

Diffuse optics for tissue monitoring and tomography

This article has been downloaded from IOPscience. Please scroll down to see the full text article.

2010 Rep. Prog. Phys. 73 076701

(<http://iopscience.iop.org/0034-4885/73/7/076701>)

[View the table of contents for this issue](#), or go to the [journal homepage](#) for more

Download details:

IP Address: 128.91.43.247

The article was downloaded on 09/06/2010 at 20:47

Please note that [terms and conditions apply](#).

Diffuse optics for tissue monitoring and tomography

T Durduran¹, R Choe², W B Baker² and A G Yodh²

¹ ICFO-Institut de Ciències Fotòniques, Mediterranean Technology Park, 08860 Castelldefels (Barcelona), Spain

² Department of Physics and Astronomy, University of Pennsylvania, Philadelphia, PA 19104, USA

E-mail: durduran@alumni.upenn.edu

Received 26 October 2009, in final form 29 January 2010

Published 2 June 2010

Online at stacks.iop.org/RoPP/73/076701

Abstract

This review describes the diffusion model for light transport in tissues and the medical applications of diffuse light. Diffuse optics is particularly useful for measurement of tissue hemodynamics, wherein quantitative assessment of oxy- and deoxy-hemoglobin concentrations and blood flow are desired. The theoretical basis for near-infrared or diffuse optical spectroscopy is developed, and the basic elements of diffuse optical tomography are outlined. We also discuss diffuse correlation spectroscopy, a technique whereby temporal correlation functions of diffusing light are transported through tissue and are used to measure blood flow. Essential instrumentation is described, and representative brain and breast functional imaging and monitoring results illustrate the workings of these new tissue diagnostics.

(Some figures in this article are in colour only in the electronic version)

This article was invited by Professor P M Chaikin.

Contents

1. Introduction	2	<i>2.13. Metabolic rate of oxygen extraction</i>	20
2. Theoretical background	3	3. Breast cancer imaging and spectroscopy	20
<i>2.1. Photon diffusion formalism</i>	3	<i>3.1. Diffuse optical mammography based on endogenous contrast</i>	20
<i>2.2. Source types</i>	5	<i>3.2. Optical mammography based on exogenous contrast</i>	22
<i>2.3. Diffuse photon density waves</i>	6	<i>3.3. Therapy monitoring</i>	22
<i>2.4. Solutions in infinite, homogeneous turbid media</i>	6	<i>3.4. Outlook: optical mammography</i>	23
<i>2.5. Boundary conditions</i>	7		
<i>2.6. Green's function solutions</i>	7	4. Optical monitoring of cerebral hemodynamics	24
<i>2.7. Solutions for semi-infinite media and other simple geometries</i>	7	<i>4.1. Clinical relevance of diffuse optics for cerebral hemodynamics</i>	24
<i>2.8. Spectroscopy for determination of tissue chromophore concentrations</i>	9	<i>4.2. Selected translational results</i>	25
<i>2.9. Diffuse correlation spectroscopy</i>	11		
<i>2.10. Tomography with diffuse photon density waves</i>	14	5. Other applications	28
<i>2.11. Fluorescence diffuse optical spectroscopy and tomography</i>	19	6. Conclusion	29
<i>2.12. Diffuse correlation tomography</i>	19	Acknowledgments	29
		References	29

Glossary

- α fraction of dynamic photon scattering events in medium
- g scattering anisotropy factor

- μ_a absorption coefficient
- μ_s scattering coefficient
- $\mu_{s\text{r}}$ reduced scattering coefficient,
 $\mu_s = \mu_{s\text{r}}(1 - g)$
- v speed of light in tissue

G_0	homogeneous Green's function
c_i	concentration of the i th chromophore
ℓ_{tr}	transport mean-free path, $\ell_{\text{tr}} \approx 1/\mu_s$
D	photon diffusion coefficient, $D = v\ell_{\text{tr}}/3$
D_b	Brownian diffusion coefficient
ε	extinction coefficient
λ	wavelength of light (nm)
$L(\mathbf{r}, \hat{\Omega}, t)$	radiance; power per unit area per unit angle traveling in $\hat{\Omega}$ direction at position \mathbf{r} and time t
$E(\mathbf{r}, \hat{\Omega}, t)$	light electric field traveling in $\hat{\Omega}$ direction at position \mathbf{r} and time t
$\mathbf{E}(\mathbf{r}, t)$	total light electric field at position \mathbf{r} and time t
$I(\mathbf{r}, t)$	light field intensity (i.e., $ E(\mathbf{r}, t) ^2$) at position \mathbf{r} and time t
G_1	electric field temporal auto-correlation function, $G_1(\mathbf{r}, \tau, t) = \langle E^*(\mathbf{r}, t)E(\mathbf{r}, t + \tau) \rangle$
G_2	intensity auto-correlation function, $G_2(\mathbf{r}, \tau, t) = \langle I(\mathbf{r}, t)I(\mathbf{r}, t + \tau) \rangle$
g_1	normalized electric field temporal auto-correlation function, $g_1(\mathbf{r}, \tau, t) = G_1(\mathbf{r}, \tau, t)/ E(\mathbf{r}, t) ^2$
g_2	normalized intensity auto-correlation function, $g_2(\mathbf{r}, \tau, t) = G_2(\mathbf{r}, \tau, t)/ I(\mathbf{r}, t) ^2$
$\Delta r^2(\tau)$	mean-square displacement in time τ of the scattering particles (e.g., red blood cells)
$\Phi(\mathbf{r}, t)$	photon-fluence rate at position \mathbf{r} and time t
$U(\mathbf{r})$	photon-fluence rate; expressed in the frequency domain, $\Phi(\mathbf{r}, t) = U(\mathbf{r})e^{-i\omega t}$
ω	laser/source modulation frequency
BFI	blood flow index estimated by DCS (i.e., αD_b)
CBF	cerebral blood flow
CMRO ₂	cerebral metabolic rate of oxygen
CT	computed tomography
CW	continuous wave
DCS	diffuse correlation spectroscopy
DOS	diffuse optical spectroscopy
DOT	diffuse optical tomography
FD	frequency domain
HbO ₂	oxy-hemoglobin concentration
Hbr/Hb	de-oxy hemoglobin concentration
ICG	indocyanine green
MRI	magnetic resonance imaging
NIRS	near infrared spectroscopy
PET	positron emission tomography
RBCs	red blood cells
StO ₂	tissue blood oxygen saturation
THC	total hemoglobin concentration
TRS	time resolved/domain spectroscopy

1. Introduction

More than 80 years ago [1] light was employed to ‘see’ tumors in thick tissues. Basic ideas from those measurements still survive today. Optical methods offer a range of sensitivities useful for characterization of a wide variety of samples. The simplest of these methods is light absorption, whereby attenuation in signal intensity occurs whenever the light wavelength coincides with a material resonance. This effect permits quantitative identification of the molecules present in a sample, their concentration and their local environment. In a different vein, light scattering provides information about micrometer-size objects (e.g., such as their molecular weight and diameter) that scatter light in the sample, and dynamic or quasi-elastic light scattering (DLS or QELS, respectively) provides information about motions of those objects. Generally, these traditional optical techniques are rigorous and are well established in simple, homogeneous, optically thin samples.

In order to use these schemes to study biological tissues, however, a physical understanding of photon propagation in highly scattering media is required. Otherwise the traditional techniques remain qualitative (at best) or are fraught with systematic errors (at worst). A key contribution to optical studies of tissue was made by Jöbsis in the late 1970s [2–4]. Jöbsis observed a spectral window in the near-infrared (NIR, ~ 650 – 950 nm) wherein photons could travel deep in tissue, as a result of the relatively small absorption of water and hemoglobin (see figure 1). Of course this penetrating light was also scattered in tissue and more physics insight was required for better quantification of detected signals. After the early work, arguably the most critical advance in the field was the recognition and widespread acceptance that light transport over long distances in tissues is well approximated as a diffusive process [5, 6]. Using this physical model it is possible to quantitatively separate tissue scattering from tissue absorption, and to accurately incorporate the influence of boundaries and heterogeneities [5, 7–22]. These models for light propagation formalized the field and paved the way for a large variety of applications ranging from imaging breast tumors (‘optical mammography’) to functional imaging of brain [23].

Generally, the propagation of light through tissues is profoundly affected by scattering. Two length scales are important in this context: a rather short ‘scattering length’ which corresponds to the typical distance traveled by photons before they scatter, and a longer ‘transport mean-free path’ or ‘random walk step’ which corresponds to the typical distance traveled by photons before their direction is randomized. The reciprocal of the photon transport mean-free path is called the reduced scattering coefficient; it is wavelength dependent and is denoted by $\mu_s(\lambda)$, where λ is the wavelength of light. Light transport in tissue is also affected by a relatively smaller absorption. The wavelength-dependent absorption length in tissue corresponds to the typical distance traveled by a photon before it is absorbed; its reciprocal, the absorption coefficient, is denoted by $\mu_a(\lambda)$.

In order to sort scattering from absorption in tissue, a model that separates the effects of tissue scattering from

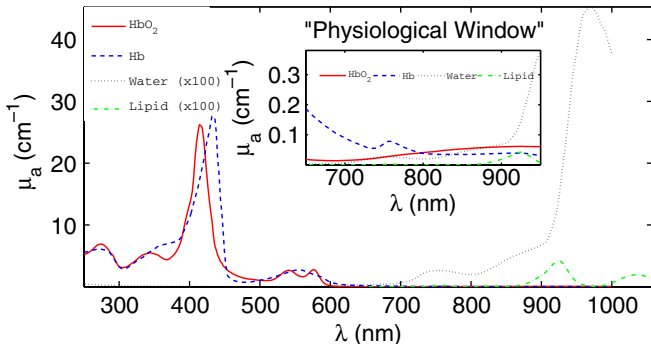


Figure 1. Absorption (μ_a) spectra of major tissue chromophores over a large wavelength range. The inset shows the so-called ‘physiological window’ in the near-infrared where water and hemoglobin absorption are relatively low. In this part of the spectrum, light can penetrate several centimeters in tissue. Furthermore, there are clear features in the spectra which enable estimation of chromophore concentration from diffuse optical measurements at several wavelengths.

tissue absorption is required. The diffusion model provides a formal mathematical basis for this separation, and as a result of this approximation, experimenters can directly measure oxy- and deoxy-hemoglobin (HbO_2 , Hbr/Hb), water and lipid concentrations using the well-known spectra (figure 1) of these molecules [5, 23]. From the scattering coefficient, experimenters gain access to information about cells, cell nuclei, cell organelles and surrounding fluids. Herein, we will refer to this measurement technique which uses diffuse near-infrared light to infer scattering and absorption, as ‘diffuse optical spectroscopy’ (DOS) or ‘near-infrared spectroscopy’ (NIRS). The imaging analog of DOS is called diffuse optical tomography (DOT); DOT provides a means to assign tissue optical and physiological properties independently to many volume elements within the tissue sample. Here we use ‘tomography’ to refer to both ‘topographic’ (2D) and ‘tomographic’ (3D) schemes because they share similar formalism.

The diffusion approach is quite versatile and can be adapted further to measure the concentrations and lifetimes of exogenous contrast agents such as dyes which can improve tumor contrast or specificity [24, 25]. A recent example of this application is fluorescence diffuse optical tomography wherein the fluorescent emission of a FDA-approved contrast agent, Indocyanine Green (ICG), was used to identify breast cancer [26]. Other uses include the measurement of the concentration of oxidized cytochrome c-oxidase [2, 27] and the measurement of very fast changes in scattering related to neuronal swelling during neuronal activity [28, 29]. To learn more about these and other applications, readers can consult recent reviews [23, 24, 30–35].

More information is available from diffusing light in tissues. Speckle fluctuations of light scattered by tissues are sensitive to the motions of scatterers such as red blood cells (RBCs). The traditional, single-scattering version of this optical technique is well known and has appeared with numerous names [36–50] over the years. In most of these experiments the temporal auto-correlation function of the

scattered electric field (or its Fourier transform) is measured and is explicitly related to the motions of scatterers within the samples. The most significant tissue signal derived from the temporal auto-correlation function is from blood flow. Early physiological work utilized single-scattering theory to analyze data derived from pairs of very closely separated (~ 0.25 mm) optodes, e.g., Laser Doppler and CCD-based speckle devices [41–43, 50–59]. Therefore, most of these early methods probed superficial tissue (< 1 mm). In the low signal limit, the photon correlation technique has an advantage over its Fourier counterpart because photon correlation instruments are essentially single photon-counting devices. This advantage enables experimenters to probe more deeply into tissue samples, and begs for theoretical models to understand similar signals from deep tissues.

The multiple scattering analog of these dynamic light scattering measurements is called ‘diffuse correlation spectroscopy’ (DCS) [60, 61] (Note, the technique called ‘diffusing wave spectroscopy’ (DWS) [62–64] was introduced before DCS. DWS is essentially an integral formulation of DCS; the name DCS, however, has been adopted in the biomedical optics field because ‘DWS’ had connotations for both absorption spectroscopy and fluctuation spectroscopy). Formally, DCS relies on the fact that temporal correlation of light fields in turbid media also obeys a diffusion equation, albeit a slightly different one than is used for absorption spectroscopy. Thus DCS shares the light penetration advantages of NIRS/DOS, but, since DCS explicitly measures cell movement, it provides a direct measure of quantities such as cerebral blood flow (CBF) [65–67]. Compared with NIRS/DOS and DOT, DCS is a relatively new methodology. DCS has been extensively validated *in vivo* in tissues, including comparisons with laser Doppler flowmetry (LDF) [65], Doppler ultrasound (DU) [65, 68–71], arterial-spin labeled MRI (ASL-MRI) [65, 66, 72, 73], xenon CT [74], fluorescent microsphere measurement of CBF [75] and against expectations from invasive and non-invasive measures of tissue physiology [65–67, 76–78]. In total, these and other [65, 66, 68–71, 73–90] studies have shown that DCS can reliably provide a blood flow index (BFI) whose changes are proportional to relative changes in tissue blood flow. Furthermore, some of these studies suggest that the combination of DCS and DOS/DOT hold potential for continuous non-invasive estimation of metabolic rate of oxygen extraction that relies on fewer approximations than DOS/DOT alone, hence improving the quality of the metabolic rate estimates [71].

The rest of this review outlines the fundamentals of diffuse optics in tutorial fashion. Toward the end of this review we illustrate the utility of diffuse optics with recent examples from optical mammography and cerebral monitoring. A glossary of terms and symbols is also provided.

2. Theoretical background

2.1. Photon diffusion formalism

Transport theory is the starting point for most theoretical formulations of diffuse optics. The key quantity in this

formulation is the light radiance, $L(\mathbf{r}, \hat{\Omega}, t)$ ($\text{W cm}^{-2} \text{sr}^{-1}$), defined as the light power per unit area traveling in the direction at position \mathbf{r} and time t . The light radiance is related to the light electric field; $L \sim |\mathbf{E}(\mathbf{r}, \hat{\Omega}, t)|^2$, where $\mathbf{E}(\mathbf{r}, \hat{\Omega}, t)$ is the electric field at (\mathbf{r}, t) traveling in the $\hat{\Omega}$ direction. $L(\mathbf{r}, \hat{\Omega}, t)$ is governed by the radiation transport equation (RTE), which is a conservation equation for the radiance in each infinitesimal volume element within the sample [91–93], i.e.,

$$\begin{aligned} \frac{1}{v} \frac{\partial L(\mathbf{r}, \hat{\Omega}, t)}{\partial t} + \hat{\Omega} \cdot \nabla L(\mathbf{r}, \hat{\Omega}, t) \\ = -\mu_t L(\mathbf{r}, \hat{\Omega}, t) + Q(\mathbf{r}, \hat{\Omega}, t) \\ + \mu_s \int_{4\pi} L(\mathbf{r}, \hat{\Omega}', t) f(\hat{\Omega}, \hat{\Omega}') d\hat{\Omega}'. \end{aligned} \quad (1)$$

$f(\hat{\Omega}, \hat{\Omega}')$ is the normalized differential cross-section for single light scattering events in the medium; it essentially gives the probability that scattered light is scattered into the direction $\hat{\Omega}'$, given its incident direction was $\hat{\Omega}$. $Q(\mathbf{r}, \hat{\Omega}, t)$ ($\text{W cm}^{-3} \text{sr}^{-1}$) is the power per volume emitted by sources at position \mathbf{r} and time t in the $\hat{\Omega}$ direction. The loss of radiance out of each infinitesimal volume element depends on the absorption and scattering coefficients in the volume and is formally characterized by the coefficient $\mu_t = \mu_a + \mu_s$. Here μ_s (cm^{-1}) is the light scattering coefficient, i.e., the reciprocal of the ‘scattering length’ (note, μ_s is different from μ_s), and μ_a (cm^{-1}) is the light absorption coefficient, i.e., the reciprocal of the ‘absorption length’. v is the speed of light in the medium. The left-hand side of equation (1) is a convective time derivative of the radiance in the infinitesimal volume element about \mathbf{r} at time t traveling in the direction $\hat{\Omega}$. This convective derivative of the radiance must equal the losses due to absorption and scattering (first term, right-hand side) plus the gains from radiance scattered into $\hat{\Omega}'$ (third term, right-hand side), and gains from sources (second term, right-hand side). In most cases of interest, the RTE must be solved numerically.

To reduce the complexity of the RTE, we employ a standard method for approximating equation (1) called the P_N approximation. In this method, L is written as a series expansion of spherical harmonics, $Y_{\ell m}$ (with coefficients $\phi_{\ell m}$), truncated at $\ell = N$ [91–94]:

$$L(\mathbf{r}, \hat{\Omega}, t) = \sum_{m=-N}^{N} \frac{2 + 1}{4\pi} \phi_{\ell m}(\mathbf{r}, t) Y_{\ell m}(\hat{\Omega}). \quad (2)$$

We also assume that the normalized differential scattering cross-section, f , depends only on the angle between incident and outgoing scattering wavevectors, i.e., $f(\hat{\Omega}, \hat{\Omega}') = f(\hat{\Omega} \cdot \hat{\Omega}')$. When $L(\mathbf{r}, \hat{\Omega}, t)$ is nearly isotropic, the so-called P_1 approximation (wherein the series expansion in equation (2) is truncated at $N = 1$) is valid, and we have [91–94]

$$L(\mathbf{r}, \hat{\Omega}, t) = \frac{1}{4\pi} \Phi(\mathbf{r}, t) + \frac{3}{4\pi} \mathbf{J}(\mathbf{r}, t) \cdot \hat{\Omega}. \quad (3)$$

Equation (3) introduces two important quantities. The photon fluence rate, $\Phi(\mathbf{r}, t)$ (W cm^{-2}), is defined as the total power per area moving radially outward from the infinitesimal volume

element at position \mathbf{r} and time t ³. More explicitly,

$$\Phi(\mathbf{r}, t) \equiv \int_{4\pi} L(\mathbf{r}, \hat{\Omega}, t) d\hat{\Omega} = \phi_{00}. \quad (4)$$

The photon flux $\mathbf{J}(\mathbf{r}, t)$ (W cm^{-2}) is a vector sum of the radiance emerging from the infinitesimal volume, i.e.

$$\begin{aligned} \mathbf{J}(\mathbf{r}, t) &\equiv \int_{4\pi} L(\mathbf{r}, \hat{\Omega}, t) \hat{\Omega} d\hat{\Omega} \\ &= \frac{1}{\sqrt{2}} (\phi_{1-1} - \phi_{11}) \hat{x} - \frac{i}{\sqrt{2}} (\phi_{1-1} + \phi_{11}) \hat{y} + \phi_{10} \hat{z}. \end{aligned} \quad (5)$$

Thus, $\mathbf{J}(\mathbf{r}, t) \cdot \hat{\Omega}$ is the power per area traveling in the $\hat{\Omega}$ direction at position \mathbf{r} and time t .

The photon fluence rate and flux are related by a continuity equation obtained from integrating equation (1) over all solid angles:

$$\frac{1}{v} \frac{\partial \Phi(\mathbf{r}, t)}{\partial t} + \nabla \cdot \mathbf{J}(\mathbf{r}, t) + \mu_a \Phi(\mathbf{r}, t) = S(\mathbf{r}, t). \quad (6)$$

Here, $S(\mathbf{r}, t)$ (W cm^{-3}) is the total power per volume emitted radially outward from position \mathbf{r} at time t , i.e., $S(\mathbf{r}, t) \equiv \int_{4\pi} Q(\mathbf{r}, \hat{\Omega}, t) d\hat{\Omega}$.

In the P_1 approximation, another relation between Φ and \mathbf{J} is obtained by substituting equation (3) into equation (1); we then multiply the resulting P_1 transport equation by $\hat{\Omega}$ and integrate over all solid angles to obtain⁴

$$\begin{aligned} \nabla \Phi(\mathbf{r}, t) &= -\frac{3}{v} \frac{\partial \mathbf{J}(\mathbf{r}, t)}{\partial t} - 3\mu_t \mathbf{J}(\mathbf{r}, t) \\ &+ 3 \int_{4\pi} Q(\mathbf{r}, \hat{\Omega}, t) \hat{\Omega} d\hat{\Omega} + 3\mu_s g \mathbf{J}(\mathbf{r}, t). \end{aligned} \quad (7)$$

The anisotropy factor g , which emerges from the differential scattering integral in equation (1), is the ensemble average of the cosine of the scattering angle θ , i.e., $g \equiv \int_{4\pi} f(\hat{\Omega} \cdot \hat{\Omega}') \hat{\Omega}' d\hat{\Omega}' = \langle \cos \theta \rangle$. The closer g is to unity, the more probable it is for a photon to be scattered in the forward direction. In soft mammalian tissue, typical values for g range between 0.8 and 0.98 [95].

Assuming isotropic sources ($Q(\mathbf{r}, \hat{\Omega}, t) = Q(\mathbf{r}, t)$), the integral over Q in equation (7) is zero. Furthermore, if we also assume slow temporal variations in the photon flux \mathbf{J} , then $(1/v)\partial \mathbf{J}/\partial t$ in equation (7) can be neglected compared with $(\mu_t - \mu_s g)\mathbf{J}$. With these two assumptions, equation (7) simplifies to Fick’s law of diffusion, i.e.,

$$\nabla \Phi(\mathbf{r}, t) = -3(\mu_s + \mu_a) \mathbf{J}(\mathbf{r}, t). \quad (8)$$

$\mu_s \equiv (1 - g)\mu_s$ is called the reduced scattering coefficient.

Substituting equation (8) into equation (6) results in the photon diffusion equation for the photon fluence rate [20, 96, 97]:

$$\begin{aligned} \nabla \cdot (D(\mathbf{r}) \nabla \Phi(\mathbf{r}, t)) - v\mu_a(\mathbf{r}) \Phi(\mathbf{r}, t) - \frac{\partial \Phi(\mathbf{r}, t)}{\partial t} \\ = -vS(\mathbf{r}, t). \end{aligned} \quad (9)$$

³ Some authors prefer to use the photon energy concentration, $\Gamma(\mathbf{r}, t)$ (J cm^{-3}), which is directly proportional to the fluence rate: $\Gamma = v\Phi$.

⁴ For any vector \mathbf{A} , $\int_{4\pi} \hat{\Omega}(\hat{\Omega} \cdot \mathbf{A}) d\hat{\Omega} = \frac{4\pi}{3} \mathbf{A}$, and $\int_{4\pi} \hat{\Omega} [\hat{\Omega} \cdot \nabla (\mathbf{A} \cdot \hat{\Omega})] d\hat{\Omega} = 0$. Also, $\int_{4\pi} \frac{\partial \Phi}{\partial t} \hat{\Omega} d\hat{\Omega} = \frac{\partial \Phi}{\partial t} \int_{4\pi} \hat{\Omega} d\hat{\Omega} = 0$ and $\int_{4\pi} f(\hat{\Omega} \cdot \hat{\Omega}') \hat{\Omega} \cdot \hat{\Omega}' d\hat{\Omega}' = \int_{4\pi} f(\hat{\Omega} \cdot \hat{\Omega}') \hat{\Omega}' \cdot \hat{\Omega} d\hat{\Omega}'$.

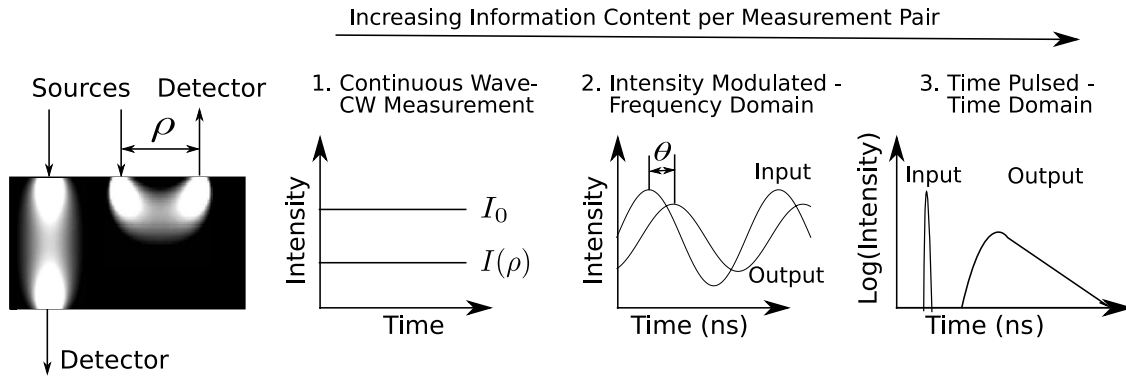


Figure 2. Three common types of sources are employed. On the far left are schematic ‘banana patterns’ showing the sampled volumes in the reflection and transmission geometries. As a rough rule of thumb, the mean light penetration depth in the reflection geometry is of order $\rho/2$ (for a more precise relation, see [495]). For continuous wave (CW), intensity modulated (FD) and time-resolved (TR) sources, the detected light intensity over time resembles (1), (2) and (3) respectively.

Here we have defined the photon diffusion coefficient $D(r) \equiv v/3(\mu_s(r) + \mu_a(r))$.

Microscopically, within this P_1 picture, photons travel through the medium along random walk pathways. Each photon is visualized to travel in straight-line segments with sudden interruptions wherein either the propagation direction is randomly changed or the photon is absorbed. The average length of the straight-line segments is the photon random walk step or the transport mean-free path, τ_{tr} , which is approximately $1/\mu_s$.

The validity of the photon diffusion model (equation (9)) rests on the validity of the P_1 approximation (equation (3)), which requires the radiance to be nearly isotropic ($J \gg |J|$). This isotropy is achieved when $\mu_s \approx \mu_a$, and when photon propagation distances within the medium are large relative to τ_{tr} . As a rough rule of thumb, μ_s/μ_a should exceed 10 to accurately apply the diffusion model [98]. Additional assumptions, noted above, include source isotropy, slow temporal flux variations, and rotational symmetry (i.e., $f(\hat{\Omega}, \hat{\cdot}) = f(\hat{\cdot} \cdot \hat{\cdot})$). Near a boundary such as an air–tissue interface, the radiance will no longer be nearly isotropic. In section 2.5, we will show how the diffusion model can be applied near the surface with additional boundary conditions at the interface. For anisotropic tissues, such as axon fiber bundles where the rotational symmetry assumption may no longer be reasonable, slightly more complicated anisotropic diffusion models [99] are necessary for data fitting. For complex tissues that contain ‘non-diffusing’ domains such as (arguably) cerebral spinal fluid inside the head [100, 101], or that contain very high concentrations of blood, as in the liver, optimal data analysis requires approximations beyond P_1 . In applications wherein photon propagation distances are comparable to τ_{tr} , the photon propagation directions do not fully randomize. Thus, approximations beyond the P_1 are needed here as well. We will discuss various schemes that extend beyond the diffusion (P_1) approximation in section 2.10.

2.2. Source types

To apply the diffusion model, one typically detects light at known distances from point sources. Figure 2 shows two

source–detector pairs; one in the reflection geometry and the other in the transmission geometry. In the reflection geometry, light injected into the tissue by a source fiber (usually coupled to a laser) is detected a distance ρ away with another fiber (usually coupled to a photomultiplier tube or avalanche photodiode). In the transmission geometry, light detection is facilitated using either a fiber or a lens/CCD camera system. At first glance, the directional light from a fiber violates the isotropic source assumption for the diffusion model. This light source, however, can be very well approximated by an isotropic light source at depth τ_{tr} inside the tissue [97]. In practice, source–detector separation should exceed $3\tau_{tr}$ to apply the diffusion model and expect accurate (~5%) results [102].

Three types of light sources commonly used in diffuse optics are (see figure 2): continuous wave (CW), intensity modulated (FD) and time pulsed (TRS). The simplest source type is CW light, where the intensity remains constant over time [103–106]. CW sources enable fast data acquisition and the use of simple detectors and detection electronics, but as we will discuss further, μ_a and D cannot be determined simultaneously from a single CW measurement.

Intensity modulated sources (the frequency-domain technique, FD) are more complex but also give more information about the medium [9, 15, 107, 108]. Here, the light intensity of the source at position r_s is sinusoidally modulated with angular frequency ω (of order 100 MHz or larger, up to ~1 GHz), producing a diffusive wave in the medium oscillating at the same frequency. At a given source–detector separation, both the amplitude and phase of the diffusing wave are measured. The additional information from the phase, in principle, permits simultaneous determination of μ_a and D .

Time pulsed light (the time-domain technique, TRS) is related to intensity modulated light via a Fourier transform, and it contains the same information content as intensity modulated sources scanned over the wide range of modulation frequencies present in the pulse [8, 12, 109–112]. Specifically, a short light pulse (<100 ps) is delivered to the medium at position r_s and time t_s . The pulse temporally broadens as it propagates through the medium. At the detector, the pulse shape contains the necessary information to determine D and

μ_a from a single source-detector pair. Also, by employing time-gating and moments analysis at the detection end, it is possible to pathlength resolve the detected light in order to reject contributions from superficial tissue layers [113, 114].

2.3. Diffuse photon density waves

Most of the following theoretical discussion will be given in the frequency domain, with the time-domain solution given for a common case. Frequency-domain sources induce fluence rate disturbances that behave in many ways as overdamped waves. To appreciate this point, we start with the diffusion equation for the fluence rate (equation (9)) and assume the source term has dc and ac parts and can be written in the form $S(r, t) = S_{dc}(r) + S_{ac}(r)e^{-i\omega t}$. Then we look for the solutions that oscillate at the same angular frequency as the source. These ac solutions will have the following general form:

$$S_{ac}(r, t) = U(r)e^{-i\omega t}. \quad (10)$$

Substituting S_{ac} into equation (9), we see that $U(r)$ is described by

$$\nabla \cdot (D(r)\nabla U(r)) - (v\mu_a(r) - i\omega)U(r) = -vS_{ac}(r), \quad (11)$$

which for homogeneous media gives

$$\nabla^2 - k^2 U(r) = -\frac{v}{D}S_{ac}(r), \quad (12)$$

with $k^2 = (v\mu_a - i\omega)/D$. The general solution of equation (12) is an overdamped wave-like fluence rate ‘disturbance’ in the turbid medium. Note, slightly different definitions for k^2 , e.g., $k^2 = (-v\mu_a + i\omega)/D$ or $k^2 = -(v\mu_a + i\omega)/D$ with $S_{ac}(r, t) = U(r)e^{i\omega t}$, enable us to write equation (12) in a Helmholtz form. This approach was used early on and had the advantage of more obvious analogies with waves. Of course, regardless of the way terms are defined in equation (12), the solutions are the same.

2.4. Solutions in infinite, homogeneous turbid media

The simplest geometry to consider is the infinite, homogeneous medium with a single intensity modulated point source at the origin ($S_{ac}(r) = S_{ac}\delta(r)$). In this case, the main boundary condition is that the fluence rate falls to zero at infinity. The solution to equation (12) in this geometry is well known. It has the form of a simple overdamped spherical wave with complex wavevector $k = k_r + ik_i$:

$$U(r) = \frac{vS_{ac}}{4\pi Dr} \exp(-kr). \quad (13)$$

Here, $r = |\mathbf{r}|$,

$$k_r = \frac{v\mu_a}{2D}^{1/2} \left[1 + \frac{\omega^2}{v\mu_a} + 1 \right]^{1/2}, \quad (14)$$

$$k_i = -\frac{v\mu_a}{2D}^{1/2} \left[1 + \frac{\omega^2}{v\mu_a} - 1 \right]^{1/2}. \quad (15)$$

Writing the fluence rate in the form $U(r) = Ae^{i\theta}$, the determination of the change in wave amplitude, A , and wave

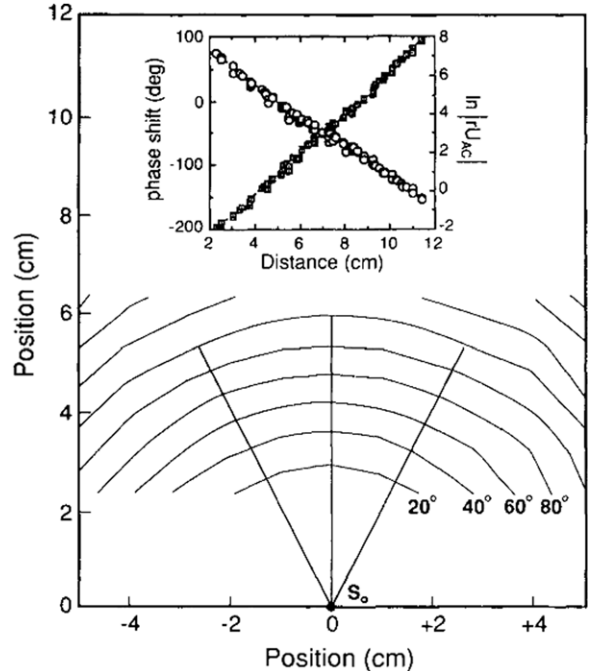


Figure 3. Constant phase contours shown as a function of position for homogeneous, 0.5% Intralipid solution filling a large aquarium ($30 \times 30 \times 60 \text{ cm}^3$). At the origin (roughly the middle of the aquarium) is the source (3 mW laser diode operating at 816 nm and modulated at 200 MHz), resulting in a geometry that very well approximates a homogeneous infinite medium. The contours are shown in 20° intervals. Inset: the measured phase shift (squares) and $\ln |rU(r)|$ (circles) are plotted as a function of radial distance from the source. The slopes reveal $-k_i$ and k_r , from which μ_a and D can be calculated using equations (15) and (14). (Reprinted with permission from [13]. Copyright 1992 American Physical Society.)

phase, θ , with distance from the source enables experimenters to extract the absorption and reduced scattering factors of the turbid medium. In figure 3 we show a measurement [13] of the amplitude and phase of such a diffuse photon density wave (DPDW).

In tissue measurements, a typical set of parameters are $\mu_s = 10 \text{ cm}^{-1}$, $\mu_a = 0.025 \text{ cm}^{-1}$, $\omega = 2\pi \times (70 \text{ MHz})$ and an index of refraction $n = 1.4$. In this case the DPDW wavelength ($2\pi/k_i \sim 19 \text{ cm}$) is roughly a factor of 20 greater than the attenuation length ($1/k_r \sim 1 \text{ cm}$). In the near-field, DPDWs have been demonstrated to exhibit several familiar wave-like properties including diffraction [14], refraction [13], interference [16] and dispersion [17].

The time-domain and frequency-domain solutions to equation (9) are Fourier transform pairs. Therefore, if the solution in one domain is known, then it is straightforward to determine the solution in the other domain. The Fourier transform of equation (13) gives the fluence rate solution in the presence of a pulsed point source of the form, $S(r, t) = S_0\delta(\mathbf{r})\delta(t)$, in the homogeneous infinite medium. The resulting fluence rate is

$$\Phi(r, t) = \frac{vS_0}{(4\pi Dt)^{3/2}} \exp \left(-\frac{r^2}{4Dt} - \mu_a vt \right). \quad (16)$$

Here, to derive optical properties, one performs a nonlinear fit comparing equation (16) with the measured

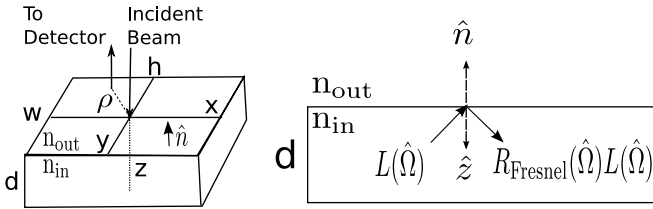


Figure 4. Common geometry used to model tissue. In the semi-infinite geometry, w , h and d all go to infinity, while in the infinite-slab geometry, w and h are infinite but d is finite. Both geometries have azimuthal symmetry about the z -axis, meaning the photon fluence rate only depends on the radial and axial cylindrical coordinates ρ and z . The unit vector \hat{n} points from inside the tissue to outside. On the left, a single source–detector pair (with separation ρ) in the reflection geometry is shown. Note that for the slab geometry, detectors can also be used for transmission measurements by being placed on the $z = d$ plane. On the right is a cross-section showing that the radiance moving into the turbid medium at the boundary is due to the Fresnel reflection of the radiance incident on the boundary.

fluence rate temporal arrival distribution at the detector (using only a single source–detector separation). The fitting determines D and μ_a . Alternatively, if it is only necessary to determine μ_a , the nonlinear fit can be avoided by noting that $\partial \ln \Phi(r, t)/\partial t \rightarrow -\mu_a v$ as $t \rightarrow \infty$. Thus, μ_a is given by the slope of the natural log of the fluence rate at long times (i.e., typically only a few nanoseconds).

2.5. Boundary conditions

While conceptually useful, the infinite homogeneous medium is not a good approximation for practical tissue geometries. Most realistic geometries have interfaces. A particularly useful geometry is the planar interface wherein a semi-infinite turbid tissue is bounded in the other half-space by air. To derive boundary conditions for the light diffusion problem, it is necessary to consider the radiance again. Typically, photons escaping from the tissue into air will never re-enter the tissue medium. Thus, the incoming irradiance (i.e., total light power per area traveling into the diffuse medium at the boundary), J_{in} , is due to Fresnel reflections of the radiance in the diffuse medium that travels out toward the interface (see figure 4):

$$\begin{aligned} J_{in} &\equiv \int_{\hat{n} \cdot \hat{\Omega} < 0} L(\hat{\Omega}) \hat{\Omega} \cdot (-\hat{n}) d\Omega \\ &= \int_{\hat{n} \cdot \hat{\Omega} > 0} R_{Fresnel}(\hat{\Omega}) L(\hat{\Omega}) \hat{\Omega} \cdot \hat{n} d\Omega. \end{aligned} \quad (17)$$

$R_{Fresnel}(\hat{\Omega})$ is the familiar Fresnel reflection coefficient for light incident upon the boundary in a direction $\hat{\Omega}$ from within the medium.

Using the diffusion model, i.e., substituting the P_1 approximation (equation (3)) in for L , and an appropriate form for $R_{Fresnel}(\hat{\Omega})$, one readily obtains the so-called partial-flux boundary condition (also known as the Robin boundary condition) which relates the fluence rate to its gradient at the boundary [115, 116]:

$$= z_b \hat{n} \cdot \nabla \quad \text{on the interface.} \quad (18)$$

Here, $z_b = 2_{tr}(1+R_{eff})/3(1-R_{eff})$, where R_{eff} is the effective reflection coefficient to account for the index mismatch between tissue and air: $R_{eff} \approx -1.440n^{-2} + 0.710n^{-1} + 0.668 + 0.00636n$ (R_{eff} is defined exactly in table 1). $n = n_{in}/n_{out}$ is the ratio of the index of refraction ‘inside’ and ‘outside’ the diffusing medium.

The partial-flux boundary condition is exact, but it is relatively difficult to use, especially if analytical solutions to the diffusion equation with interfaces are desired. In this case, a simpler boundary condition is usually made as an approximation to the more fundamental result. In particular, the fluence rate is Taylor expanded to first order around the boundary, with the first-derivative term taken from the partial-flux boundary condition. The treatment gives a zero-crossing point for the fluence rate at a distance, z_b , outside (i.e., on the air side) of the tissue (figure 5):

$$\Phi(z = -z_b) = 0. \quad (19)$$

Equation (19) is called the extrapolated-zero boundary condition. It approximates the exact partial-flux boundary condition quite well (see [115, 116] for details). With this ‘new’ zero fluence rate interface, it is readily possible to use the method of images to obtain analytic solutions in a variety of geometries. Many researchers employ numerical methods to solve these and other problems; in such cases the partial-flux boundary condition is often directly incorporated into the numerical codes rather than the extrapolated-zero boundary condition (for example, see [117]).

2.6. Green’s function solutions

An age old strategy [118, 119] employed to solve the time-domain and frequency-domain diffusion equations (equations (9) and (11)) is to first find their respective Green’s functions, and then to use these Green’s functions to construct more general solutions. In diffuse optical spectroscopy, the usual assumption is to treat tissues as homogeneous media. For homogeneous media, equation (9) can be written in the form $\hat{A}\Phi(r, t) = -vS(r, t)/D$, where $\hat{A} \equiv \nabla^2 - \partial/\partial t - v\mu_a$. The time-domain Green’s function $G_0(r, r_s, t, t_s)$ then satisfies $\hat{A}G_0(r, r_s, t, t_s) = -\delta(r - r_s)\delta(t - t_s)$ and the boundary conditions for the geometry of interest. Similarly, equation (12) can be written in the form $\hat{B}U(r) = -vS_{ac}(r)/D$, where $\hat{B} \equiv \nabla^2 - k^2$. The frequency-domain Green’s function $G_0(r, r_s)$ then satisfies $\hat{B}G_0(r, r_s) = -\delta(r - r_s)$ and the relevant boundary conditions. The full fluence rate solution in homogeneous media will be the convolution of these Green’s functions with the source term vS/D .

2.7. Solutions for semi-infinite media and other simple geometries

In NIRS/DOS, the most commonly used models approximate tissue either as a homogeneous semi-infinite medium or as a homogeneous infinite slab (figure 4). In both geometries, the method of images can be employed to find the diffusion equation Green’s functions, subject to the extrapolated-zero

Table 1. Frequency-domain Green's functions for equation (12) in several homogeneous geometries subject to the extrapolated-zero boundary condition (equation (19)). r_s is the position of a normalized isotropic point source. With the exception of the infinite case, cylindrical coordinates are used explicitly to specify position, i.e., $\mathbf{r} = (\rho, z)$. Notation is defined in the lower part of the Table. In practice, the infinite sums are truncated after a desired accuracy has been reached.

Case	Green's function (frequency domain)
Infinite	$G_0(\mathbf{r}, \mathbf{r}_s) = \frac{1}{4\pi \mathbf{r} - \mathbf{r}_s } \exp(-k \mathbf{r} - \mathbf{r}_s)$
Semi-infinite	$G_0([\rho, z], [\rho_s = 0, z_s = z_{tr}]) = \frac{1}{4\pi} \frac{\exp(-kr_1)}{r_1} - \frac{\exp(-kr_b)}{r_b}$
Infinite slab	$G_0([\rho, z], [\rho_s = 0, z_s = z_{tr}]) = \frac{1}{4\pi} \sum_{m=-\infty}^{\infty} \frac{\exp[-kr_{+,m}]}{r_{+,m}} - \frac{\exp[-kr_{-,m}]}{r_{-,m}}$
Infinite cylindrical	$G_0([\rho, z], [\rho_s, z_s]) = \frac{1}{2\pi a_b^2} \sum_{m=-\infty}^{\infty} \cos m\varphi \frac{e^{- z-z_s /\sqrt{k^2+\beta_m^2}}}{\beta_m} \frac{J_m(\beta_m \rho) J_m(\beta_m \rho_s)}{[J_m(\beta_m a_b)]^2}$
$k \equiv \sqrt{(\mu_a v - i\omega)/D}$	$J_m(z)$ m th order Bessel function, 1st kind
$r_{\pm,m} \equiv \sqrt{\rho^2 + (z - z_{\pm,m})^2}$	a , cylinder radius
$z_{+,m} \equiv 2m(d + 2z_b) + z_{tr}$	$a_b = a + z_b$, i.e., extrapolated-zero boundary (cylinder)
$z_{-,m} \equiv 2m(d + 2z_b) - 2z_b - z_{tr}$	β_m , a positive root of $J_m(\beta_m a_b) = 0$
$k_m \equiv \sqrt{k^2 + m^2 \pi^2 / h_b^2}$	ρ , radial cylindrical coordinate
$r_1 \equiv \sqrt{(z - z_{tr})^2 + \rho^2}$	$r_b \equiv \sqrt{(z + 2z_b + z_{tr})^2 + \rho^2}$
$R_{\text{eff}} \equiv \frac{R_\phi + R_J}{2 - R_\phi + R_j}$	$z_b = 2 z_{tr} \frac{1 + R_{\text{eff}}}{3(1 - R_{\text{eff}})}$
$R_\phi \equiv \int_0^{\pi/2} \sin(2\vartheta) R_{\text{Fresnel}}(\vartheta) d\vartheta$	$R_J \equiv \int_0^{\pi/2} 3 \sin \vartheta \cos^2 \vartheta R_{\text{Fresnel}}(\vartheta) d\vartheta$
m , an integer	d , slab thickness (figure 4)
$\cos \vartheta = \hat{\mathbf{n}} \cdot \hat{\mathbf{r}}$ (figure 4)	$R_{\text{Fresnel}}(\vartheta)$, Fresnel reflection coefficient
ϑ , angle of incidence in $R_{\text{Fresnel}}(\vartheta)$	φ , angle between input/output light beams (cylinder)

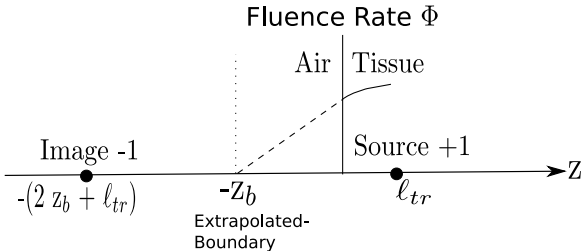


Figure 5. The fluence rate curve is approximated by its tangent line at $z = 0$, and the $z = 0$ intercept of this curve is found to occur $z = -z_b$ (z_b is defined exactly in table 1).

boundary condition (equation (19)) [120, 121]. For example, consider a single normalized isotropic point source at position (in cylindrical coordinates) $\mathbf{r}_s = (\rho_s = 0, z_s = z_{tr})$ in the semi-infinite geometry. Recall from section 2.2 that this source is a good approximation for light injected into the tissue by a fiber at $\mathbf{r} = (\rho = 0, z = 0)$. The extrapolated-zero boundary condition is satisfied by introducing a negative image point source at $z_s = -(2z_b + z_{tr})$ (figure 5). Superposition of the infinite medium solutions (equation (13)) from each (positive and negative) point source yields the homogeneous semi-infinite Green's function. In the frequency domain,

$$G_0([\rho, z], [\rho_s = 0, z_s = z_{tr}])$$

$$= \frac{1}{4\pi} \frac{\exp(-kr_1)}{r_1} - \frac{\exp(-kr_b)}{r_b}, \quad (20)$$

where

$$r_1 = \sqrt{(z - z_{tr})^2 + \rho^2}, \quad (21)$$

$$r_b = \sqrt{(z + 2z_b + z_{tr})^2 + \rho^2}. \quad (22)$$

Let us now consider a NIRS/DOS measurement in reflection on a tissue sample, using a frequency-domain source (figure 4). Assuming the tissue is well modeled by a homogeneous semi-infinite geometry, the fluence rate along the tissue surface is $S_0 v G_0([\rho, z = 0], [\rho_s = 0, z_s = z_{tr}])/D$, where G_0 is given by equation (20) and S_0 is the strength of the source. This solution contains two independent equations: one for the fluence rate amplitude, $A(\rho)$, and the other for the phase, $\theta(\rho)$. Thus, as with the infinite medium (section 2.4), by measuring $A(\rho)$ and $\theta(\rho)$, one can solve the system of equations from the semi-infinite solution for D and μ_a .

We note that the detected light signal is the radiance integrated over the collection solid angle, which in the diffusion model is proportional to the fluence rate near the detector [115, 122]. It is difficult to predict this proportionality constant theoretically. Thus, in practice additional amplitude and phase-shift unknowns are usually incorporated into the solutions. Multiple source-detector separations are preferred to minimize this uncertainty and enable calibration.

Equation (20) can be fit exactly, but in the limit, $\rho \ll (\ell_{tr} + 2z_b)$. The solution then simplifies to

$$\begin{aligned} U(\rho, z = 0) &\approx \frac{v S_0}{4\pi D} \frac{e^{-k\rho}}{\rho^2} 2k(z_{tr} z_b + z_b^2) \\ &= \frac{A_0 e^{-k_r \rho}}{\rho^2} e^{i(-k_i \rho + \theta_0)} = A(\rho) e^{i\theta(\rho)}. \end{aligned} \quad (23)$$

Note that in this limit, $\ln[\rho^2 A(\rho)]$ and $\theta(\rho)$ depend linearly on ρ ,

$$\ln(\rho^2 A(\rho)) = -k_r \rho + \ln A_o, \quad (24)$$

$$\theta(\rho) = -k_i \rho + \theta_0, \quad (25)$$

making it particularly simple to fit for k_i and k_r , which in turn permits calculation of μ_a and D .

The method of images can also be used to compute the frequency-domain Green's functions for a homogeneous turbid medium in other geometries [120, 121]. Table 1 shows the frequency-domain Green's functions subject to the extrapolated-zero boundary condition for several simple geometries. Similarly, analytic solutions exist for heterogeneities such as spherical [123] and cylindrical [124] inclusions in homogeneous media as well as for multi-layer media [125–129].

2.8. Spectroscopy for determination of tissue chromophore concentrations

The tissue absorption depends linearly on the concentrations of tissue chromophores. In particular, the wavelength-dependent absorption coefficient is given by

$$\mu_a(\lambda) = \sum_i \varepsilon_i(\lambda) c_i. \quad (26)$$

Here $\varepsilon_i(\lambda)$ is the wavelength-dependent extinction coefficient (usually known for typical tissue chromophores) and c_i the concentration of the i th chromophore. We have seen above (sections 2.4 and 2.7) that the diffusion approximation enables us to separate the scattering and absorption contributions in the detected light signals. Thus, by measuring μ_a at multiple optical wavelengths, we generate a system of coupled equations (equation (26)) that can be solved to yield the unknown chromophore concentrations. Generally, to estimate the concentrations of N chromophores, one must determine μ_a at N or more wavelengths.

NIRS/DOS is typically employed to measure oxygenated and de-oxygenated hemoglobin; thus a bare minimum of phase and amplitude measurements at two wavelengths are required. Use of more wavelengths permits inclusion of other tissue chromophores such as water and lipid, and also improves the accuracy of the hemoglobin measurements because measurement redundancy reduces systematic errors. Of course, more wavelengths increase the cost and complexity of the instrument and require longer data acquisition times.

The most common NIRS/DOS configuration is the reflection geometry, which employs the homogeneous semi-infinite medium analysis described above (section 2.7) to derive $\mu_a(\lambda)$. However, other geometries are sometimes used to obtain bulk tissue properties; in this case the derived phase-shift and amplitude as a function of source-detector separation are usually more complex than the simple linear functions outlined above, and the fitting is correspondingly more tricky (but still possible). Imaging schemes employ essentially the same ideas on a volume-element-by-volume-element basis to assign chromophore concentrations to particular voxels in the sample (see section 2.10).

NIRS/DOS provides quick estimates of bulk chromophore concentrations in large tissue volumes. These estimates

are often accurate enough to be useful in many monitoring applications (see section 4).

One technical problem associated with the multi-source/detector, multi-wavelength approach arises because each source and each detector has a different light coupling coefficient to tissue. This ‘coupling coefficient’ (generally, a complex number in the frequency domain) is a parameter that combines many factors such as the wavelength-dependent fiber transmission, different source and detector optics, differences in the physical properties of sources and detectors, electronics and tissue-fiber interfaces. The measured fluence rate for a given source-detector pair is thus equal to a product of the true fluence rate with the pair’s coupling coefficients. The light coupling coefficients for each source-detector pair will be additional unknowns in the inverse problem. If the coupling coefficients for different source-detector pairs are significantly different, then the NIRS/DOS inverse problem is harder with added variables [130]. Several methods are commonly employed to address this problem. One approach uses calibration phantoms with known optical properties to determine the coupling coefficients before and after each experiment (see [131]). A second approach employs self-calibrating probes (see [81]). The first method assumes the coupling will be the same for tissue and phantom; the second method assumes tissue homogeneity. In the case of tomography (section 2.10), it is often assumed that the reference measurement cancels out these coupling coefficients [132]. A more rigorous approach is to consider the coupling coefficients as unknowns and explicitly reconstruct them [130].

2.8.1. Optimal wavelengths.

Determination of tissue chromophore concentrations requires the separation of tissue absorption from tissue scattering at more than one optical wavelength. The optimal choice of wavelengths for chromophore concentration determination is an important topic in its own right, with an interesting history that involved careful consideration of measurement type, i.e., frequency-, time domain, CW and measurement signal-to-noise. For simple, two-wavelength time- and frequency-domain instruments, early experimenters wondered about which wavelengths to choose to minimize cross-talk between chromophores when inverting equation (26). Superficially, one might expect that at least one wavelength within the NIR window should be below the isosbestic point of hemoglobin and one should be above this isosbestic point. The isosbestic point is the wavelength wherein the extinction coefficients of oxygenated and de-oxygenated hemoglobin are the same (~ 800 nm, see figure 1); wavelengths below the isosbestic point are thus more sensitive to deoxy-hemoglobin, while wavelengths above are more sensitive to oxy-hemoglobin. However, such wavelength selection processes are limited. Yamashita *et al* [133], Strangman *et al* [134] and Boas *et al* [135] have shown theoretically and experimentally that when using only two wavelengths, a pair at 660–760 nm and 830 nm provides superior oxy- and deoxy-hemoglobin separation by comparison with what was the more commonly used choice of 780 and 830 nm.

A formal evaluation of the optimum wavelength selection for an arbitrary number of wavelengths was carried out by Corlu *et al* [136, 137]; they introduced a general procedure for finding those wavelengths which best differentiate tissue chromophores using CW and frequency-domain light. These results built on a theoretical approach developed in a classic paper by Lionheart and Arridge [138]. That paper [138] theoretically proved that it is impossible to uniquely separate scattering from absorption in a diffuse optical imaging experiment employing CW light. In an attempt to circumvent this uniqueness problem for CW imaging, Corlu *et al* demonstrated that a multi-spectral approach can be employed to uniquely reconstruct the chromophore concentrations, c_i . In a key advance, Corlu *et al* [136, 137] abandoned the two-step approach of determining μ_a at each wavelength first and then inverting equation (26). Instead, they introduced a multi-spectral approach that exploits known spectral properties of the medium *a priori* to directly reconstruct chromophore concentrations with better fidelity than the traditional two-step method. Specifically, *a priori* assumptions about the form of the scattering (e.g., $\mu_s(\lambda) = A\lambda^{-b}$) and wavelength-dependent absorption extinction factors (i.e. equation (26)) are used, and the wavelength independent variables c_i , A and b are reconstructed directly from all of the data simultaneously. Because the data from all wavelengths are simultaneously used, the inverse problem is better constrained than the traditional approach (see [137] for details). The multi-spectral technique is now commonly used, and has been extended for frequency-domain sources [139], for including uncertainties in the hemoglobin extinction coefficients [140], and for spectral window optimization when using broadband sources [141].

2.8.2. The differential pathlength (DPF) approach. In many situations, we are interested in the temporal variation of quantities such as hemoglobin concentration or oxygenation with respect to some perturbation. In such cases, one need only measure ‘changes’ in tissue optical properties, i.e., $\Delta\mu_a$ and $\Delta\mu_s$. If $\Delta\mu_a$ and $\Delta\mu_s$ are small relative to their baseline values, $\mu_a^{(0)}$ and $\mu_s^{(0)}$, respectively, and if they are homogeneously distributed across the sample, then a much simpler differential pathlength method can be employed using only the intensity of the detected light. Specifically, this method relates temporal changes in the optical density, $OD \equiv -\ln(A(r_d, t)/A(r_s))$, to changes in chromophore concentrations [10, 120, 134, 142–146]. Here $A(r, t)$ is the fluence rate amplitude. Furthermore, only one source-detector separation is needed to estimate these concentration changes.

The differential pathlength method is derived by truncating the Taylor series expansion of the optical density for a given source-detector separation ρ to first order in μ_a and μ_s :

$$\begin{aligned} OD(\mu_a^{(0)} + \Delta\mu_a, \mu_s^{(0)} + \Delta\mu_s, \rho) &\approx OD(\mu_a^{(0)}, \mu_s^{(0)}, \rho) \\ &+ \frac{\partial OD(\mu_a^{(0)}, \mu_s^{(0)}, \rho)}{\partial \mu_a} \Delta\mu_a + \frac{\partial OD(\mu_a^{(0)}, \mu_s^{(0)}, \rho)}{\partial \mu_s} \Delta\mu_s. \end{aligned} \quad (27)$$

Substituting equation (26) into equation (27), we see that temporal changes in the detected optical density, i.e.,

$$\begin{aligned} OD(\lambda, t, \rho) &\equiv -\ln(A(r_d, t)/A(r_d, t = 0)) \\ &= OD(\mu_a^{(0)}(\lambda) + \Delta\mu_a(\lambda, t), \mu_s^{(0)}(\lambda) + \Delta\mu_s(\lambda, t), \rho) \\ &\quad - OD(\mu_a^{(0)}(\lambda), \mu_s^{(0)}(\lambda), \rho), \end{aligned} \quad (28)$$

may be related to changes in tissue chromophore concentrations and scattering through a modified Beer-Lambert law:

$$\begin{aligned} OD(\lambda, t) &\approx \sum_i (\varepsilon_i(\lambda) \Delta c_i(t)) d_a(\rho, \lambda) \\ &\quad + \Delta\mu_s(\lambda, t) d_s(\rho, \lambda) \sim \sum_i (\varepsilon_i(\lambda) \Delta c_i(t)) DPF(\lambda) \rho. \end{aligned} \quad (29)$$

Here, $d_a \equiv \partial OD(\lambda, t = 0, \rho)/\partial \mu_a$ and $d_s \equiv \partial OD(\lambda, t = 0, \rho)/\partial \mu_s$ are called the differential absorption and scattering pathlengths, respectively, for wavelength λ (or baseline values $\mu_a^{(0)}(\lambda) = \mu_a(\lambda, t = 0)$ and $\mu_s^{(0)}(\lambda) = \mu_s(\lambda, t = 0)$) and source-detector separation ρ [120]. The last step in equation (29) is an approximation that is utilized widely in studies of brain hemodynamics (see section 4). This approximation assumes that scattering is unchanged (i.e., $\Delta\mu_s = 0$) and that $d_a(\rho, \lambda) = DPF(\lambda)\rho$, where DPF is a ‘normalized’ ρ -independent differential pathlength factor usually obtained from the literature.

Thus, by measuring OD at multiple wavelengths, we can invert equation (29) to determine the changes in chromophore concentrations Δc_i . Again, in addition to assuming small absorption and scattering changes, equation (29) assumes homogeneously distributed changes for $\Delta\mu_a$ and $\Delta\mu_s$. If the changes are localized, the modified Beer-Lambert law leads to systematic underestimations of the chromophore concentration changes (i.e., the partial volume effect) [145].

The parameters d_a and d_s depend on source-detector separation, tissue geometry and the baseline optical properties of the underlying tissue, which in turn depend on the wavelength used. The parameters can be estimated analytically with a diffusion model, numerically using the Monte Carlo method [146], or measured using pulse-time methods in a sample of statistically similar tissue types [10]. Pulse-time methods are relevant for a differential pathlength analysis involving light intensity only, because here the differential pathlength factors are related to the photon mean time of flight in tissue, t , determined by pulse-time methods [120], i.e.,

$$d_a = 1 + \frac{\mu_a}{\mu_a + \mu_s} v t, \quad (30)$$

$$d_s = \frac{\mu_a v}{\mu_a + \mu_s} t. \quad (31)$$

The differential pathlength approach essentially makes a best estimate for the actual light pathlength in the tissue. Although it is clearly a very approximate method, it has been employed extensively in the biomedical optics community (see [35, 147–150], and many others).

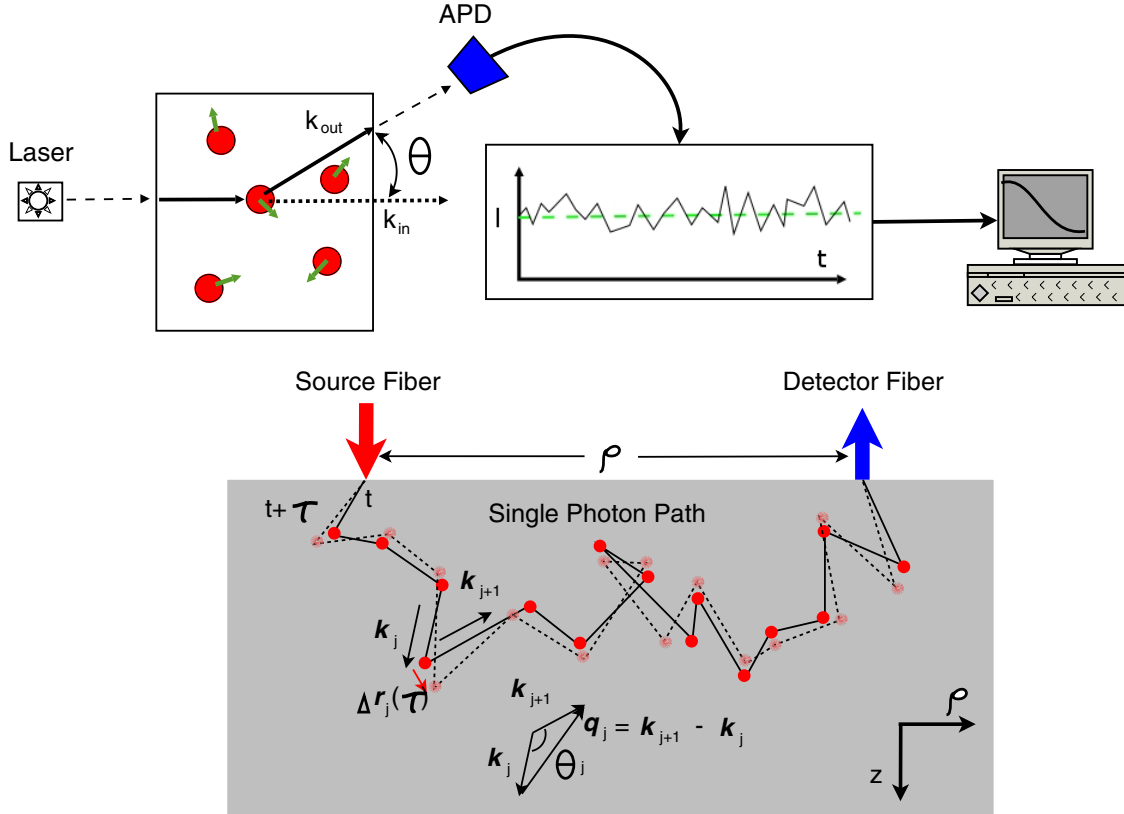


Figure 6. Illustration of a single scattering DLS experiment (top) and of multiple scattering (bottom) along a single photon path in turbid media. k_j and k_{j+1} are the wavevectors before and after the j th scattering event, respectively. $q_j = k_{j+1} - k_j$ is the momentum transfer and θ_j is the scattering angle of the j th scattering event. The solid line represents the photon path at time t , while the dotted line represents the photon path at time $t + \tau$. During the delay time τ , the j th scatterer moves $\Delta r_j(\tau)$. (Reprinted courtesy of Zhou [496].)

2.9. Diffuse correlation spectroscopy

2.9.1. Dynamic light scattering in the single-scattering limit.

The dynamic light scattering (DLS) (sometimes called quasi-elastic light scattering (QELS)) technique is a well-known optical method for measuring the motions of scatterers such as particles in suspension [45, 46, 151]. In the experiment (figure 6(top)), a light beam illuminates a sample. To be concrete, let us assume that the sample is composed of a dilute solution of particles or macro-molecules; dilute in the sense that light is scattered once or not at all as it traverses the sample. Each of the particles develops an induced dipole moment in the presence of the incident light, and these oscillating dipoles, in turn, emit scattered light fields into all directions. The scattered light electric field at the detector, $E(t)$, is thus built from a superposition of these dipole contributions. Because the particles move, the relative phases of the scattered dipole fields change and the light field (and light intensity) at the detector fluctuates in time.

It is straightforward to show [45, 46, 151] that for independent particles with isotropic dynamics, the normalized electric field temporal auto-correlation function (g_1) at the detector is

$$g_1(\tau) \equiv \frac{\mathbf{E}^*(t) \cdot \mathbf{E}(t + \tau)}{\langle |\mathbf{E}(t)|^2 \rangle} = e^{i2\pi f\tau} e^{-q^2 \Delta r^2(\tau)/6}. \quad (32)$$

Here, f is the frequency of the incident light, q is the scattered wavevector representing the difference between output and

input beam wavevectors and $\Delta r^2(\tau)$ is the mean-square particle displacement in time τ . The brackets represent time-averages (for experiments) or ensemble averages (for calculations). Thus by measuring the temporal fluctuations of scattered light, one obtains quantitative information about the particle motions. For the case of Brownian motion, $\langle \Delta r^2(\tau) \rangle = 6D_b\tau$; for the case of random flow, $\langle \Delta r^2(\tau) \rangle = V^2 \tau^2$. Here, D_b is the particle diffusion coefficient and V^2 is the second moment of the particle speed distribution. Of course there are other types of motions (e.g., rotation) which affect these signals, but we will restrict our discussion to these two types of particle motion.

In practice, experimenters often measure the scattered, normalized intensity temporal auto-correlation function (g_2); $g_2(\tau) \equiv \langle I(t)I(t + \tau) / I(t)^2 \rangle$, with the intensity $I(t) = |\mathbf{E}(t)|^2$. The Siegert relation [152],

$$g_2(\tau) = 1 + \beta |g_1(\tau)|^2, \quad (33)$$

is then used to extract the electric field auto-correlation function from the intensity data. β is a constant determined primarily by the collection optics of the experiment, and is equal to one for an ideal experiment setup.

2.9.2. Dynamic light scattering in the multiple light scattering limit.

In samples such as tissue or more concentrated colloidal suspensions, the incident light field is multiply

scattered. As with light diffusion, one can envision the electric field temporal auto-correlation function propagating ballistically, then scattering from small volume elements within the sample, and then propagating ballistically again in a random manner as the light makes its way from one side of the sample to the other side. Each of these ‘single’ dynamic light scattering events, from a volume element within the sample, contributes to the detected correlation function. This is illustrated in figure 6(bottom). It is thus apparent that the detected field auto-correlation function is also related to motions of the scatterers within the medium, albeit in a more complex way. There has been elegant research on this multiple ‘dynamic light scattering’ problem over the years (for example, see [61–63, 153–155]). In the late 1980s the diffusing wave spectroscopy (DWS) technique was formulated [62, 63, 156]. In DWS, the phase of the various photon random walk paths through the sample is computed at time $\tau = 0$ and then recomputed at time τ . When the scattering events within each path are uncorrelated, and when the diffusion approximation is valid, one finds that the detected field autocorrelation function is then essentially equal to the angle-averaged DLS signal due to a typical single scattering event in the random walk sequence raised to the power N (where N is the number of random walk steps in the photon path). The detected signal is the integral of these single-path signals over all allowed photon paths. Another approach, which we will discuss in detail below, employs correlation transport theory to derive a diffusion equation for the field auto-correlation function. The correlation transport equation and the resultant correlation diffusion equation are particularly attractive in the context of tissues, because they share a formal similarity with the results we have presented already about diffuse photon density waves.

2.9.3. Diffusion of temporal correlation functions. Temporal fluctuations in the sample are characterized by an unnormalized electric field auto-correlation function, $G_1^T(r, \hat{\Omega}, \tau) = \langle E^*(r, \hat{\Omega}, t) \cdot E(r, \hat{\Omega}, t + \tau) \rangle$, where the brackets denote the usual time and/or ensemble averages, and as mentioned earlier, $E(r, \hat{\Omega}, t)$ is the electric field at position r and time t propagating in the $\hat{\Omega}$ direction. Ackerson and co-workers first suggested that G_1^T is analogous to the radiance L and should be governed by a correlation transport equation [154, 155]:

$$\nabla \cdot G_1^T(r, \hat{\Omega}, \tau) + \mu_t G_1^T(r, \hat{\Omega}, \tau) = Q(r, \hat{\Omega}) + \mu_s G_1^T(r, \hat{\Omega}, \tau) g_1^s(\hat{\Omega}, \tau) f(\hat{\Omega}, \tau) d\Omega. \quad (34)$$

Here $g_1^s(\hat{\Omega}, \tau)$ is the normalized temporal field auto-correlation function for single scattering (see equation (32)), $f(\hat{\Omega}, \tau)$ is the normalized differential single scattering cross-section, $Q(r, \hat{\Omega})$ is the light source distribution and $\mu_t = \mu_a + \mu_s$. Equation (34) is a steady-state equation independent of time, meaning it is applicable for CW sources and systems in equilibrium.

Given equation (34), one can implement a set of steps formally identical to the steps used to derive the diffusion equation for photon fluence rate from the radiative transport equation. That is, using a P_1 approximation for G_1^T ,

the correlation transport equation reduces to the correlation diffusion equation for correlation ‘fluence rate’ [60, 61]:

$$\begin{aligned} \nabla \cdot (D(r) \nabla) - v \mu_a(r) - \frac{\alpha}{3} v \mu_s \kappa_0^2 \Delta r^2(\tau) G_1(r, \tau) \\ = -v S(r). \end{aligned} \quad (35)$$

Here, $G_1(r, \tau)$ is the correlation fluence rate, i.e.

$$G_1(r, \tau) = \frac{G_1^T(r, \hat{\Omega}, \tau) d\Omega}{4\pi} = E^*(r, t) \cdot E(r, t + \tau), \quad (36)$$

where $E(r, t)$ is the total light electric field at (r, t) , and $S(r)$ is an isotropic source term:

$$S(r) = \frac{Q(r, \hat{\Omega}) d\Omega}{4\pi}. \quad (37)$$

α represents the fraction of photon scattering events that occur from moving particles in the medium, $\Delta r^2(\tau)$ is the usual mean-square displacement in time τ of the scattering particles (e.g., blood cells), $\kappa_0 = 2\pi/\lambda$ is the wavenumber of the CW light diffusing through the medium and D , μ_a and v are the same optical properties that arise in the photon diffusion equation (equation (9)). Furthermore, a set of analogous correlation diffusion boundary conditions arise for $G_1(r, \tau)$:

$$G_1(r, \tau) = z_b \hat{n} \cdot \nabla G_1(r, \tau) \quad \text{Partial-flux.} \quad (38)$$

$$G_1(z = -z_b, \tau) = 0 \quad \text{Extrapolated zero..} \quad (39)$$

Diffuse correlation spectroscopy (DCS) refers to the measurement of the temporal diffusing field auto-correlation function to obtain information about tissue dynamics. Equation (35) is essentially a differential equation formulation of diffusing wave spectroscopy (DWS). It is better suited than DWS for handling point sources, heterogeneous media and tomography. Note also that if we take the $\tau = 0$ limit of the correlation diffusion equation, then we obtain the CW diffusion equation for photon fluence rate.

Since equation (35) with its boundary conditions has the same form as the photon diffusion equation (equation (9)) for CW sources, Green’s function solutions of the correlation diffusion equation will also have the same form. For example, in a homogeneous semi-infinite medium, the solution to equation (35) is (see equation (20)),

$$G_1(\rho, z, \tau) = \frac{v}{4\pi D} \frac{\exp(-K(\tau)r_1)}{r_1} - \frac{\exp(-K(\tau)r_b)}{r_b}, \quad (40)$$

where $K(\tau) = (\mu_a + \alpha \mu_s \kappa_0^2 \Delta r^2(\tau)/3)v/D$, and r_1 and r_b are given by equations (21) and (22), respectively. The new feature is that the decay constant, $K(\tau)$, also depends on the correlation time τ ; of course that is where the dynamical information resides.

As in the case of DLS, the quantity measured in practice is usually not G_1 , but is instead proportional to the intensity auto-correlation function $G_2(r, \tau) = \langle I(r, t)I(r, t + \tau) \rangle$, where $I(r, t) = |E(r, t)|^2$. Again, the Siegert relation (equation (33)) may be used to relate the intensity and field auto-correlation functions.

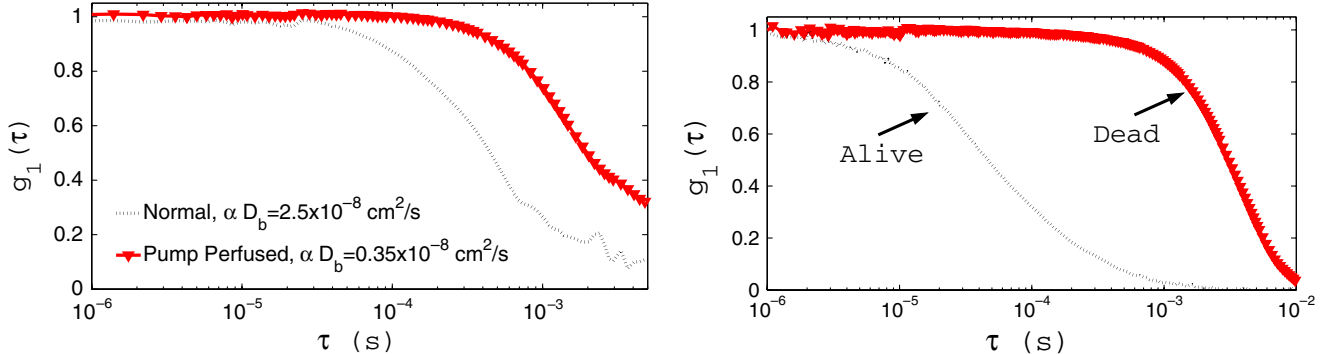


Figure 7. The measured intensity auto-correlation curves from two experiments on isolated limb preparations on rats. (left) Shows the electric field correlation functions during healthy circulation and under artificial perfusion with a pump. (right) Shows the electric field auto-correlation functions from a rat before/after death.

Thus, G_1 is derived from the experimentally measured G_2 , and K^2 is determined by fitting to the temporal decay of G_1 (for a given source-detector separation). This information plus optical property information permit determination of $\alpha \Delta r^2(\tau)$.

Strictly speaking, the Siegert relation is fully valid if the electric field, $E(r, t)$, is a Gaussian variable in time with zero mean [152]. For samples such as tissue, wherein some scatterers are static and some scatterers move, the total electric field will have static and dynamic components and can be written as $E(r, t) = E_c(r) + E_f(r, t)$. Here, E_c is a time-independent contribution to the total field from photons that have experienced only static scattering on their path from source to detector. E_f is the field due to photons that have experienced at least one dynamic scattering event between source and detector; this field will fluctuate in time. Application of the Siegert relation in such cases requires careful consideration of the interference terms involving E_c and E_f . To date, a few methods for circumventing this problem have been developed [157–159], e.g., moving the sample (or detector) to induce fluctuations in E_c [157] or choosing speckles wherein E_c is small. We have conducted experiments in tissue phantoms and tissues to explore this further. In most practical tissue geometries we have found that the intensity auto-correlation functions decay to unity (typical field auto-correlation measurements are shown in figure 8); collectively these measurements indicate that E_c is small, perhaps because most of the detected photon paths involve at least one moving red blood cell or another slow moving tissue scatterer (e.g., due to subtle vibrations or other effects). More work remains to clarify this observation. Nevertheless, it appears that one can routinely employ the Siegert relation in most tissue dynamics experiments, except perhaps those wherein the subject is exercising.

2.9.4. Blood flow indices from diffuse correlation spectroscopy. DCS is most sensitive to the motion of blood cells in the microvasculature (i.e. capillaries, arterioles, venules), since the diffusing light is mostly absorbed when traversing large arteries and veins. Typical detected photons experience scattering events from static (or very slow moving) scatterers in biological tissue (e.g., organelles and interfaces),

in addition to the dynamic scattering from moving RBCs (see previous section for details) [153].

Since the microvasculature is convoluted, we may expect that the distribution of the directions of velocities of the sampled RBCs is more or less isotropic. Thus, the random ballistic flow model is sometimes a first ‘guess’ as a choice for the dynamics of RBCs, where $\langle \Delta r^2(\tau) \rangle = V^2 \tau^2$ (see section 2.9.1). In practice, however, we and others [65, 66, 68–90] have found that the Brownian model, $\langle \Delta r^2(\tau) \rangle = 6D_b\tau$, fits the observed correlation decay curves better over a wide range of tissue types including rat brain [77, 78]; mouse tumors [68]; piglet brain [75]; and human skeletal muscle [81], tumors [83, 84] and brain [66, 69, 71, 74, 80] (see figure 8). In these cases, D_b is an effective diffusion coefficient obtained from fitting to correlation data; it is a few orders of magnitude larger than the traditional thermal Brownian diffusion coefficient of RBCs in the blood given by the Einstein-Smoluchowski relation [160]. Upon reflection, it should not be too surprising that the random flow model does not fit the data well. RBCs in the microvasculature do not move ballistically; they experience position-dependent shear stresses, they roll, they tumble and they translate in the vasculature.

Clearly, the final cumulative effect of photon-RBC interactions on the measured auto-correlation function will depend on both the nature of the microscopic motions and on the spatial distribution of moving particles in tissue. In the vasculature, both of these factors can be quite complex [161, 162], and, in fact, their affects on light signals are not fully understood. The situation is further complicated by the non-trivial distribution of photon paths in tissue; for example, contributions from the largest vessels tend to be small, since photons that interact with RBCs in an artery are mostly absorbed and do not reach the detector.

Despite these apparent difficulties, we (and others) have worked to elucidate DCS measurement sensitivity. For example, we have carried out isolated limb perfusion measurements in rats (see figure 7(left)). The figure shows two correlation decay curves, one from the limb with normal circulation and the other due to controlled circulation (of roughly the same speed) of an external suspension of RBCs (with ~ 10 times reduced concentration) through the same

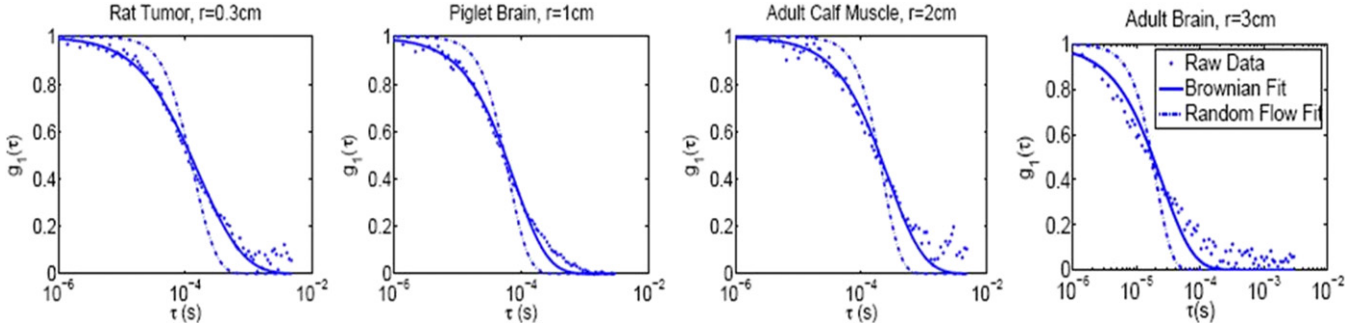


Figure 8. Data from a mouse tumor, a piglet brain, a human calf muscle and adult human brain. Dots show the experimental data, the dashed line is a fit with $\Delta r^2 \sim \tau^2$ (random flow) and the solid line is a fit with $\Delta r^2 \sim \tau$ (Brownian motion). Note how the accuracy of the fits vary depending on the delay time (τ) and the longer delays tend to deviate further from the fits for brain measurements. This is mainly because later delays correspond to photons that probe more superficial tissues and presence of the skull alters this part of the curves. Note, r in the figure titles is the source-detector separation on the tissue surface.

vasculature. The measurement clearly demonstrates that our signal is due to RBC motion. Variation of RBC concentration in suspension decreased the measured αD_B in a proportional manner (~ 7.2 times). When healthy flow is compared with that from a dead limb the residual decay is $< 3\%$ of the baseline (see figure 7(right)). In the latter state, we altered and monitored the temperature of the limb while continuing to measure the correlation decay. Fitted αD_B was dependent linearly on the temperature, as expected for true Brownian motion of the scatterers, which has a linear temperature dependence.

Furthermore, we (and others) have found that the fitted parameter αD_B (from the Brownian model) correlates well with other blood flow measurement modalities. As a result, it is natural to identify the αD_B parameter as a blood flow index (BFI). The BFI is not a measure of absolute blood flow in the strict sense (e.g., it has the wrong units), but the relative change in BFI has been repeatedly shown to be a quantitative measure of relative change in blood flow. In particular, it has been shown that under well controlled circumstances, αD_B is proportional to the absolute blood flow measured by ASL-MRI [73] and transcranial Doppler ultrasound [69, 71]. Similar sorts of ambiguities are well known in the Laser Doppler literature, and in general, calibration and empirical modeling are used to estimate absolute values of blood flow velocity [43, 153, 163]. Calibration methods similar to those utilized by laser Doppler, e.g., to calibrate for ‘biological zero’, are also applicable for DCS [164–167]. We also note that it is possible (but difficult without constraints) to measure absorption and even scattering with DCS [168].

2.10. Tomography with diffuse photon density waves

Many of the simplifying assumptions used in spectroscopy, such as homogeneity and a semi-infinite or infinite-slab geometry, are relaxed when imaging with diffusing waves. By using a more realistic model of tissue, diffuse optical tomography (DOT) improves the accuracy of the measured optical properties. Tomography is also critical for identification of localized heterogeneities such as tumors in tissue. The goal of DOT is to reconstruct the spatial distribution of optical/physiological properties at each point (or volume element) in the tissue from measurements of fluence rate on

the tissue surface. This problem is typically called the ‘inverse problem’, whereas ‘forward problem’ refers to the calculation of the fluence rate on the tissue surface given a particular spatial distribution of optical/physiological properties. The transport/diffusion equations provide a tractable mathematical basis for tomographic image reconstruction [30].

Unfortunately, the dominance of scattering in light propagation makes each fluence rate measurement sensitive to a relatively large tissue volume compared, for example, with x-ray CT wherein scattering is minimal. The inverse problem in diffuse optical imaging is thus much more difficult than standard x-ray CT. The DOT inverse problem is also intrinsically nonlinear with respect to the tissue optical properties. As a result, it is computationally intensive to arrive at the inverse solutions, though as we will discuss, for some applications the problem can be linearized.

Despite these difficulties, several approaches have been developed and successfully applied for diffuse optical tomography (DOT) [30, 34, 169–171]. These include: backprojection methods [172, 173], diffraction tomography in k -space and variants [174–177], perturbation approaches [178–182], the Taylor series expansion approach [183–188], gradient-based iterative techniques [189, 190], elliptic systems methods [191, 192], truncated Newton schemes [193–196], multigrid inversion algorithms [197] and Bayesian conditioning [198–205]. Other important and related theoretical advances include the development of analytic inversion formalisms [206–209], development and clarification of differencing [210] and differential [211] methodologies, and advances in the use of *a priori* information [212, 213]. Experimentally, different schemes such as the use of spatially structured/modulated illumination [214–216] and phased-arrays of sources [217, 218] were also considered to improve localization. For other recent reviews on image reconstruction, see [23, 30, 31, 98, 219–221].

As mentioned before, though the diffusion model is adequate for light transport in most tissues, many biomedical applications involve tissues with ‘non-diffusing domains’ and/or tissue volumes which are smaller than a few scattering lengths. To handle these cases, more complex (and more computationally intensive) models are needed. These models are summarized in recent reviews [30, 220]. One

approach consists of schemes based on the full radiative transport equation [30, 190, 222–224], which have recently been reviewed by Klose and Hielscher [225]. This approach has been especially successful for imaging small tissue volumes such as the finger [226]. Another approach is to use higher order P_N approximations of the transport equation [227–230]. If DOT is combined with an anatomical MRI, then it is possible to segment tissue into diffusive and non-diffusive regions. In this case, a hybrid model can be applied where light transport is modeled by diffusion in the diffusive regions and by radiosity theory [30, 231–233] or Monte Carlo [234] in the non-diffusive regions. The disadvantage of the hybrid model is that the boundaries between the diffusive and non-diffusive regions must be known. That said, many researchers are combining DOT with other imaging methods such as MRI in order to have more prior information to constrain the inverse problem. The incorporation of prior information improves the resolution and accuracy of the reconstructed images with DOT. A comprehensive review focusing on the incorporation of prior information into DOT has been recently published by Dehghani *et al* [235].

In the following sections, some common tomography approaches are outlined. Forward problem computations are an essential part of most of the methods used to solve the inverse problem. For simple geometries (e.g., table 1), analytic solutions to the forward problem are quite useful. However, for complex geometries and/or heterogeneous optical property distributions, the forward problem is sometimes solved using numerical finite-difference methods (FDM), finite-element methods (FEM), boundary element methods (BEM) or Monte Carlo [30, 181, 182, 190, 236, 237]. Tomography approaches can be classified as linear or nonlinear. As mentioned above, the tomography inverse problem is nonlinear, but in the limit that the volume element optical properties are close to a specified background, the inverse problem is approximately linear (section 2.10.1). This is usually the case for imaging differences in optical properties. For example, in a functional brain activation experiment, the perturbations in optical properties due to the brain stimulation are small compared with the background resting state of the brain (i.e., no stimulus). However, if the goal is to measure absolute optical properties, the full nonlinear problem should be tackled. Here, we focus the discussion on frequency-domain single-wavelength data; one can readily expand these ideas to continuous-wave and time-domain sources, as well as multispectral data (section 2.8.1).

2.10.1. Linear numerical inversion using the perturbation approach. To start, we write the optical properties at position \mathbf{r} as

$$\mu_a(\mathbf{r}) = \mu_a^{(0)} + \delta\mu_a(\mathbf{r}), \quad (41)$$

$$D(\mathbf{r}) = D^{(0)} + \delta D(\mathbf{r}), \quad (42)$$

where $\delta\mu_a(\mathbf{r})$ and $\delta D(\mathbf{r})$ can be regarded as perturbations from a homogeneous ‘background’ medium with optical properties $\mu_a^{(0)}$ and $D^{(0)}$. Here, $\mu_a^{(0)}$ and $D^{(0)}$ are estimated from a tissue spectroscopy measurement or from values reported in the literature for similar tissue samples. Thus, the inverse problem

utilizes measurements of fluence rate on the tissue surface to determine $\delta\mu_a(\mathbf{r})$ and $\delta D(\mathbf{r})$, given some $\mu_a^{(0)}$ and $D^{(0)}$.

Two common forms are used for $U(\mathbf{r})$ to set up the inverse problem [238]. The Born approach writes $U(\mathbf{r}) = U_0(\mathbf{r}) + U_{sc}(\mathbf{r})$, while the Rytov approach writes $U(\mathbf{r}) = U_0(\mathbf{r}) \exp[U_{sc}^R(\mathbf{r})]$. In both cases, U_0 is the spatial part of the frequency-domain fluence rate in the homogeneous background medium, which can be calculated theoretically given $\mu_a^{(0)}$ and $D^{(0)}$, and U_{sc} ($\exp[U_{sc}^R]$) is the correction to U_0 as a result of the heterogeneities. Note that U_{sc} has units of power per area, but U_{sc}^R is dimensionless. For more detail on both approaches see [238].

Let us focus on the Born approach. Corresponding Rytov results will also be given. In the linear perturbative approach, $U(\mathbf{r})$ is set equal to its first-order Taylor series expansion about U_0 , i.e., $U = U_0 + (\partial U_0 / \partial \mu_a) \delta\mu_a + (\partial U_0 / \partial D) \delta D$. This defines a simple linear problem for $\delta\mu_a$ and δD :

$$J_{a,ij}, J_{s,ij} \quad \delta\mu_a(\mathbf{r}_j), \delta D(\mathbf{r}_j)^\top = \{U_{sc}(\mathbf{r}_d, \mathbf{r}_s)_i\}, \quad (43)$$

where $[J] = J_{a,ij}, J_{s,ij} = [\partial U_0(\mathbf{r}_j) / \partial \mu_a, \partial U_0(\mathbf{r}_j) / \partial D]$ is the Jacobian. The index i refers to the source-detector pair and the index j refers to the position within the sample. Equation (43) is derived from an expansion of U to first order, whose accuracy depends on $\delta\mu_a$ and δD being small. We note that the terminology weight matrix, sensitivity matrix and Jacobian are often used interchangeably in the literature to refer to the matrix in equation (43).

One could potentially calculate the Jacobian directly using numerical methods, but the perturbation approach lets one derive an analytic expression for the Jacobian. Substituting $U(\mathbf{r}) = U_0 + U_{sc}$, equation (41), and equation (42) into the heterogeneous diffusion equation (equation (11)) gives a differential equation for U_{sc} :

$$\nabla^2 - k^2 \quad U_{sc}(\mathbf{r}) = \frac{v\delta\mu_a(\mathbf{r})}{D_0} U(\mathbf{r}) \\ - \frac{\delta D(\mathbf{r})}{D_0} \nabla^2 U(\mathbf{r}) - \nabla \cdot \frac{\delta D(\mathbf{r})}{D_0} \nabla U(\mathbf{r}). \quad (44)$$

As before, $k^2 = (v\mu_a^{(0)} + i\omega)/D^{(0)}$. The integral solution for $U_{sc}(\mathbf{r}_d, \mathbf{r}_s)$, at detector position \mathbf{r}_d given source position \mathbf{r}_s , is given by the convolution of the homogeneous Green’s function $G_0(\mathbf{r}_d, \mathbf{r})$ (for the geometry of interest) with the right-hand side of equation (44) (see chapter 5 of [239]):

$$U_{sc}(\mathbf{r}_d, \mathbf{r}_s) = \frac{-v\delta\mu_a(\mathbf{r})}{D_0} G_0(\mathbf{r}_d, \mathbf{r}) U(\mathbf{r}, \mathbf{r}_s) d^3 r \\ + \frac{\delta D(\mathbf{r})}{D_0} \nabla G_0(\mathbf{r}_d, \mathbf{r}) \cdot \nabla U(\mathbf{r}, \mathbf{r}_s) d^3 r. \quad (45)$$

Equation (45) is intrinsically nonlinear in $\delta\mu_a(\mathbf{r})$ and $\delta D(\mathbf{r})$ because $U(\mathbf{r}, \mathbf{r}_s)$ on the right-hand side also depends on $\delta\mu_a(\mathbf{r})$ and $\delta D(\mathbf{r})$.

If we assume that $U_0 = U_{sc}$, equation (44) is readily linearized, i.e., U is replaced with U_0 in the integrals (U_0 is independent of the perturbations $\delta\mu_a$ and δD). Discretization of the integral in equation (45) leads to a sum over NV elements (or voxels) of size ΔV :

$$U_{sc}(\mathbf{r}_d, \mathbf{r}_s) = \sum_{j=1}^{NV} W_{a,j} \delta\mu_a(\mathbf{r}_j) + W_{s,j} \delta D(\mathbf{r}_j), \quad (46)$$

where $W_{a,j} = -v\Delta V G_0(\mathbf{r}_d, \mathbf{r}_j)U_0(\mathbf{r}_j, \mathbf{r}_s)/D_0$ and $W_{s,j} = \Delta V \nabla G_0(\mathbf{r}_d, \mathbf{r}_j) \cdot \nabla U_0(\mathbf{r}_j, \mathbf{r}_s)/D_0$.

In tomography problems, many source-detector pairs are typically spread out over the sample surface. Given NM source-detector pairs, equation (46) is most easily expressed as a matrix equation that relates a vector of source-detector measurements to a vector of absorption and diffusion coefficient variations at voxels within the sample. Note that equations (46) and (43) are identical (i.e. $[J] = [W]$), so that

$$J_{a,ij} = \frac{\partial U_0}{\partial \mu_a}_{ij} = \frac{-v\Delta V}{D_0} G_0(\mathbf{r}_d^i, \mathbf{r}_j)U_0(\mathbf{r}_j, \mathbf{r}_s^i), \quad (47)$$

$$J_{s,ij} = \frac{\partial U_0}{\partial D}_{ij} = \frac{\Delta V}{D_0} \nabla G_0(\mathbf{r}_d^i, \mathbf{r}_j) \cdot \nabla U_0(\mathbf{r}_j, \mathbf{r}_s^i). \quad (48)$$

The matrix $[J]$ has dimensions $NM \times (2NV)$, the measurement vector $\mathbf{U}_{sc} = \mathbf{U} - \mathbf{U}_0$ has length NM , and the perturbation vector $\{\delta\mu_a, \delta D\}$ has length $2NV$. Note, in most practical cases in the frequency domain, amplitude and phase data are further split in the matrix. Finally, the measurement vector \mathbf{U}_{sc} is obtained from measurements of the fluence rate \mathbf{U} ; but as we discussed in section 2.7, the intensity measured in practice for a given source-detector pair, $I(\mathbf{r}_d, \mathbf{r}_s)$, is proportional to the fluence rate $U(\mathbf{r}_d, \mathbf{r}_s)$. Thus, as with spectroscopy (see earlier discussion on ‘coupling coefficients’ in section 2.8), a calibration scheme or explicit reconstruction of these unknowns should be employed [130].

The linearized Rytov approach (i.e., $U(\mathbf{r}) = U_0(\mathbf{r}) \times \exp[U_{sc}^R(\mathbf{r})]$) leads to a matrix equation of the same form as equation (43), except that the measurement vector $U_{sc}^R(\mathbf{r}_d, \mathbf{r}_s) = \ln[U(\mathbf{r}_d, \mathbf{r}_s)/U_0(\mathbf{r}_d, \mathbf{r}_s)]$ and the Jacobian terms are

$$J_{a,ij} = G_0(\mathbf{r}_d^i, \mathbf{r}_j)U_0(\mathbf{r}_j, \mathbf{r}_s^i)(-\nu\Delta V/U_0(\mathbf{r}_d^i, \mathbf{r}_s^i)D_0), \quad (49)$$

$$J_{s,ij} = \nabla G_0(\mathbf{r}_d^i, \mathbf{r}_j) \cdot \nabla U_0(\mathbf{r}_j, \mathbf{r}_s^i)(\Delta V/U_0(\mathbf{r}_d^i, \mathbf{r}_s^i)D_0). \quad (50)$$

Note, the Rytov approximation requires that the scattered field varies comparatively slowly (i.e., $(\nabla U_{sc}^R)^2$ is small relative to $v\delta\mu_a/D^{(0)}$ and $(\delta D/D^{(0)})(\nabla G_0/G_0)^2$).

The construction and the inversion of equation (43) is generally the computationally most expensive step in the tomography problem. Because the Jacobian is almost always a nonsquare matrix ($NM \times 2NV$), one often multiplies equation (43) by the transpose of the Jacobian to create a square matrix for the inversion, i.e.,

$$[J]^T [J] \{\delta\mu_a, \delta D\}^T = [J]^T \{\mathbf{U}_{sc}\}. \quad (51)$$

$[J]^T [J]$ is usually singular, or close to singular, and is thus difficult to invert directly. Furthermore, experimental noise in the data tends to produce artifacts when explicitly solving equation (51). To convert equation (51) into a more readily solvable problem, a regularization parameter is usually introduced into the inverse problem. The regularization parameter is employed to suppress effects of measurement noise and model errors,

$$[J]^T [J] + R^g [C]^T [C] \{\delta\mu_a, \delta D\}^T = [J]^T \{\mathbf{U}_{sc}\}, \quad (52)$$

where R^g is a regularization scalar that weights a regularization operator $[C]$ [188, 240–243]. Regularization is a theoretical

knob that can be adjusted to smooth image artifacts from experimental noise and other errors at the cost of decreasing the spatial resolution [244, 245].

Let us review the steps for this inversion approach. The linearized inversion problem constructs a suitable ‘perturbed’ fluence rate, often within Born or Rytov approximations. The so-called ‘background’, ‘baseline,’ or ‘homogeneous’ field, \mathbf{U}_0 , is either measured (e.g., using a homogeneous phantom before the breast scan, or during a ‘rest’ period in the case of functional studies of the brain) or calculated using a forward solver. The second step is the construction of the appropriate Jacobian (or weight matrix), which is derived from analytic solutions, numerical solutions (such as finite-element or finite-difference forward solutions of the photon diffusion equation) or a combination thereof. Then, typically, some sort of a regularization is applied to the Jacobian. Thus, up to this point, the steps are cumbersome but straightforward. The next step is to invert the often ill-posed Jacobian. Many strategies can be employed for this purpose, including ‘standard’ singular value decomposition (SVD), algebraic reconstruction technique (ART) or simultaneous iterative reconstruction technique (SIRT), and k -space expansions [30, 170, 175, 179, 206, 208, 220, 239, 246, 247]. Despite the well-known [30, 170, 220, 239, 246] limitations of linearized methods, these methods are employed for many applications including functional brain imaging, wherein well defined and often localized optical property changes occur in response to neuronal stimulation (see section 4), and optical mammography, wherein optical properties change in response to stimuli such as compression (see section 3). Furthermore, in applications that involve many time points and near real-time feedback, such as the case of bedside monitoring of brain function, the linearized inversion is attractive as a feasible option given the current state of portable computational power and speed.

2.10.2. Linear analytical inversion with assumed symmetry.

For simple geometries such as semi-infinite, infinite slab, infinite cylindrical and spherical, Schotland and colleagues have developed a fast alternative method for solving the inverse problem. Essentially, this method exploits the symmetry of the geometry to avoid constructing and inverting the entire weight matrix in equation (43) [174, 206–208, 248]. Here, we will outline the method for the infinite-slab geometry using the Rytov approach.

The geometry is as defined in figure 4 where ρ is the position vector on the plane where there is symmetry. By exploiting this symmetry, the Green’s function (G_0) can be expanded in plane waves along ρ [175, 249], i.e.,

$$G_0(\rho, z; \rho_s, z_s) = \frac{1}{(2\pi)^2} \int d^2q \zeta(\mathbf{q}; z, z_s) e^{i\mathbf{q} \cdot (\rho - \rho_s)}, \quad (53)$$

where $\zeta(\mathbf{q}; z, z_s)$ gives the amplitude and phase of the plane wave with wavevector $\mathbf{q} = (q_x, q_y)$ in the plane z due to a source in the plane z_s . Analytic expressions for $\zeta(\mathbf{q}; z, z_s)$ are given in [208].

Substituting equation (53) into the linearized Rytov solution (section 2.10.1) and then taking a four-dimensional

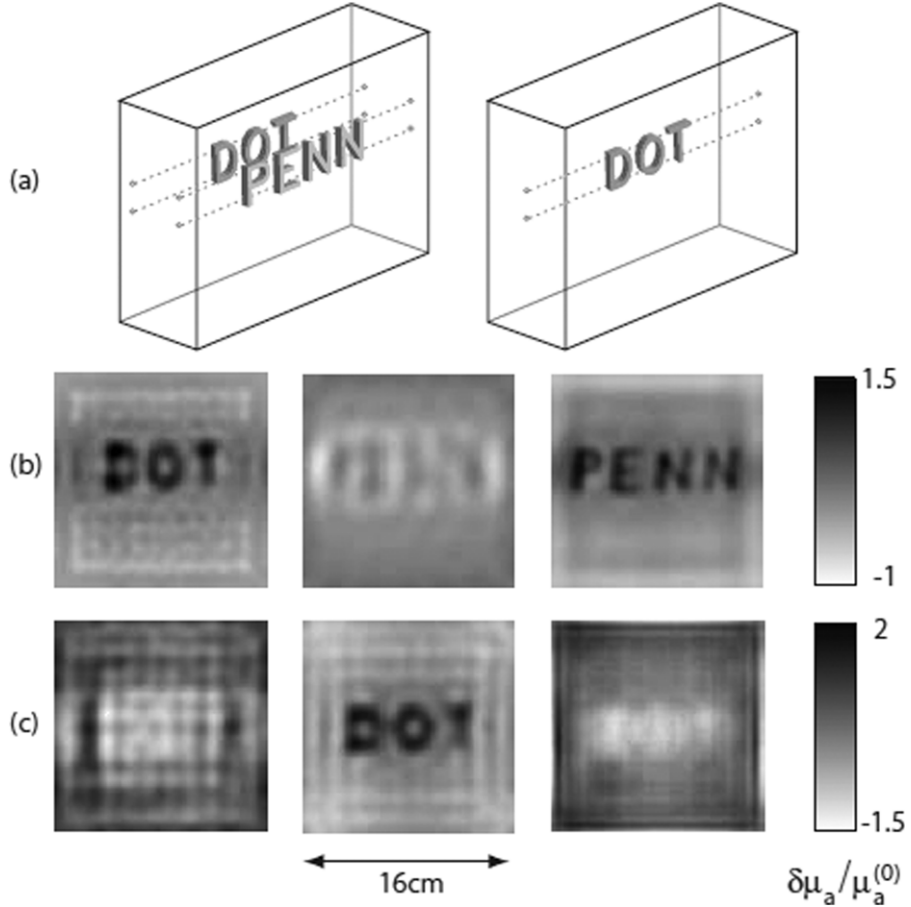


Figure 9. Slices from three-dimensional image reconstructions of the relative absorption coefficient ($\delta\mu_a/\mu_a^{(0)}$) for targets suspended in a 6 cm thick slab filled with highly scattering fluid. The Rytov linearized analytic inversion was used for this reconstruction. The three slices shown for each reconstruction correspond to depths of 1 cm (left), 3 cm (middle) and 5 cm (right) from the source plane. (a) Schematics of the positions of the letters during the experiments. Left: the target consists of letters ‘DOT’ and ‘PENN’ suspended 1 cm and 5 cm from the source plane, respectively. Right: the target consists only of the letters ‘DOT’ suspended 3 cm from the source plane. (b) Reconstructed image of the letters ‘DOT’ and ‘PENN’. (c) Reconstructed image of the letters ‘DOT’. (Reprinted with permission from [250]. Copyright 2008 Optical Society of America.)

(two each for the source and detector coordinates ρ_s and ρ_d) spatial Fourier transform, we obtain

$$\begin{aligned} \tilde{u}(\mathbf{q}_d, q_s) = & \int_{z_s}^{z_d} \kappa_A(\mathbf{q}_s, \mathbf{q}_d; z) v \delta \tilde{\mu}_a(\mathbf{q}_s + \mathbf{q}_d, z) \\ & + \kappa_D(\mathbf{q}_s, \mathbf{q}_d; z) \delta \tilde{D}(\mathbf{q}_s + \mathbf{q}_d, z) dz. \end{aligned} \quad (54)$$

Both κ_A and κ_D are known since we have analytic expressions for the coefficients defined in equation (53) and are given by

$$\kappa_A(\mathbf{q}_s, \mathbf{q}_d; z) = \zeta(\mathbf{q}_s; z_s, z) \zeta(\mathbf{q}_d; z, z_d), \quad (55)$$

$$\begin{aligned} \kappa_D(\mathbf{q}_s, \mathbf{q}_d; z) = & \frac{\partial \zeta(\mathbf{q}_s; z_s, z)}{\partial z} \frac{\partial \zeta(\mathbf{q}_d; z, z_d)}{\partial z} \\ & - \mathbf{q}_s \cdot \mathbf{q}_d g(\mathbf{q}_s; z_s, z) g(\mathbf{q}_d, z, z_d). \end{aligned} \quad (56)$$

These steps, collectively, reduce the original inverse problem to a linear one-dimensional integral equation which can be inverted in a manner similar to those mentioned in section 2.10.1 to obtain $\delta \tilde{\mu}_a(\mathbf{q}, z)$ and $\delta \tilde{D}(\mathbf{q}, z)$, which are the spatial Fourier transforms of the ‘images’ we seek to reconstruct (see [208] for details). Performing an inverse Fourier transform on $\delta \tilde{\mu}_a(\mathbf{q}, z)$ and $\delta \tilde{D}(\mathbf{q}, z)$ gives the desired images. Exploiting the planar symmetry this way dramatically

decreases the computation time relative to constructing the inverse for the entire Jacobian numerically (equation (43)).

For example, Konecky *et al* [250] used the Rytov linearized analytic inversion method to reconstruct objects of a complex structure (i.e. letters made from silicone rubber) with optical properties comparable to those of tissue embedded in an optically thick medium. In this study, reconstructions utilizing data sets of 10^7 source-detector pairs obtained with a CW instrument only required a minute of CPU time on a 1.3 GHz workstation. In addition to identifying the location and spatial extent of the heterogeneities, the resulting images contained spatially resolved features on the sub-centimeter scale at varying depths inside the optically thick medium (see figure 9).

2.10.3. Nonlinear numerical inversion (jacobian- and gradient-based methods). Linearized approaches are useful for generating images, but if the tissue optical properties are significantly different from those of a specified background, then the accuracy of the linear image reconstruction will be compromised. In section 2.10.1, we showed that the

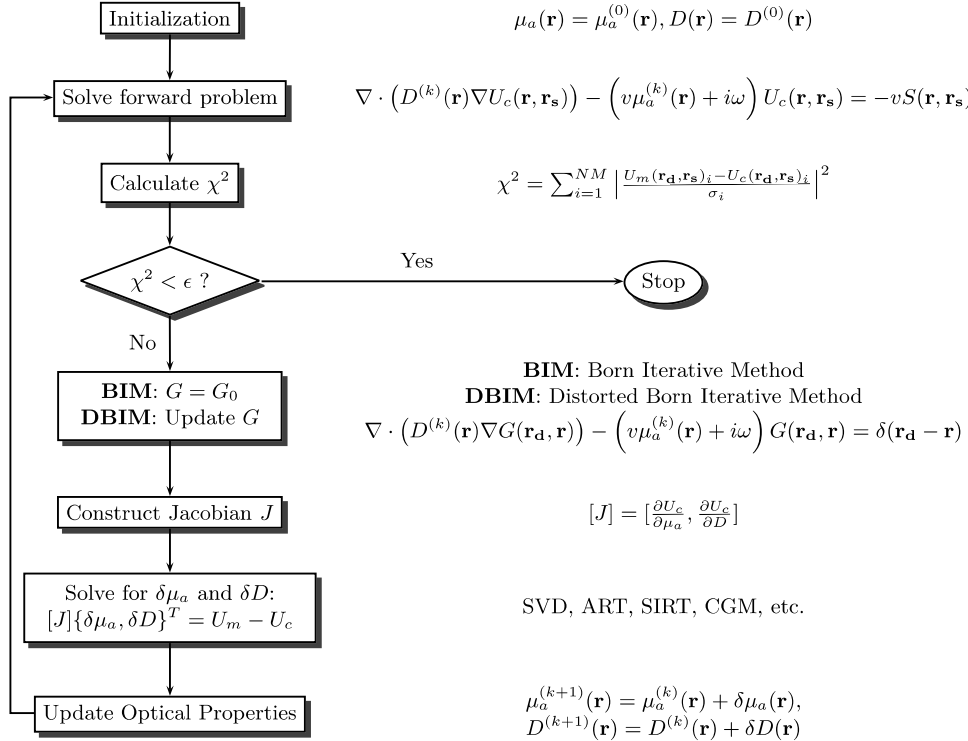


Figure 10. Flow chart of Born and distorted Born iterative methods. A linear inverse problem of the form $J\delta x = y$ is solved for each iteration. Both the fluence rate and Green's function are updated in the distorted born method, but only the fluence rate is updated in the Born iterative method (see text for details). The iterations continue until χ^2 has reached the desired tolerance.

linearized inverse problem in the Born approach ($U = U_0 + U_{sc}$) is valid if the magnitude of the fluence rate correction U_{sc} is small relative to the background U_0 . In the Rytov approach ($U = U_0 \exp[U_{sc}^R]$), the linearized inverse problem is valid if the fluence rate correction U_{sc}^R is slowly varying, i.e., $(\nabla U_{sc}^R)^2 \ll v\delta\mu_a/D$. In general, both of these linearized approaches break down when optical property perturbations are large. With the Born approach, this can easily be seen by noting that the derivation of equation (43) assumed small optical property perturbations [246]. When attempting to measure absolute optical properties of tissue, the specified background is an initial guess of these properties, which is often significantly different from the true properties. To improve image reconstruction, nonlinear approaches for the inverse problem are required. Jacobian-based nonlinear schemes in essence solve linear problems again and again, updating the perturbations $\delta\mu_a$ and δD iteratively, and then comparing calculated fluence rates with the measured fluence rates until they become sufficiently close.

Here, we will discuss a Born iterative method (BIM) and a distorted Born iterative method (DBIM) presented by Yao *et al* [182]. Figure 10 is a schematic illustrating the steps for these two methods. First, μ_a and D are initialized, and the corresponding Green's function, G_0 , for the photon diffusion equation (equation (44)) is determined. The forward problem is then solved; typically by using finite elements or finite-difference numerical methods. To quantify the agreement between calculated fluence rate $U_c(r_d)$ and the measured

fluence rate $U_m(r_d)$, an objective function χ^2 is constructed:

$$\chi^2 = \sum_{i=1}^{NM} \frac{(U_m(r_d, r_s)_i - U_c(r_d, r_s)_i)^2}{\sigma_i^2}. \quad (57)$$

Here NM is the number of measurements and σ_i is the measurement error for the i th source-detector pair. When χ^2 falls below some pre-defined convergence criterion ϵ , the iteration procedure is stopped. If the iteration procedure is not stopped, then the optical properties are updated. Updated optical properties are derived via the solution to an inverse problem which has been outlined already for the linearized problem in section 2.10.1 (i.e., equation (52)).

The difference between the two methods is that the DBIM method calculates a new Green's function at every iteration, while the BIM method always uses the same Green's function (see figure 10). The DBIM usually converges faster than the BIM, but it is also less robust to noise than the BIM [182]. Equivalent methods using the Rytov approach, i.e., the Rytov iterative method and the distorted Rytov iterative method, are also utilized.

Another useful nonlinear reconstruction approach employs a gradient-based iterative scheme rather than explicitly building the Jacobian and solving equation (52) [171, 189, 190]; in this case, the gradient of the objective function χ^2 (equation (57)) with respect to μ_a and D (e.g., $\frac{\partial \chi^2}{\partial \mu_a}$, $\frac{\partial \chi^2}{\partial D}$) is determined to establish a search direction to minimize χ^2 directly. A line search is performed to find the optical properties that minimize χ^2 along this search direction, and these

new optical properties are then used for the next iteration. The search direction is established using the nonlinear conjugate gradient method (see [171] for details). This process repeats until χ^2 has converged within a desired tolerance. Since the gradient-based approach does not involve direct inversion of the Jacobian matrix (time- and memory-consuming computational process), it is computationally less intensive than the Jacobian-based iterative methods under many conditions.

Public software packages are available that utilize the iterative methods described above for image reconstruction. Both the gradient-based and Jacobian-based approaches can be employed in the well-known DOT reconstruction package time-resolved optical absorption and scattering tomography (TOAST) [171]. NIRFAST is another software package written in the MATLAB environment that uses the Jacobian-based approach [117].

2.10.4. Nonlinear analytical inversion. The exact fluence rate solution to equation (11) can be written as an infinite series. For example, taking the Born approach, the series is generated by replacing U with $U_0 + U_{sc}$ in equation (45) and then substituting equation (45) in for U_{sc} in an iterative fashion, we obtain:

$$\begin{aligned} U(\mathbf{r}_d, \mathbf{r}_s) = & U_0(\mathbf{r}_d, \mathbf{r}_s) + G_0(\mathbf{r}_d, \mathbf{r}) F(\mathbf{r}) U_0(\mathbf{r}, \mathbf{r}_s) d^3 r \\ & + G_0(\mathbf{r}_d, \mathbf{r}) F(\mathbf{r}) G_0(\mathbf{r}, \mathbf{r}) F(\mathbf{r}) U_0(\mathbf{r}, \mathbf{r}_s) d^3 r d^3 r \\ & + \dots \end{aligned} \quad (58)$$

Here, $F(\mathbf{r}) \equiv (-v\delta\mu_a(\mathbf{r}) + \delta D(\mathbf{r})\nabla_r G_0(\mathbf{r}_d, \mathbf{r}) \cdot \nabla_r)/D_0$.

Equation (58) truncated at first order is the Born approximation. Inclusion of higher order terms in the series leads to more accurate results, but numerically evaluating the higher order terms is more computationally expensive [246]. However, for special geometries, symmetry properties of the fluence rate can be exploited for all of the higher order terms in a similar manner to the method described for the linear term in section 2.10.2. This scheme speeds up the reconstruction with higher order terms. Schotland and co-workers have derived an exact analytic inversion formula for the fluence rate written as an infinite series. For details about this approach, see [251, 209].

2.11. Fluorescence diffuse optical spectroscopy and tomography

The use of extrinsic near-infrared fluorescent dyes has gained attention recently, in part because of their potential to target specific tissues and in part because of their potential to provide information about tissue type and tissue micro-environment. Some researchers in the biomedical optics field recognized the potential of fluorescence early on [14, 204–252] and set about developing theoretical formalisms to understand these fluorescence signals in the multiple scattering limit; these theories have provided a framework to quantitatively assess the potential of fluorescent contrast agents and to use fluorescence for diagnosis. Proper inversion of fluorescent data to derive contrast agent concentration (or fluorophore lifetime

information), however, is more complication than DOS/DOT. It requires an understanding of the transport of excitation light and the transport of fluorescent light. Thus, most generally, a set of coupled equations for both diffuse light waves must be set up and solved.

Fluorescence diffuse optical spectroscopy (FDOS) is a fluorescence analog of NIR/S/DOS. Much of the theory for this relatively simple problem is fully developed (see, for example, [254, 256, 260]), and these theories have been applied in contexts such as photodynamic therapy [267, 268]. Similarly, the potential for contrast agents has stimulated the development and use of fluorescence diffuse optical tomography (FDOT) for imaging molecular-targeting probes in small animals [269–271], for sentinel lymph node tracking in animals and humans [272, 273], for imaging tumors in human breast [26, 274, 275], and for monitoring blood flow in human brain [276–279]. The feasibility of FDOS and FDOT in humans has thus been demonstrated.

In a related vein, phosphorescence lifetime spectroscopy and tomography have been introduced as a unique means to measure tissue parameters such as the partial pressure of oxygen [280–282]. Bioluminescence tomography of tagged molecules has been utilized to track physiological processes such as gene expression [283], and the autofluorescence from various components of tissue components has been studied in oncological contexts [284–287] and in neuro-imaging [288]. All of these applications require knowledge of the diffuse light transport problem.

2.12. Diffuse correlation tomography

Image reconstruction with temporal correlation functions, i.e., diffuse correlation tomography (DCT), employs essentially the same theoretical techniques as DOT for CW light, because the underlying mathematical models are formally similar. In general, such reconstruction schemes permit imaging of spatially heterogeneous dynamics. The inverse problem, in this case, must reconstruct the homogeneous and spatially varying blood flow index, $BFI(\mathbf{r}) = BFI_0 + \delta BFI(\mathbf{r})$, absorption, $\mu_a(\mathbf{r}) = \mu_{a0} + \delta\mu_a(\mathbf{r})$, and scattering, $D(\mathbf{r}) = D_0 + \delta D(\mathbf{r})$. Quite often the changes in BFI dominate the problem, making it reasonable to assume that $\delta\mu_a(\mathbf{r}) = \delta D(\mathbf{r}) = 0$ or in the case of hybrid instrumentation [76] to include them as inputs for the reconstructions.

The key difference between reconstruction with correlation functions versus reconstruction with the CW photon fluence rate is the correlation time dependence of G_1 . A simple practical approach selects a particular time $\tau = \tau^*$ for reconstruction of BFI from measured G_1 . Zhou *et al* developed a model for estimating the reconstructed image noise in DCT from the DCS noise information at each source-detector pair; it was found that the time τ^* that minimizes the DCT noise satisfies the relation $G_1(\mathbf{r}, \tau^*) = G_1(\mathbf{r}, 0)e^{-1}$ [78]. This approach thus optimized data selection for DCT by considering both the experimental noise and ill-posedness of the tomographic problem.

2.13. Metabolic rate of oxygen extraction

An important physiological parameter to monitor is the local metabolic rate of oxygen extraction. This quantity depends on the oxygen extraction fraction, i.e., the difference in oxygen saturation between the arterial and venous ends, and on blood flow. The cerebral metabolic rate of oxygen extraction (CMRO₂) has been studied extensively in the context of the brain and a wide range of models have been developed to estimate CMRO₂ from measurable quantities under different regimes [289–292].

A relatively simple model permits changes in CMRO₂ (*r*CMRO₂) to be calculated using a synthesis of *r*CBF, Hb and THC [76, 290–292]. In this case, a compartmentalized model of the vasculature is assumed and an equation that relates the measurable quantities is derived using Fick's law: CMRO₂ = OEF × CBF × C_a [293]. OEF is the normalized oxygen extraction fraction, i.e., the difference between oxygen concentrations in arterial (C_a) and venous ends of the vasculature. Our goal is to estimate OEF (or changes thereof) with optical data. Since NIRS/DOS measures a mixture of arteriole, capillary and venuole blood oxygen saturation and does not separate venous from arterial saturations, this task is non-trivial. We refer to this mixed signal as 'tissue blood oxygen saturation' (StO₂).

A compartmental model relates microvascular blood oxygen saturation to the percentage of blood in the venous and arterial components of the vasculature [77, 294]. We write StO₂ as a mixture StO₂ = k₁ × S_aO₂ + k₂ × S_cO₂ + k₃ × S_vO₂. Here, S_aO₂, S_cO₂ and S_vO₂ are the arteriolar, capillary and venous saturations, respectively, and k₁, k₂ and k₃ are the respective weights of each compartment to the total blood volume (k₁ + k₂ + k₃ = 1). A standard simplification is to represent S_cO₂ as a weighted average of the arterial and venous saturations; S_cO₂ = k₄ × S_aO₂ + k₅ × S_vO₂ where k₄ + k₅ = 1. The system can then be reduced to a two-compartment model [65, 66, 76, 77, 295] to estimate *r*CMRO₂:

$$\begin{aligned} r\text{CMRO}_2 &= r\text{OEF} \times r\text{CBF} \\ &= \frac{S_aO_2 - StO_2}{S_aO_{2bl} - StO_{2bl}} \frac{\gamma_{bl} S_aO_{2bl}}{\gamma S_aO_2} r\text{CBF} \\ &\approx \frac{S_aO_2 - StO_2}{S_aO_{2bl} - StO_{2bl}} \frac{S_aO_{2bl}}{S_aO_2} r\text{CBF}. \end{aligned} \quad (59)$$

StO₂ = HbO₂/(THC) is the microvascular blood oxygen saturation measured by NIRS/DOS. Sub-script 'bl' (bl) is used to indicate baseline values of a parameter. Baseline StO₂ (StO_{2bl}) and THC_{bl} are ideally measured but are often estimated from the literature values. Here γ is the percentage of blood in the venous compartment and if we assume that it remains constant over time, it divides out of our measures of *r*OEF. Thus, *r*CMRO₂ can be directly calculated from optical measurements of *r*OEF and *r*CBF.

3. Breast cancer imaging and spectroscopy

Approximately one in eight women in the United States will develop breast cancer, and, about 30% of these women will ultimately die of the disease [296]. Thus even

modest improvements in breast cancer screening (detection), diagnosis, and therapy monitoring can have huge impact in women's health. While existing clinical modalities have reduced the morbidity and mortality rates of breast cancer, no single diagnostic modality is suitable for the plethora of management problems that arise in the clinic. For example, accurate detection and characterization of tumors is required for screening and diagnosis, whereas predictions about treatment efficacy are important for therapy monitoring. X-ray mammography, a routine screening modality, has high false negative rate (i.e. missing cancers) in women under 50 years of age [297] and cannot be used too frequently due to the ionizing nature of x-ray radiation. Techniques such as ultrasound and magnetic resonance imaging (MRI) are sometimes employed in addition to x-ray mammography, but they have limitations such as high cost, low throughput, limited specificity (MRI) and low sensitivity (ultrasound). Most of these imaging modalities rely on the anatomical differences between cancer and healthy tissues. On the other hand, positron emission tomography (PET) relies on functional tumor contrast such as glucose metabolism and is recommended for assessing metastatic status. However, frequent measurements with PET pose problems due to its expense and the requirement of radioactive isotope injection. Thus new methods are needed to detect cancers earlier for treatment, to detect cancers missed by mammography [298–300], to reduce the false positive rate [301, 302] and to monitor tumor progression during cancer therapy.

Near-infrared diffuse optical tomography and spectroscopy are tools that rely on functional processes for contrast and therefore have potential to enhance sensitivity and specificity of breast cancer detection/diagnosis. Diffuse optical techniques are attractive, because they provide physiological information directly related to tumor vascularity and oxygenation, while utilizing inexpensive, non-ionizing, rapid, portable and non-invasive instrumentation.

A variety of instrumentation and algorithmic strategies have been developed for optical mammography and tumor monitoring. Instruments range from hand-held remission systems [303–308], to tandem-scanning systems [309–314] to full three-dimensional tomographic systems [106, 111, 315–320]. These instruments generally differ with respect to measurement geometry (e.g., remission, parallel-plate, ring/cone), detection type (e.g., CW, FD, TD), wavelength implementation (e.g., broadband versus discrete wavelengths) and source/detector numbers. Analysis algorithms vary too, ranging from analytic solutions in the homogeneous semi-infinite geometry to full fledged 3D tomographic reconstruction; algorithm choices must carefully consider clinical trade-offs in time and space against increased spectral- and spatial-content, and detection complexity for improved data fidelity.

3.1. Diffuse optical mammography based on endogenous contrast

3.1.1. Endogenous properties of normal breast tissue.

An understanding of normal breast optical properties is desirable,

even if one's ultimate goal is to probe cancer. Recent diffuse optical spectroscopic research on normal tissues has demonstrated sensitivity to tissue composition [321–328], which can change significantly with age or hormonal status. The subcutaneous breast tissues consist of adipose, glandular and fibrous stroma, and the blood supply is typically richest in the glandular areas [329]. Total hemoglobin concentration is thus expected to be larger in breasts with high glandular content and smaller in breasts with high adipose content. Since verification of actual breast composition for individual subject is difficult, we rely on surrogate markers such as body mass index (BMI) or mammographic parenchymal patterns for consistency checks. A significant inverse correlation between THC and BMI has been found, wherein high BMI is an indication of high adipose tissue content [320, 321, 323, 330]. Mammographic parenchymal patterns can be derived from the x-ray attenuation characteristics of fat (radiolucent) and epithelial and stromal tissues (radiodense) [331]. Cubeddu and co-workers have found that water and lipid content correlated well with the mammographic parenchymal pattern, which is an indicator of the composition of adipose and fibrous tissue content [330].

The observation that optical measurements of absorption and scattering can provide physiologically relevant information about breast tissue composition [323] has been extended in a new direction by Lilge and co-workers. Based on parenchymal pattern classification studies of x-ray mammography, it was found that women with dense tissue in more than 60–75% of the breast are at 4–6 times greater risk of breast cancer than others [331]. Using a principal components analysis of a broadband optical spectroscopy measurement, Lilge and co-workers have found agreement between the mammographic assessment of tissue density (high versus low) and optical measurements with 90% accuracy [332–334].

3.1.2. Breast cancer detection and characterization. Tissue properties accessible to DOT and DOS techniques are demonstrably different in tumors compared with normal tissues [213, 305, 309, 313, 315, 318, 320, 324, 325, 335–343]. Among various physiological parameters available to DOT and DOS, most groups have reported high THC contrast in malignant tumors [320, 324, 336, 337, 339, 343–347]. Since the malignant growth of tumors is often accompanied by sustained angiogenesis to supply oxygen and nutrient [348], THC might reasonably be expected to be higher in the cancers compared with normal tissues. Indeed, a positive correlation between microvessel density and THC has been found, providing further insight about the microscopic origin of THC contrast [336, 347, 349]. The rapid growth of many tumor cells can also give rise to an increase in number density of subcellular organelles (e.g., mitochondria, nucleolus), which in turn affect tissue light scattering coefficients. Mean size and volume fraction of the nucleus and nucleolus measured by microscopy have indeed been correlated with light scattering observations by DOT [350], and some groups have reported tumor-to-normal contrast in tissue scattering parameters [122, 341, 344, 345, 347, 350].

Information about tumor oxygenation status is important, especially for predicting the efficacy of cancer therapies [351–353]. However, while it has been hypothesized that malignant cancer would exhibit low oxygenation due to hyper-metabolism [305], its manifestation in macroscopic DOT measurements has not been apparent. Some groups have observed a decrease of StO₂ in the tumor [305, 343, 354–357] whereas others observed no difference [122, 320, 340–342, 358, 359] or even an increase [344]. This discrepancy may be due to dependence of cancer oxygen metabolism on the cancer stage, type, biochemical pathways or differences in oxygenation accuracy sensitivity among systems.

The spatial locations of tumors based on optical contrast have been compared with x-ray mammograms/ultrasound [313, 320, 336, 350, 360, 361], and MRI [122, 362, 363]. Since optical and other imaging measurements were performed with different compression geometries, new image coregistration schemes [364] and algorithms [340, 365, 366] have been developed for quantitative comparisons between different imaging modalities. It was demonstrated that the spatial locations of optical tumor contrast agree with those identified by MRI and/or PET, and the extracted tumor physiological contrast parameters from optics have been shown to be correlated with PET parameters [366].

Ultimately, characterization of a new imaging modality can be established through computation of receiver operating characteristic (ROC) curve [367, 368]. Let us suppose that there is a parameter (X) from new imaging modality whose value seems to be higher for malignant lesions and lower for benign lesions. (Note: depending on the test, one can easily substitute ‘healthy’ or ‘non-diseased’ state with ‘benign’.) For each value of the threshold value ($X_{\text{threshold}}$), all the lesions under consideration can be grouped into the following four categories. Some lesions are indeed malignant and correctly predicted to be malignant by the new modality (true positive; TP); some lesions are malignant, but incorrectly predicted to be benign (false negative; FN); some lesions are benign, and correctly predicted to be benign (true negative, TN); and some lesions are benign, but incorrectly predicted to be malignant (false positive; FP). These quantities can be expressed as rates by dividing by the total number of true malignant lesions or true benign lesions: for example, true positive rate $\text{TPR} = \text{TP}/(\text{TP} + \text{FN})$ and false positive rate $\text{FPR} = \text{FP}/(\text{TN} + \text{FP})$. The ROC curve is constructed by plotting true positive rate on the horizontal axis and false positive rate on the vertical axis at different $X_{\text{threshold}}$. A perfect test establishes a threshold which separates diseased and non-diseased subjects completely, i.e., the true positive rate is 1 and the false positive rate is 0. A useless test is one in which diseased and non-diseased states have the same probability (i.e., 50/50 chance) regardless of the threshold; in this case the ROC curve has slope of unity. Thus, a larger ‘Area under ROC curve’ (AUC) implies a better test/method. AUC of 50% corresponds to an ROC slope of unity (i.e., a useless test). Chance *et al* [305] used a threshold based on a combination of relative THC and StO₂ (derived by DOS) of tumors compared with the tissue from the contralateral breast and obtained

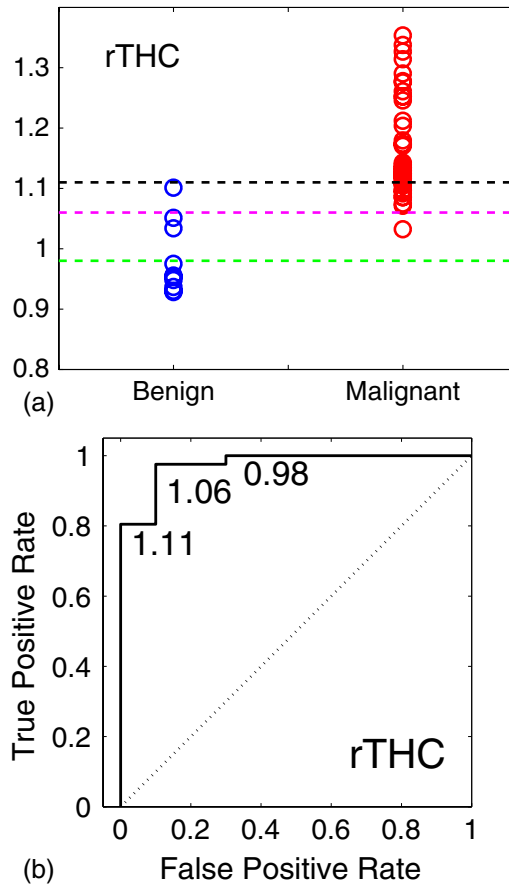


Figure 11. (a) Tumor-to-normal ratio of total hemoglobin concentration ($r\text{THC}$) of 10 benign and 41 malignant lesions. (b) Receiver-operating-characteristic curve for $r\text{THC}$ showing true positive rate for malignant lesions versus false positive rate for benign lesions. (Reprinted with permission from [122]. Copyright 2009 SPIE.)

95% AUC to discern cancer from normal tissue. Poplack *et al* [369] achieved 88% AUC for differentiating cancer from normal tissue, and 76% AUC for differentiating malignant cancer from benign lesions using $r\text{THC}$ derived from 3D DOT images for a subset of subjects with lesions larger than 6 mm; their AUC decreased when smaller lesions were included in the data set. In recent work from our laboratory [122], we have extracted the optical parameters from 3D reconstructed images based on MRI-guided region-of-interest selection. As seen in figure 11, there is a clear distinction between benign and malignant lesions in tumor-to-normal ratio of THC with AUC higher than 90%. Similar trends were seen in tumor-to-normal contrast of HbO_2 and the tissue scattering coefficient. While AUCs of DOS/DOT are relatively high, showing the potential of DOS/DOT for differentiating malignant tumors from healthy or even benign tumors, the optical methodology needs more assessment since the number of subjects is still low compared to other imaging modalities.

At this point in time, these findings do not represent a final assessment of DOT performance. Most often, each study focused on demonstration of a particular methodology. Discrepancies among groups can be a function of method, subject groups (e.g., lesion size, percentage of benign and malignant lesions, etc) and lack of large-scale, blinded clinical

trials. Clearly much work remains, but promise has been demonstrated.

3.2. Optical mammography based on exogenous contrast

DOT can be conducted concurrently with injection of exogenous contrast agents. With the use of exogenous contrast dyes tumor contrast can be improved as a result of tissue-dependent spatial distributions of the dyes and dye lifetimes [24, 25]. Currently, ICG is the only FDA-approved compound suitable for DOT, having an absorption and fluorescence spectra in the NIR window. ICG has been demonstrated to enhance absorption of human breast cancer *in vivo* [335, 370, 371].

In principle, fluorescence signals can provide greater detection sensitivity and specificity compared with absorption signals. Fluorescence signals also provide access to new information about tissue micro-environment, such as pO_2 , pH and intracellular calcium concentration [372, 373].

Sevick-Muraca and co-workers have demonstrated fluorescence imaging using ICG in canine breast cancer [258] and in realistic breast phantoms [374]. In our laboratory, we have recently demonstrated the first 3D fluorescence diffuse optical tomography (FDOT) of *in vivo* human breasts and breast cancer [26]. In figure 12, one example of FDOT is given. Endogenous optical signals and fluorescence signals from ICG injection were measured from a 46-year-old pre-menopausal female diagnosed with invasive ductal carcinoma. Selected slices from 3D DOT reconstructions of endogenous optical properties (i.e., THC, StO_2 , μ_s) and 3D FDOT reconstruction of ICG concentration exhibit large contrast. In a volume that was confirmed to be the tumor region by Gd uptake and radiology reports, the reconstructed THC, μ_s and ICG concentrations were higher and StO_2 somewhat lower than the surrounding tissue. When we take 3D isosurface images of THC, μ_s and ICG concentration contrast with iso-values set to three standard deviations above their means. The isosurfaces of the three contrasts overlay quite well, and the volumetric differences may be due to real tissue physiology variation. Other groups have now started to report more cases of *in vivo* FDOT in human patients with enhancement of tumor contrast [274, 275].

3.3. Therapy monitoring

Neoadjuvant (i.e., pre-surgical) chemotherapy is an important therapeutic approach for women with locally advanced breast cancer that can increase long-term survival. Typically, such breast cancers are large (e.g., larger than 5 cm) and many anticipated responses to drugs are vascular in nature. For treatment optimization, it is desirable to monitor tumor responses during this process. For example, alterations in tumor biology and physiology can be seen early following cytotoxic chemotherapy and can be a marker of tumor response. Dynamic contrast enhanced MRI (DCE-MRI) has been used to monitor the change in both tumor size and vascularity following pre-operative (neoadjuvant) chemotherapy in patients with locally advanced breast cancer [375–377]. Results demonstrate that even before clinical

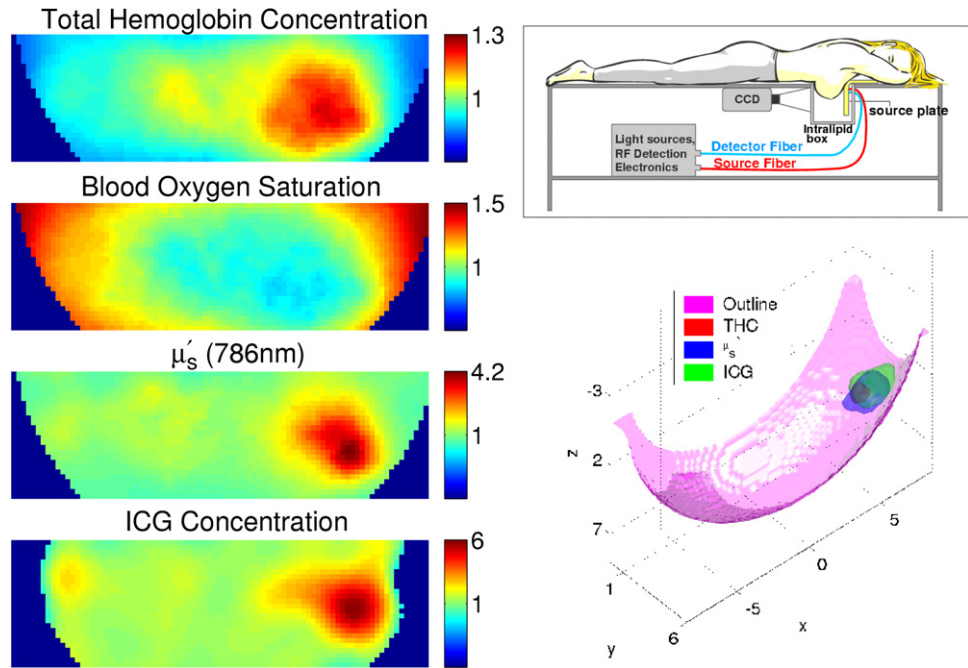


Figure 12. A case of 3D optical tomography of breast with malignant cancer is shown with both endogenous (relative total hemoglobin, relative blood oxygen saturation and relative tissue scattering) and exogenous contrast images (relative Indocyanine Green concentration measured from fluorescence) (left). On the top right, a parallel-plane DOT instrument and measurement geometry are illustrated. The isosurface diagram on the bottom right shows the volumetric extent of the observed tumor for each optically derived parameter. (Reprinted with permission from [26]. Copyright 2007 Optical Society of America.)

or imaging evidence of tumor shrinkage are measurable, changes in tumor vascularity can be seen through blunting of the dynamic enhancement curve following intravenous administration of gadolinium contrast agents. Furthermore, positron emission tomography (PET) has found that metabolic changes of cancer due to cancer therapy can precede morphological changes by up to eight days [378, 379]. DCE-MRI and PET, however, are expensive and are not practical for frequent monitoring.

The feasibility of applying diffuse optical techniques in the context of cancer therapy monitoring has been demonstrated successfully in imaging instruments [340, 349, 380, 381] and with hand-held probes [84, 324, 382]. Thus far, tumor size and/or properties (e.g., THC, HbO_2 , water) detected by diffuse optical methods have correlated well with patient response to chemotherapy (i.e., complete, partial or none) [380–382].

3.4. Outlook: optical mammography

The field of diffuse optics, as applied to breast cancer imaging and monitoring, is rapidly evolving. Innovative instrumentation and reconstruction algorithms have been developed and combined to improve image fidelity, and these factors continue to improve over time. In addition, more statistics from *in vivo* breast cancer data provide insight into the biological issues and guidance for more directed instrumentation and algorithm development.

Spatial resolution and detectability are two major concerns about optical mammography. In general, these factors depend on the size and contrast of the heterogeneities we investigate. To date, a few groups have demonstrated that the tumors of

order 1 cm are readily detectable with excellent sensitivity and specificity based on, for example, total hemoglobin concentration contrast [122, 305, 369]. Tumor sensitivity and specificity decrease as the lesion size becomes smaller [369], with 4–7 mm being the state-of-the-art resolution demonstrated in tissue phantoms at tumor-to-normal ratios of 2× to 4× [250]. The resolution of a DOT system depends on the many factors, such as the number of sources and detectors, the field of view covered by the optodes and optode spacings, the tissue volume to be reconstructed, the depth of target (e.g., tumor), the target-to-background contrast, the presence of *a priori* spatial or spectral information and fundamentally on the physics of photon propagation in tissues [229]. While the current level of DOT resolution poses some barriers for its use as a stand-alone imaging modality for cancer screening, cancer detectability is not necessarily limited by resolution and can be utilized in complementary fashion with other imaging modalities in tumor detection and diagnosis. Strategies to further improve detectability and/or resolution are (1) to find other optical contrast related to tumoral physiological changes, (which may even occur before angiogenic changes) (2) to use anatomical constraints given by other imaging modalities to improve DOT resolution and (3) to enhance tumor-to-normal contrast based on molecular-targeted (fluorescent/absorption) probes.

In the search for optical contrast to enhance differentiation between tumor and normal tissues, research groups are employing broader wavelength ranges to explore water, lipid and collagen concentrations, bound water fraction and refractive index [311, 312, 347, 357, 359, 383–385]. Some of the most recent investigations have found that water

concentration is higher in tumors compared with normal tissues [311, 312, 347, 357, 359], that lipid concentration is lower in tumors compared with normal tissues [311, 359], that the bound water fraction [383] and refractive indices [385] may provide novel tumor contrast as well. In addition, using diffuse correlation spectroscopy, experimenters have found that blood flow in breast cancer is larger than in normal breast tissues [84, 86].

Several groups have incorporated concurrent optical measurements with other imaging modalities. The multi-modal approach can potentially overcome structural resolution limitations of DOT, using the spatial information provided by other imaging modalities to constrain the DOT inverse problem. This multi-modal approach also provides extra physiological information for the other imaging modalities. Thus far advances have been made in three fronts: concurrent measurements with MRI [335, 370, 386–390], 3D x-ray mammography [213, 391, 392] and ultrasound [339, 346, 349, 381, 393–395].

The most effective clinical role for diffuse optical tomography in the screening, diagnosis and treatment monitoring of breast cancer has yet to be determined. It is clear, however, that DOT and DOS provide exquisite functional information directly related to tumor pathophysiology (e.g., metabolic activity, angiogenesis, and blood flow/concentration), and complementary to structural and functional information provided by conventional imaging. Furthermore, advances in diffuse optical tomography of breast are critical for exploitation of the advances of molecular imaging [24, 269, 270], an emerging field of medicine with promise of new generation optical contrast agents. Photo-acoustic, optical mammography was also recently reported [396].

4. Optical monitoring of cerebral hemodynamics

4.1. Clinical relevance of diffuse optics for cerebral hemodynamics

The ability to measure cerebral hemodynamic responses to stimuli has important implications in fundamental neuroscience, clinical modeling and the clinic. A key concept in the field concerns the coupling between functional stimulation and regional changes in cerebral blood flow (CBF). This phenomenon is often referred to as activation flow coupling (AFC). AFC has been known for over a century but is still poorly understood [397–400]. Since most neuro-imaging methods rely on AFC as an indicator of neuronal activity, a detailed characterization of AFC under normal conditions improves understanding of normal as well as pathological brain physiology, and it permits us to relate hemodynamic quantities to neuronal activity.

Hemodynamics play other crucial roles in the brain. Cerebral well being is dependent on adequate and continuous delivery of oxygen and on the clearance of the by-products of oxygen consumption, e.g., carbon dioxide. In a simplistic picture, oxygen-saturated red blood cells (RBCs) are pumped through the arterial network to smaller vessels

and into the microvasculature. Tissues are perfused by the microvasculature. Oxygen exchange occurs by diffusion at the microvascular level and the by-products are cleared, along with oxygen depleted RBCs, on the venous side (see section 2.13). In general, this phenomena is tightly autoregulated by a variety of processes, including changes in the vascular resistance [401], to maintain constant blood perfusion in spite of changes in local pressures and other factors (see figure 15 inset). In brain, local perfusion pressure (i.e., ‘cerebral perfusion pressure’ (CPP)) is defined as the difference between the mean-arterial pressure (MAP) and the intracranial pressure (ICP). It is very difficult to monitor cerebral autoregulation in clinical settings. ICP can be monitored by invasive probes [402], but in many populations, clinicians prefer not to accept the risks of invasive probes; in this case MAP and neurologic signs are utilized as surrogate markers for ICP.

Microvascular CBF is particularly difficult to measure at the bedside. To date many attempts have been made to measure CBF, all with unique advantages and disadvantages. Below, we list some of the major modalities employed in the clinic; research only modalities, which are very promising but not yet widely utilized are not included in the list [403]:

- (i) Laser speckle techniques such as laser Doppler flowmetry (LDF) rely on physical principles similar to those of DCS [50]. These techniques can measure microvascular CBF. However, practical problems in detection and overly simplified modeling largely restrict the use of LDF to the single scattering and limit its uses to about ~0.5 mm below the tissue surface (see section 1). Therefore, the skull must be removed to access the brain, and clinical applications are limited to intraoperative measurements [404–406]. Recent developments now permit penetration up to ~5 mm in skeletal muscles [407], but the technology is not yet useful for non-invasive, transcranial monitoring. Another variant of the method, laser speckle flowmetry (LSF) using a CCD camera, has recently been introduced to examine cerebral hemodynamics in rodents [408, 409]. It has not yet been widely commercialized, however, and its application in humans is limited to measurements during open-skull surgery [406].
- (ii) Doppler ultrasound uses the frequency shifts in an ultrasound beam to image blood flow. However, due to technical issues only the proximal portions of the intracranial arteries can be insonated. Thus far the ultrasound method has only been used to measure blood flow velocity through large vessels, i.e., macrovascular blood flow velocity [410, 411]. Furthermore, since velocity changes predict CBF variation only if vessel diameters do not change, transcranial Doppler ultrasound (TCD) has limited utility in important clinical applications such as stroke evaluation [412], with its success arising in patients with proximal arterial occlusions [413]. Nevertheless, TCD remains a primary clinical modality for serial monitoring of CBF at the bedside.
- (iii) Arterial-spin labeling MRI (ASL) [414–416] and flow-sensitive alternating inversion recovery MRI (FAIR) [417, 418] are two modalities of magnetic resonance imaging (MRI) sensitive to perfusion/flow that have

- been used extensively in the brain. Additional MRI modalities are available for perfusion measurements, but they require bolus injections. Although these MRI methods offer a ‘full-head’ imaging capability and can readily be co-registered with the high-resolution anatomical information of MRI and other functional MRI modalities (e.g., blood oxygen level dependent, BOLD), their use in clinical settings is limited. For example, the presence of strong magnetic fields makes them difficult to use in intensive care units, and their low throughput relegates their use to a single-shot measurement where the patients are transferred into the magnet for one \sim 30–60 min observation. Furthermore, the instruments and instrument time are expensive. Some difficulties also arise from patient specific problems; for example, it is sometimes difficult to hold infants still, and some patients are claustrophobic.
- (iv) Xenon computed tomography (xenon CT) is used in the clinic for measurements of ‘full-head’ maps of cerebral blood flow [419, 420]. The modality dynamically scans the head using a CT system while the patient inhales xenon gas. The method is gaining acceptance as a complementary modality in some intensive care units, i.e., in preference over MRI and PET modalities. As in the case of MRI, however, the use of xenon CT is limited to few time points, even though quasi-portable variants are available to reduce patient transport issues. Finally, the instrument and the xenon gas are quite expensive, and xenon gas is also known to alter CBF which makes quantification more difficult.
- (v) Positron emission tomography (PET) is a diagnostic modality that offers direct measurements of a variety of physiological parameters including blood flow [421], glucose metabolism [422] and oxygen metabolism [421]. However, use of radioactive materials limits its applicability in many clinical settings such as the intensive care unit [423]. PET shares problems with MRI and xenon CT as per expense, availability, patient discomfort and limitations for long-term monitoring. Finally, PET requires injection and/or inhalation of chemicals and uses radioactive materials.

Clearly, an optimal method for hemodynamic monitoring has yet to be developed. A strong need exists for an inexpensive, continuous, non-invasive instrument for measurement of CBF and the technologies described in this review offer a great deal of promise along these lines. Diffuse optical tomographic and spectroscopy (i.e., DOT and DOS) methods have been demonstrated to measure blood volume, blood oxygenation and changes thereof, in research and clinical settings; in addition, through some maneuvers, it is also possible to employ DOS/DOT for the measurement of blood flow. DOS/DOT has been particularly successful in infants [144, 424–430]. The development of DCS has had even more impact, however, because it permits clinicians to measure several hemodynamic parameters independently with non-invasive probes (i.e., the hemoglobin concentrations and the blood flow), thus permitting estimation of changes in oxygen metabolism.

The primary advantages of diffuse optics for monitoring cerebral hemodynamics in the clinic are as follows:

- (i) The technique is non-invasive and involves no risk to the patient (e.g., no ionizing radiation, no gases to be inhaled or drugs to be injected).
- (ii) The technique samples and reports results in real time.
- (iii) The technique can track changes over long periods (hours to days), in contrast to single-time-point modalities (e.g., MRI, PET, xenon CT).
- (iv) The technique can sample more than one spatial location, permitting examination of regional differences in the brain.
- (v) The technique can be employed at the bedside; critically ill patients need not be moved.
- (vi) The technique is applicable to measurements patients of all ages, from pre-mature born infants to adults.
- (v) The instrumentation is relatively inexpensive and the per-measurement costs are minimal.

Diffuse optical measurements also have limitations: relatively short penetration beyond the skull/scalp, relatively coarse spatial resolution, limited structural/morphological information which makes partial volume effects more difficult to account for and difficulties with the assignment of absolute optical properties. Furthermore, as with any new modality proposed for clinical use, diffuse optical monitors must demonstrate clinical utility in large, controlled trials before mainstream acceptance is assured. For applications in neurology, portable devices that monitor hemodynamics in large tissue volumes are popular due to the relative simplicity of the instrumentation and analysis algorithms, and due to simple, comfortable probe heads. Several topographic (2D) and tomographic (3D) imagers are used now to map hemodynamic changes locally or globally [431, 432], and various approaches ranging from dense probe designs to utilization of secondary data have been considered to optimize the spatial resolution [135, 433]. Given these pros and cons, we now consider clinical applications at the present state of diffuse optics technology.

4.2. Selected translational results

Optical imaging—ranging from microscopy methods to diffuse optics—has found a myriad of applications in brain imaging [431, 432]. It is beyond the scope of this review to describe this wide-ranging field. Here we limit our discussion to those translational applications wherein diffuse optical methods are used in the clinic.

Broadly speaking, two groups of studies have been employed: (1) those using commercial devices [432] and (2) those using state-of-the-art research devices and algorithms [432].

Thousands of commercial instruments are currently in use with a rapidly increasing number of studies being published as a result [432]. Unfortunately, some of these studies have been done without state-of-the-art instrumentation and/or algorithms, and over the years, the lack of optimized methodology has led to some debate over the utility of

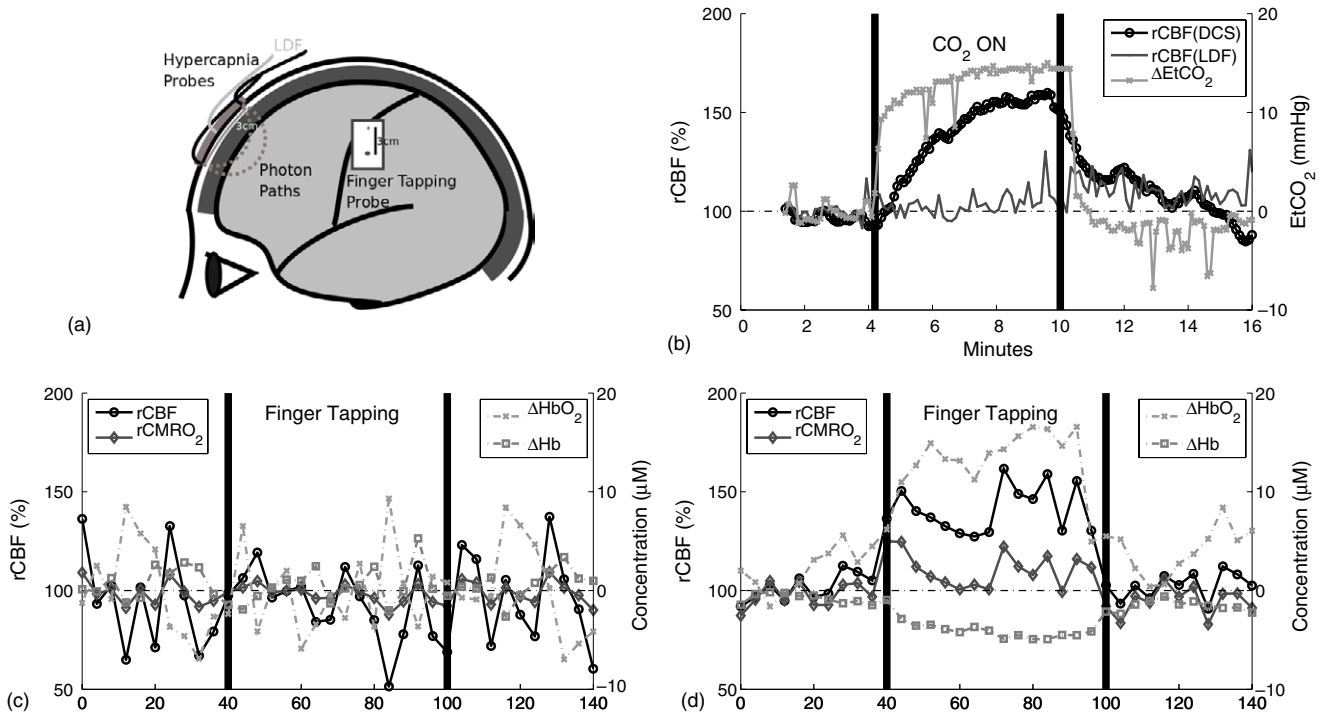


Figure 13. (a) Schematic showing placement of probes used for hypercapnia (frontal) and sensorimotor (side) studies. For the frontal probe, a laser Doppler flowmetry (LDF) probe was placed mid-way the source and detector fibers to record scalp blood flow. (b) Increased CO₂ breathing (hypercapnia) results in significant increases in end-tidal CO₂ (EtCO₂) and blood flow in brain (*r*CBF(DCS)) but only a negligible amount in scalp blood flow (*r*CBF(LDF)). (c)–(d) Hemodynamic response to finger tapping when the probe is placed (c) away from the contralateral sensorimotor cortex and (d) when its placed on the contralateral sensorimotor cortex. (Reprinted with permission from [66]. Copyright 2004 Optical Society of America.)

(particularly) NIRS/DOS [434–436]. We believe that NIRS/DOS and related techniques offer a great deal of promise and with improvements in technology and improvements in physical understanding about photon propagation through tissues and its modeling, the utility of NIRS/DOS will rapidly become more apparent. Commercial systems are, indeed, crucial for the clinical penetration of the technology, but until large-scale clinical trials have been performed, instrumentation needs to be handled as research tools. At this point, at least three [432] devices have the USA Food and Drug Administration's approval for use in patient populations.

Amongst many potential applications, NIRS/DOS has been utilized for cerebral monitoring of adults with traumatic brain injury (TBI) and subarachnoid hemorrhage (SAH) [437–442], ischemic stroke [80, 276–279, 443–450] sleep apnea and other sleep disorders [451–454], intraoperative brain monitoring [455, 456] and in neonates and children [430, 457–459]. This list is not exhaustive; it is meant to give a ‘flavor’ of the field. Over the years, NIRS/DOS has been utilized for a very wide range of applications, but unfortunately largely for feasibility demonstrations.

4.2.1. Hemodynamics of healthy brain. Figure 13(a) shows a schematic and data from two studies conducted in our laboratory [65, 66]. Here we have combined NIRS/DOS and DCS methods in a hybrid instrument [65, 77]. For NIRS/DOS, three, amplitude modulated (70 MHz, ‘frequency-domain’) lasers operating at 690, 785 and 830 nm were employed as

light sources. A photomultiplier tube (PMT) was used as a detector and its output was fed to a radio-frequency, homodyne, I&Q demodulation electronics box which calculated the relative amplitude and phase [460]. NIRS/DOS data were analyzed using the ‘differential pathlength factor’ (DPF, see section 2.8.2) formulation [143]. For DCS, a long coherence length, continuous-wave laser was used as a source. Eight photon-counting, fast avalanche-photodiodes (APDs) and a multi-channel autocorrelator board was used. DCS data were analyzed using a semi-infinite medium solution (see section 2.9.3) [65, 76, 77]. The fiber optics from the two devices were mounted on the same probe and were time shared; data were acquired in an interlaced sequence by utilizing optical switches.

Figure 13(b) shows data from a hypercapnia experiment wherein we have measured the CBF response to increased carbon dioxide (CO₂) breathing. We measured CBF in five subjects at rest, and during 4–6 min periods of increased cerebral carbon dioxide induced by breathing a 6% CO₂ gas mixture. In healthy subjects, hypercapnia causes a well-defined increases in CBF [461]. We observed a sustained increase in mean CBF of $35.4 \pm 9.6\%$, and an accompanying increase in EtCO₂ of 14.7 ± 4.7 mmHg. This relative rate corresponds to a $2.4 \pm 0.4\%$ CBF increase per mmHg of EtCO₂, a number well within the literature values (i.e., 2–3.6%/mmHg). During this investigation we also placed a laser Doppler probe on the scalps of a subset of volunteers. The probe enabled us to directly compare CBF measured by DCS with scalp flow measured by laser Doppler flowmetry (LDF)

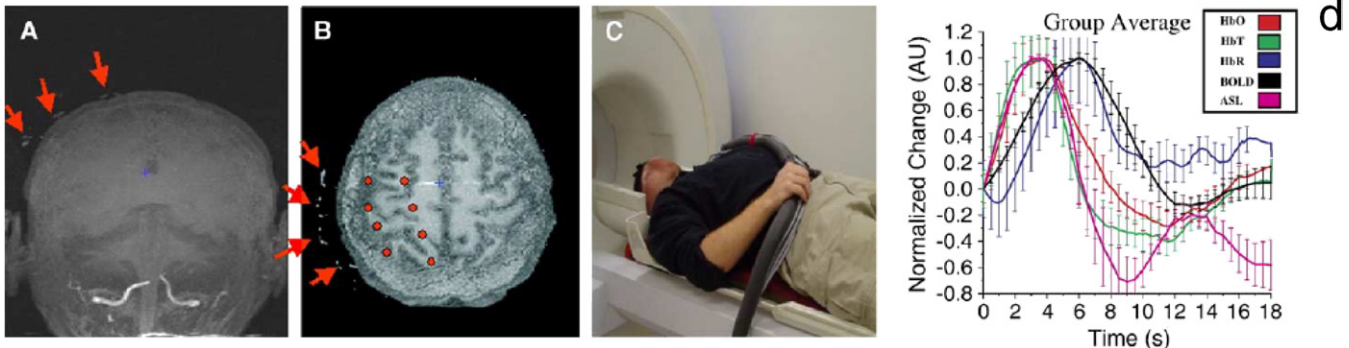


Figure 14. (a)–(b) Morphological MRI scans showing location of fiducial markers indicating the location of NIRS/DOS probe which is then overlaid onto BOLD and ASL scans to define ROIs. As shown in (c), an MRI compatible NIRS/DOS probe was used for simultaneous data acquisition. (d) Group averaged responses from simultaneous ASL, BOLD and NIRS/DOS studies. Temporal evolution of NIRS/DOS measures of THC and HbO₂ agree with ASL and Hb agrees with BOLD. Note how ASL, THC and HbO₂ maxima are earlier than BOLD and Hb maxima. Hb curve is shown inverted. (Reprinted with permission from [471]. Copyright 2006 Elsevier.)

during activation. Figure 13(b) shows these measurements for one subject, along with measured EtCO₂. Note that the scalp flow signal is small compared with CBF measured by DCS and largely unchanged with changes in EtCO₂ (right vertical axis). These studies demonstrate the DCS signal does not arise from changes in scalp blood flow, but some contamination is inevitable.

Figures 13(c) and (d) show data from an experiment where the subject was asked to carry out a task that would stimulate the sensorimotor cortex [66]. First, we localized the hand sensorimotor cortical area contralateral to the dominant hand according to the 10–20 system [462]. The probe (figure 13(a)) was placed and secured over this region. For the activation period, the subject was instructed to tap index and middle fingers against the thumb at 3 Hz. A blocked design of fifteen such stimuli was used. In order to illustrate the local nature of the observed response, we have also taken data where the whole process was repeated with probe placed ~2 cm frontal to the sensorimotor cortex. Figure 13(c) shows the results of one such study. None of the observed quantities show any changes that are correlated with the stimuli despite the fact that stimuli were presented during the time period shown by vertical bars. Figure 13(d) shows the population averaged results from seven subjects; a robust change correlated with the activation was observed in all quantities. Mean changes observed were $39 \pm 10\%$ for rCBF, $12.5 \pm 2.8 \mu\text{M}$ for HbO₂, $-3.8 \pm 0.8 \mu\text{M}$ for Hb, $8.3 \pm 2.3 \mu\text{M}$ for THC and $10.1 \pm 4.4\%$ for rCMRO₂. rCBF changes are well within the range of values determined by MRI [463, 464], [²H ¹⁵O] PET [465], [¹³³Xe] [466] and [¹¹CH₃] PET [467] for similar measurement stimuli, i.e., 21–60%. Mean oxy-, deoxy- and total-hemoglobin changes agree quantitatively with increases reported by BOLD of 2–4% [463, 468]. The increase in CMRO₂ is within the range of values (9–29%) from hybrid MRI measurements [463]. The ratio of rCBF to rCMRO₂ is also agreement with data reported by hybrid MRI techniques [463, 469] which range from two to four.

Overall, these results demonstrate the ability of NIRS/DOS and DCS to probe local changes in cerebral hemodynamics.

4.2.2. Diffuse optics versus fMRI. Since NIRS/DOS and DCS both employ fiber optics to deliver and detect light, they are readily adaptable for use concurrently in the MRI magnet using MRI compatible probes and long optical fibers. This permits cross-validation studies, as well as utilization of MRI derived spatial information for diffuse optical data analysis. In a series of papers, Boas and co-workers have compared NIRS/DOS with BOLD and ASL-MRI; in so doing, they have also developed models to describe the physiological origin of the BOLD signal, to account for partial volume effects in NIRS/DOS signals and to derive composite models to estimate rCMRO₂ [470–475].

Here we highlight one study [471] that compares the temporal properties of NIRS/DOS signals with BOLD and ASL-MRI. As shown in figure 14, the temporal evolution of NIRS/DOS determined THC and HbO₂ agree with ASL-MRI and Hb agrees with BOLD. Notice how ASL-MRI derived CBF, THC and HbO₂ maxima arise earlier than BOLD and Hb maxima. Hb and BOLD are strongly correlated while THC and BOLD exhibit a weaker correlation, in agreement with biophysical models for the BOLD signals. It has long been assumed that NIRS/DOS measures of THC (or blood volume) would correlate with CBF under many circumstances. These results explicitly demonstrate strong correlation between these signals.

4.2.3. Longitudinal bedside monitoring. One of the most promising applications of diffuse optics is at the bedside for longitudinal monitoring of cerebral hemodynamics. To demonstrate this idea and to test the feasibility of hybrid NIRS/DOS-DCS measurements on a critically ill population of acute, ischemic stroke patients, we have induced orthostatic stress by changes in head-of-bed positioning as shown in figure 15 [80]. Our hypothesis was that in response to this challenge, the impaired cerebral autoregulation would lead to larger changes in cerebral hemodynamics in the infarcted hemisphere by comparison with the ‘healthy’, contralateral hemisphere.

To this end, diffuse optical measurements were obtained from patients with acute hemispheric ischemic stroke ($n = 17$,

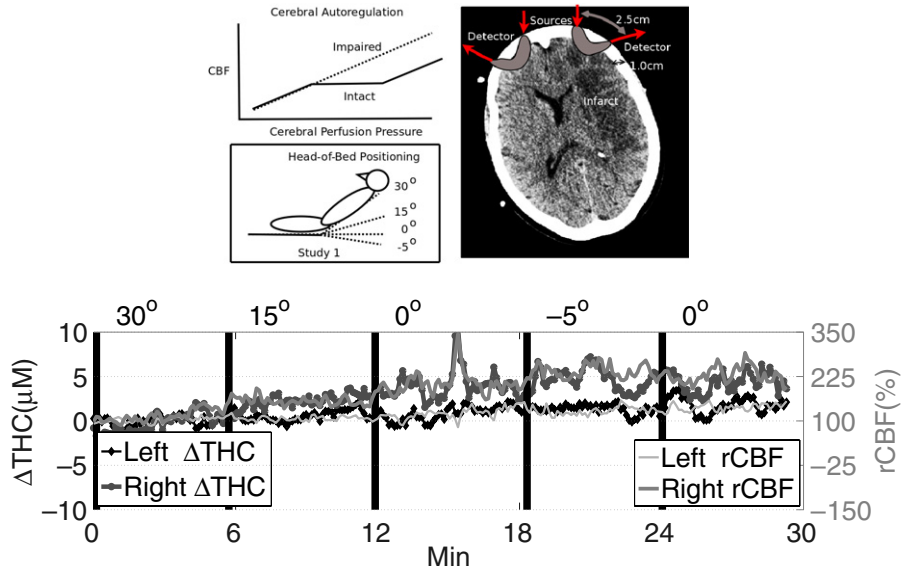


Figure 15. (Top) Cerebral autoregulation implies a range of cerebral perfusion pressure (CPP) values where CBF is kept constant. As shown in the inset, impairment causes CBF to depend passively on CPP. Head-of-bed positioning was used to induce orthostatic changes in CPP. Schematic showing placement of probes where one is placed on the infarcted hemisphere and the other on contralateral, ‘healthy’ hemisphere. (Bottom) Changes in Δ THC and r CBF are significantly larger on the infarcted hemisphere (right) which is presumably due to impaired cerebral autoregulation. (Reprinted with permission from [80]. Copyright 2009 Optical Society of America.)

mean age 65 years) with probes placed on the forehead near the frontal poles (figure 15 (top, right)). CBF and hemoglobin concentrations were measured sequentially for 5 min each at HOB positions: 30°, 15°, 0°, -5° and 0° and normalized to their values at 30°. Figure 15(bottom) shows continuous CBF data taken over 25 min from a representative subject with acute ischemic stroke. A clear differentiation is observed between two hemispheres; this differentiation was statistically significant over the whole population. In contrast, when an age-matched group with ‘vascular risk factors’ was studied, i.e., risk factors such as cigarette smoking, high blood pressure, etc, we did not observe any hemispherical differentiation. Interestingly, in \sim 25% of subjects, we have observed that CBF was not maximized at -5°; rather it was minimized at this HOB angle. This paradoxical response was also observed in traumatic brain injury patients [476]. The effect was likely a result of a substantial increase in intracranial pressure, a parameter that is not routinely monitored in ischemic stroke patients.

This example illustrates how diffuse optical instrumentation can be deployed at the bedside of critically ill-patients, and how it may be promising for use as a tool to optimize patient care based on cerebral hemodynamic measurements in real time.

4.2.4. Full head, 3D tomography in neonates. Amongst numerous applications of NIRS/DOS to neonatal studies, few groups have reported three-dimensional, tomographic imaging of the whole head [457, 477–481]. As discussed in previous sections, 3D tomography with NIRS/DOS has mostly been limited to less absorbing tissues such as the breast. New results, while still very preliminary, demonstrate the feasibility of whole-head imaging in neonates by taking advantage of their smaller head circumferences and thinner skulls. When

combined with other modalities such as ultrasound, MRI or CT, this approach could provide valuable physiologic information in addition to the mostly morphological information available via other modalities. Figure 16 (from [477]) shows a photo of the probe on a subject and coronal sections of images of blood volume and blood oxygen saturation as it compares with an ultrasound image from a 34-week gestational age infant. In general, 3D scans such as this one show a left/right symmetry between hemispheres, except in the presence of a condition such as a hemorrhage. The images shown are from an infant who was diagnosed with a left-sided intraventricular hemorrhage which is also visible on the ultrasound image. A clear increase in blood volume is evident on the left hemisphere, consistent with the presence of the hemorrhage. In the blood oxygen saturation image, a small region of significantly low oxygen saturation (10% versus 62% on the contralateral side) that is apparent; it is more lateral and superficial than both the ultrasound and blood volume images. This observation may be attributed to the presence of an ischemic penumbra surrounding hemorrhagic lesions, or it may be due to issues with optical image reconstruction. Nevertheless, the authors reported data from \sim 40 infants showing the feasibility of 3D tomography in neonates. This type of approach may become more common in the future with improved probe designs, detectors and newer reconstruction algorithms.

5. Other applications

Due to space constraints, we have chosen to focus on breast and brain applications. Other applications include, but are not limited to, imaging and monitoring in pre-clinical and clinical oncology [482], monitoring of muscle diseases and physiology [432, 483], photo-dynamic therapy planning

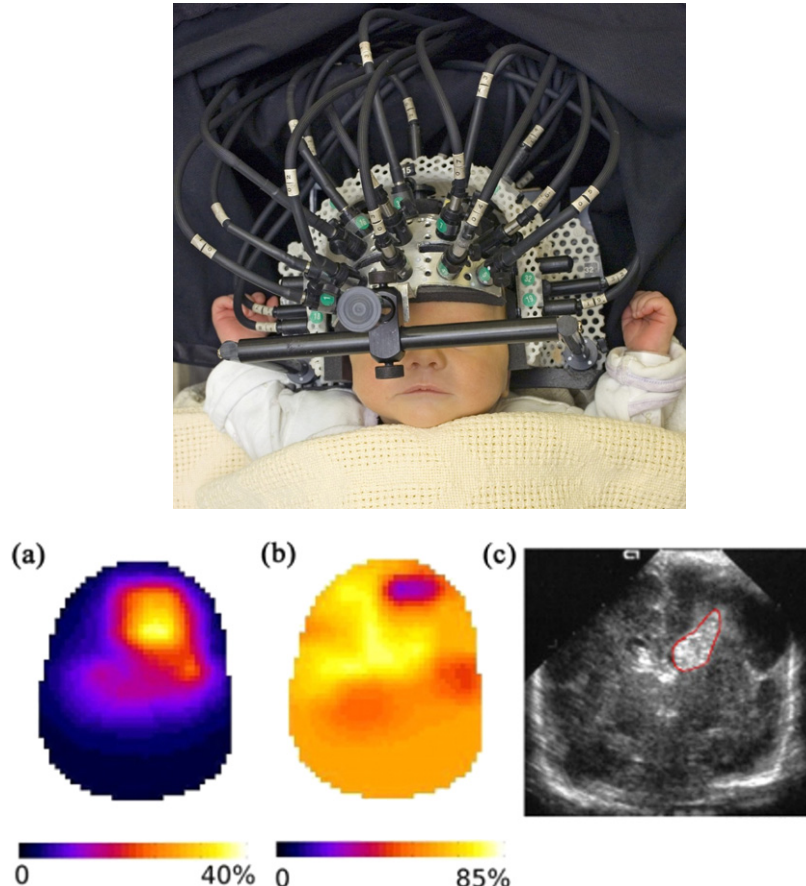


Figure 16. (Left) Placement of probes on an infant. (Right) Coronal sections showing (a) blood volume, (b) blood oxygen saturation and (c) the corresponding ultrasound image. (Reprinted with permission from [477]. Copyright 2007 Springer Science and Business Media.)

[484, 485], in-surgery monitoring [455] and guidance [272, 486], dermatology [487] and tomography of finger joint physiology and disease [488, 489]. The biomedical optics field has, more broadly, also been branching into many other clinically exciting directions with tools ranging from optical coherence tomography to photo-acoustic tomography and microscopy to optical projection tomography. Interested readers will find more information about these subjects in [490–494].

6. Conclusion

In this review, we have outlined the physical and algorithmic foundations of near-infrared (NIRS) or diffuse optical (DOS) spectroscopy, diffuse correlation spectroscopy (DCS) and diffuse optical tomography (DOT). We have showcased their applications in two subfields: optical mammography and cerebral hemodynamics. These subfields were chosen because they are, arguably, the two areas with the largest amount of diffuse optics research activity. The field has now evolved to a point wherein substantial effort is oriented toward clinical application. In the near future, improved understanding of photon propagation in tissues, better access to algorithms and computational resources, new developments in laser and detector technologies, and increasing amounts of clinical data will enable these developments.

Acknowledgments

This work was partially funded by NIH-grants HL-57835, NS-60653, RR-02305, EB-07610, NS-45839, CA-126187, Thrasher Research Fund (NR 0016) and Fundació Cellex Barcelona. The authors gratefully acknowledge many fruitful discussions and interactions over the years with colleagues from the biomedical optics community at the University of Pennsylvania and, indeed, throughout the world. At UPenn, much of the research in this review was facilitated by sustained collaborations over many years with Britton Chance, Mitchell Schnall, Joel Greenberg, John Detre, Daniel Licht, Theresa Busch, Mark Rosen, Thomas Floyd, Joseph Culver, Guoqiang Yu and David Boas.

References

- [1] Cutler M 1929 Transillumination of the breast *Surg. Gynecol. Obstet.* **48** 721–7
- [2] Jobsis F F 1977 Noninvasive infrared monitoring of cerebral and myocardial sufficiency and circulatory parameters *Science* **198** 1264–7
- [3] Jöbsis-vanderVliet F F and Jöbsis P D 1999 Biochemical and physiological basis of medical near-infrared spectroscopy *J. Biomed. Opt.* **4** 397
- [4] Jöbsis-vanderVliet F F 1999 Discovery of the near-infrared window into the body and the early development of near-infrared spectroscopy *J. Biomed. Opt.* **4** 392

- [5] Yodh A and Chance B 1995 Spectroscopy and imaging with diffusing light *Phys. Today* **48** 34–40
- [6] Chance B and Alfano R (ed) 1995 *Proc. Optical Tomography, Photon Migration, and Spectroscopy of Tissue and Model Media: Theory, Human Studies, and Instrumentation, Proc. SPIE* **2389**
- [7] Patterson M S, Moulton J D, Wilson B C, Berndt K W and J R Lakowicz 1991 Frequency-domain reflectance for the determination of the scattering and absorption properties of tissue *Appl. Opt.* **30** 4474–6
- [8] Patterson M S, Chance B and Wilson B C 1989 Time resolved reflectance and transmittance for the non-invasive measurement of tissue optical properties *Appl. Opt.* **28** 2331–6
- [9] Gratton E, Mantulin W W, van de Ven M J, Fishkin J, Maris M, and Chance B 1990 The possibility of a near-infrared imaging system using frequency-domain methods *Proc. Third Int. Conf. on Peace Through Mind/Brain Science (Hamamatsu, Japan)* pp 183–9
- [10] Delpy D T, Cope M, van der Zee P, Arridge S, Wray S and Wyatt J 1988 Estimation of optical pathlength through tissue from direct time of flight measurement *Phys. Med. Biol.* **33** 1433–42
- [11] Jacques S L 1989 Time resolved propagation of ultrashort laser pulses within turbid tissues *Appl. Opt.* **28** 2223–9
- [12] Benaron D A and Stevenson D K 1993 Optical time-of-flight and absorbance imaging of biologic media *Science* **259** 1463–6
- [13] O’Leary M A, Boas D A, Chance B and Yodh A G 1992 Refraction of diffuse photon density waves *Phys. Rev. Lett.* **69** 2658–61
- [14] Boas D A, O’Leary M A, Chance B and Yodh A G 1993 Scattering and wavelength transduction of diffuse photon density waves *Phys. Rev. E* **47** R2999–R3002
- [15] Fishkin J B and Gratton E 1993 Propagation of photon density waves in strongly scattering media containing an absorbing ‘semi-infinite’ plane bounded by a straight edge *J. Opt. Soc. Am. A* **10** 127–40
- [16] Schmitt J M, Knutel A, and Knutson J R 1992 Interference of diffusive light waves *J. Opt. Soc. Am. A* **9** 1832
- [17] Tromberg B J, Svaasand L O, Tsay T and Haskell R C 1993 Properties of photon density waves in multiple-scattering media *Appl. Opt.* **32** 607–16
- [18] Sevick E M, Lakowicz J R, Szmucinski H, Nowaczyk K and Johnson M L 1992 Frequency domain imaging of absorbers obscured by scattering *J. Photochem. Photobiol. B: Biol.* **16** 169–85
- [19] Johnson C C 1970 Optical diffusion in blood *IEEE Trans. Biomed. Eng.* **BME17** 129–33
- [20] Ishimaru A 1978 *Wave Propagation and Scattering in Random Media* (San Diego, CA: Academic)
- [21] Furutsu K 1980 On the diffusion equation derived from the space-time transport equation *J. Opt. Soc. Am. A* **70** 360
- [22] Groenhuis R A J, Ferwerda H A and Bosch T J J 1983 Scattering and absorption of turbid materials determined from reflection measurements: I. Theory *Appl. Opt.* **22** 2456–62
- [23] Yodh A G and Boas D A 2003 Functional imaging with diffusing light *Biomedical Photonics* (Boca Raton, FL: CRC Press) pp 21/1–45
- [24] Ntziachristos V and Chance B 2001 Probing physiology and molecular function using optical imaging: applications to breast cancer *Breast Cancer Res.* **3** 41–6
- [25] Hawrysz D J and Sevick-Muraca E M 2000 Developments toward diagnostic breast cancer imaging using near-infrared optical measurements and fluorescent contrast agents *Neoplasia* **2** 388–417
- [26] Corlu A, Choe R, Durduran T, Rosen M A, Schweiger M, Arridge S R, Schnall M D and Yodh A G 2007 Three-dimensional *in vivo* fluorescence diffuse optical tomography of breast cancer in humans *Opt. Express* **15** 6696–716
- [27] Ferrari M, Hanley D F, Wilson D A and Traystman R J 1990 Redox changes in cat brain cytochrome-c oxidase after blood-fluorocarbon exchange *Am. J. Physiol.—Heart Circulatory Physiol.* **258** 1706–13
- [28] Gratton G, Corballis P M, Cho E, Fabiani M and Hood D C 1995 Shades of gray matter: noninvasive optical images of human brain responses during visual stimulation *Psychophysiology* **32** 505–9
- [29] Gratton G, Fabiani M, Friedman D, Franceschini M A, Fantini S, Corballis P M and Gratton E 1995 Rapid changes of optical parameters in the human brain during a tapping task *J. Cogn. Neurosci.* **7** 446–56
- [30] Arridge S R and Schotland J C 2009 Optical tomography: forward and inverse problems *Inverse Problems* **25** 123010
- [31] Boas D A, Brooks D H, Miller E L, DiMarzio C A, Kilmer M, Gaudette R J and Zhang Q 2001 Imaging the body with diffuse optical tomography *IEEE Signal Process. Mag.* **18** 57–75
- [32] Hebden J C, Arridge S R, and Delpy D T 1997 Optical imaging in medicine: I. Experimental techniques *Phys. Med. Biol.* **42** 825–40
- [33] Hebden J C and Delpy D T 1997 Diagnostic imaging with light *Br. J. Radiol.* **70** Spec No: S206–14
- [34] Arridge S R and Hebden J C 1997 Optical imaging in medicine: II. Modelling and reconstruction *Phys. Med. Biol.* **42** 841–54
- [35] Villringer A and Chance B 1997 Non-invasive optical spectroscopy and imaging of human brain function *Trends Neurosci.* **20** 435–42
- [36] Clark N A, Lunacek J H and Benedek G B 1970 A study of brownian motion using light scattering *Am. J. Phys.* **38** 575–85
- [37] Fuller G G, Rallison J M, Schmidt R L and Leal L G 1980 The measurement of velocity gradients in laminar flow by homodyne light-scattering spectroscopy *J. Fluid Mech.* **100** 555–75
- [38] Tong P, Goldburg W I, Chan C K and Sirivat A 1988 Turbulent transition by photon-correlation spectroscopy *Phys. Rev. A* **37** 2125–33
- [39] Bertolotti M, Crosignani B, Di Porto P and Sette D 1969 Light scattering by particles suspended in a turbulent fluid *J. Phys. A: Math. Gen.* **2** 126–8
- [40] Bourke P J, Butterworth J, Drain L E, Egelstaff P A, Jakeman E and Pike E R 1970 A study of the spatial structure of turbulent flow by intensity-fluctuation spectroscopy *J. Phys. A: Math. Gen.* **3** 216–28
- [41] Tanaka T, Riva C and Ben-Sira I 1974 Blood velocity measurements in human retinal vessels *Science* **186** 830–1
- [42] Stern M D 1975 *In vivo* evaluation of microcirculation by coherent light scattering *Nature* **254** 56–8
- [43] Bonner R F and Nossal R 1990 Principles of laser-Doppler flowmetry *Laser-Doppler Blood Flowmetry* vol 107 (Boston, MA: Kluwer) pp 17–45
- [44] Pusey P N and Vaughan J M 1975 Light scattering and intensity fluctuation spectroscopy *Dielectric and Related Molecular Processes* vol 2 ed M Davies *Specialist Periodical Report* (London: The Chemical Society)
- [45] Berne B J and Pecora R 1990 *Dynamic Light Scattering with Applications to Chemistry, Biology and Physics* (Malabar, FL: Krieger)
- [46] Brown W 1993 *Dynamic Light Scattering: The Method and Some Applications* (New York: Clarendon)
- [47] Cummings H Z and Pike E R 1974 *Photon Correlation and Light-Beating Spectroscopy (NATO Advanced Study Institute Series B: Physics* vol 3) (New York: Plenum)

- [48] Cummings H Z and Swinney H L 1970 Light beating spectroscopy *Prog. Opt.* **8** 133–200
- [49] Valkov A Y and Romanov V P 1986 Characteristics of propagation and scattering of light in nematic liquid crystals *Sov. Phys.—JETP* **63** 737–43
- [50] Briers J D 2001 Laser doppler, speckle and related techniques for blood perfusion mapping and imaging *Physiol. Meas.* **22** R35–66
- [51] Riva C E, Ross B and Benedek G B 1972 Laser doppler measurements of blood flow in capillary tubes and retinal arteries *Invest. Ophthalmol.* **11** 936–44
- [52] Tanaka T and Benedek G B 1975 Measurement of the velocity of blood flow (*in vivo*) using a fiber optic catheter and optical mixing spectroscopy. *Appl. Opt.* **14** 189–96
- [53] Stern M D, Bowen P D, Parma R, Osgood R W, Bowman R L and Stein J H 1979 Measurements of renal cortical and medullary blood flow by laser-doppler spectroscopy in the rat *Am. J. Physiol.* **236** F80–7
- [54] Stern M D, Lappé D L, Bowen P D and Chimosky J E 1977 Continuous measurements of tissue blood flow by laser-doppler spectroscopy *Am. J. Physiol.* **232** H441–8
- [55] Oberg P A, Nilsson G E, Tenland T, Holmstrom A and Lewis D H 1979 Use of a new laser doppler flowmeter for measurements of capillary blood flow in skeletal muscle after bullet wounding *Acta Chir. Scand. Suppl.* **489** 145–50
- [56] Kiel J W, Riedel G L, DiResta G R and Shepherd A P 1985 Gastric mucosal blood flow measured by laser-doppler velocimetry *Am. J. Physiol.* **249** G539–545
- [57] Hellerm S, Jacobsson L S, Nilsson G E and Lewis D H 1983 Measurements of microvascular blood flow in cancellous bone using laser doppler flowmetry and ^{133}Xe -clearance *Int. J. Oral Surg.* **12** 165–77
- [58] Williams P C, Stern M D, Bowen P D, Brooks R A, Hammock M K, Bowman R L and Chiro G 1980 Mapping of cerebral cortical strokes in rhesus monkeys by laser doppler spectroscopy *Med. Res. Eng.* **13** 3–5
- [59] Shepherd A P and Riedel G L 1982 Continuous measurements of intestinal mucosal blood flow by laser-doppler velocimetry *Am. J. Physiol.* **242** G668–72
- [60] Boas D A, Campbell L E and Yodh A G 1995 Scattering and imaging with diffusing temporal field correlations *Phys. Rev. Lett.* **75** 1855–8
- [61] Boas D A and Yodh A G 1997 Spatially varying dynamical properties of turbid media probed with diffusing temporal light correlation *J. Opt. Soc. Am. A* **14** 192–215
- [62] Pine D J, Weitz D A, Chaikin P M and Herbolzheimer E 1988 Diffusing-wave spectroscopy *Phys. Rev. Lett.* **60** 1134–7
- [63] Maret G and Wolf P E 1987 Multiple light scattering from disordered media. The effect of brownian motion of scatterers *Z. Phys. B* **65** 409–13
- [64] Stephen M J 1988 Temporal fluctuations in wave propagation in random media *Phys. Rev. B* **37** 1–5
- [65] Durduran T 2004 Non-invasive measurements of tissue hemodynamics with hybrid diffuse optical methods *PhD Dissertation* University of Pennsylvania
- [66] Durduran T, Yu G, Burnett M G, Detre J A, Greenberg J H, Wang J, Zhou C and Yodh A G 2004 Diffuse optical measurements of blood flow, blood oxygenation and metabolism in human brain during sensorimotor cortex activation *Opt. Lett.* **29** 1766–8
- [67] Li J, Dietsche G, Iftime D, Skipetrov S E, Maret G, Elbert T, B Rockstroh and Gisler T 2005 Noninvasive detection of functional brain activity with near-infrared diffusing-wave spectroscopy *J. Biomed. Opt.* **10** 044002–1–044002–12
- [68] Yu G, Durduran T, Zhou C, Wang H W, Putt M E, Saunders M, Seghal C M, Glatstein E, Yodh A G and Busch T M 2005 Noninvasive monitoring of murine tumor blood flow during and after photodynamic therapy provides early assessment of therapeutic efficacy *Clin. Cancer Res.* **11** 3543–52
- [69] Buckley E M *et al* 2009 Cerebral hemodynamics in preterm infants during positional intervention measured with diffuse correlation spectroscopy and transcranial doppler ultrasound *Opt. Express* **17** 12571–81
- [70] Menon C, Polin G M, Prabakaran I, Hs A, Cheung C, Culver J P, Pingpank J, Sehgal C S, Yodh A G, Buerk D G and Fraker D L 2003 An integrated approach to measuring tumor oxygen status using human melanoma xenografts as a model *Cancer Res.* **63** 7232–40
- [71] Roche-Labarbe N, Carp S A, Surova A, Patel M, Boas D A, Grant P E and Franceschini M A 2009 Noninvasive optical measures of CBV, StO_2 , CBF index and $r\text{CMRO}_2$ in human premature neonates' brains in the first six weeks of life (p na). *Human Brain Mapping* **31** 341–52
- [72] Durduran T *et al* 2010 Optical measurement of cerebral hemodynamics and oxygen metabolism in neonates with congenital heart defects *J. Biomed. Opt.* at press
- [73] Yu G, Floyd T, Durduran T, Zhou C, Wang J J, Detre J A and Yodh A G 2007 Validation of diffuse correlation spectroscopy for muscle blood flow with concurrent arterial-spin-labeling perfusion *Opt. Exp.* **15** 1064–75
- [74] Kim M N *et al* 2010 Noninvasive measurement of cerebral blood flow and blood oxygenation using near-infrared and diffuse correlation spectroscopies in critically brain-injured adults *Neurocritical Care* **12** 173–80
- [75] Zhou C, Eucker S, Durduran T, Yu G, Ralston J, Friess S H, Ichord R N, Margulies S S and Yodh A G 2009 Diffuse optical monitoring of hemodynamic changes in piglet brain with closed head injury *J. Biomedical Opt.* **14** 034015
- [76] Culver J P, Durduran T, Furuya D, Cheung C, Greenberg J H and Yodh A G 2003 Diffuse optical tomography of cerebral blood flow, oxygenation and metabolism in rat during focal ischemia *J. Cereb. Blood Flow Metab.* **23** 911–24
- [77] Cheung C, Culver J P, Takahashi K, Greenberg J H and Yodh A G 2001 *In vivo* cerebrovascular measurement combining diffuse near-infrared absorption and correlation spectroscopies *Phys. Med. Biol.* **46** 2053–65
- [78] Zhou C, Yu G, Furuya D, Greenberg J H, Yodh A G and Durduran T 2006 Diffuse optical correlation tomography of cerebral blood flow during cortical spreading depression in rat brain *Opt. Exp.* **14** 1125–44
- [79] Durduran T, Zhou C, Yu G, Edlow B, Choe R, Shah Q, Kasner S E, Cucchiara B L, Yodh A G, Greenberg J H and Detre J A 2007 Bed-side monitoring of cerebral blood flow (CBF) in acute stroke patients during changes in head of bed position *Int. Stroke Conf.* vol P37 (San Francisco, CA: American Heart Association)
- [80] Durduran T *et al* 2009 Transcranial optical monitoring of cerebrovascular hemodynamics in acute stroke patients *Opt. Exp.* **17** 3884–902
- [81] Yu G, Durduran T, Lech G, Zhou C, Chance B, Mohler E R and Yodh A G 2005 Time-dependent blood flow and oxygenation in human skeletal muscle measured with noninvasive near-infrared diffuse optical spectroscopies *J. Biomed. Opt.* **10** 024027–1–12
- [82] Yu G, Durduran T, Zhou C, Zhu T C, Finlay J C, Busch T M, Malkowicz S B, Hahn S M and Yodh A G 2006 Real-time in situ monitoring of human prostate photodynamic therapy with diffuse light *Photochem. Photobiol.* **82** 1279–84
- [83] Sunar U *et al* 2006 Non-invasive diffuse optical measurement of blood flow and blood oxygenation for monitoring radiation therapy in patients with head and neck tumors: a pilot study *J. Biomed. Opt.* **11** 064021
- [84] Zhou C *et al* 2007 Diffuse optical monitoring of blood flow and oxygenation in human breast cancer during early

- stages of neoadjuvant chemotherapy *J. Biomed. Opt.* **12** 051903
- [85] Sunar U, Makonnen S, Zhou C, Durduran T, Guoqiang Yu, Wang H W, Lee W M and Yodh A G 2007 Hemodynamic responses to antivascular therapy and ionizing radiation assessed by diffuse optical spectroscopies *Opt. Express* **15** 15507–16
- [86] Durduran T, Choe R, Yu G, Zhou C, Tchou J C, Czerniecki B J and Yodh A G 2005 Diffuse optical measurement of blood flow in breast tumors *Opt. Lett.* **30** 2915–17
- [87] Li J, Ninck M, Koban L, Elbert T, Kissler J and Gisler T 2008 Transient functional blood flow change in the human brain measured noninvasively by diffusing-wave spectroscopy *Opt. Lett.* **33** 2233–5
- [88] Dietsche G, Ninck M, Ortolf C, Li J, Jaillon F and Gisler T 2007 Fiber-based multispeckle detection for time-resolved diffusing-wave spectroscopy: characterization and application to blood flow detection in deep tissue *Appl. Opt.* **46** 8506–14
- [89] Jaillon F, Li J, Dietsche G, Elbert T and Gisler T 2007 Activity of the human visual cortex measured non-invasively by diffusing-wave spectroscopy *Opt. Express* **15** 6643–50
- [90] Jaillon F, Skipetrov S E, Li J, Dietsche G, Maret G and Gisler T 2006 Diffusing-wave spectroscopy from head-like tissue phantoms: influence of a non-scattering layer *Opt. Express* **14** 10181–94
- [91] Case K M and Zweifel P F 1967 *Linear Transport Theory* (Boston, MA: Addison-Wesley)
- [92] Davidson B 1957 *Neutron Transport Theory* (Oxford: Clarendon)
- [93] Glasstone S and Edlund M C 1952 *The Elements of Nuclear Reactor Theory* (New York: Van Nostrand)
- [94] Chandrasekhar S 1960 *Radiative Transfer* (New York: Dover)
- [95] Cheong W F, Prahl S A and Welch A J 1990 A review of the optical properties of biological tissues *IEEE J. Quantum Electron.* **QE-26** 2166–85
- [96] Ripoll J 2000 Light Diffusion in Turbid Media With Biomedical Applications *PhD Dissertation* Universidad Autónoma de Madrid
- [97] Farrell T J, Patterson M S and Wilson B 1992 A diffusion theory model of spatially resolved, steady-state diffuse reflectance for the noninvasive determination of tissue optical properties *in vivo* *Med. Phys.* **19** 879–88
- [98] Jacques S L and Pogue B W 2008 Tutorial on diffuse light transport *J. Biomed. Opt.* **13** 041302
- [99] Heino J, Arridge S, Sikora J and Somersalo E 2003 Anisotropic effects in highly scattering media *Phys. Rev. E* **68** 031908
- [100] Custo A, Wells W M III, Barnett A H, Hillman E M C and Boas D A 2006 Effective scattering coefficient of the cerebral spinal fluid in adult head models for diffuse optical imaging *Appl. Opt.* **45** 4747–55
- [101] Okada E and Delpy D T 2003 Near-infrared light propagation in an adult head model: I. Modeling of low-level scattering in the cerebrospinal fluid layer *Appl. Opt.* **42** 2906–14
- [102] Kaplan P D, Kao M H, Yodh A G and Pine D J 1993 Geometric constraints for the design of diffusing-wave spectroscopy experiments *Appl. Opt.* **32** 3828–36
- [103] Siegel A M, Marota J A and Boas D A 1999 Design and evaluation of a continuous-wave diffuse optical tomography system *Opt. Express* **4** 287–98
- [104] Nioka S, Luo Q and Chance B 1997 Human brain functional imaging with reflectance *CWS Adv. Exp. Med. Biol.* **428** 237–42
- [105] Colier W, van der Sluijs M C Menssen J and Oeseburg B 2000 A new and highly sensitive optical brain imager with 50 Hz sample rate *NeuroImage* **11** 542
- [106] Culver J P, Choe R, Holboke M J, Zubkov L, Durduran T, Slemp A, Ntziachristos V, Pattanayak D N, Chance B and Yodh A G 2003 Three-dimensional diffuse optical tomography in the plane parallel transmission geometry: evaluation of a hybrid frequency domain/continuous wave clinical system for breast imaging *Med. Phys.* **30** 235–47
- [107] Chance B, Cope M, Gratton E, Ramanujam N and Tromberg B 1998 Phase measurement of light absorption and scattering in human tissues *Rev. Sci. Instrum.* **69** 3457–81
- [108] Pogue B W and Patterson M S 1994 Frequency-domain optical-absorption spectroscopy of finite tissue volumes using diffusion-theory *Phys. Med. Biol.* **39** 1157–80
- [109] Andersson-Engels S, Berg R, Svanberg S and Jarlman O 1990 Time-resolved transillumination for medical diagnostics *Opt. Lett.* **15** 1179–81
- [110] Jacques S L 1989 Time-resolved reflectance spectroscopy in turbid tissues *IEEE Trans. Biomed. Eng.* **36** 1155–61
- [111] Schmidt F E W, Fry M E, Hillman E M C, Hebden J C and Delpy D T 2000 A 32-channel time-resolved instrument for medical optical tomography *Rev. Sci. Instrum.* **71** 256–65
- [112] Ntziachristos V, Ma X H and Chance B 1998 Time-correlated single photon counting imager for simultaneous magnetic resonance and near-infrared mammography *Rev. Sci. Instrum.* **69** 4221–33
- [113] Selb J, Stott J J, Franceschini M A, Sorensen A G and Boas D A 2005 Improved sensitivity to cerebral hemodynamics during brain activation with a time-gated optical system: analytical model and experimental validation *J. Biomed. Opt.* **10** 011013
- [114] Liebert A, Wabnitz H, Steinbrink J, Obrig H, Moller M, Macdonald R, Villringer A and Rinneberg H 2004 Time-resolved multidistance near-infrared spectroscopy of the adult head: intracerebral and extracerebral absorption changes from moments of distribution of times of flight of photons *Appl. Opt.* **43** 3037–47
- [115] Haskell R C, Svaasand L O, Tsay T, Feng T, McAdams M S and Tromberg B J 1994 Boundary conditions for the diffusion equation in radiative transfer *J. Opt. Soc. Am. A* **11** 2727–41
- [116] Aronson R 1995 Boundary conditions for diffusion of light *J. Opt. Soc. Am. A* **12** 2532–9
- [117] Dehghani H, Eames M E, Yalavarthy P K, Davis S C, Srinivasan S, Carpenter C M, Pogue B W and Paulsen K D 2008 Near infrared optical tomography using nirfast: algorithm for numerical model and image reconstruction *Commun. Numer. Methods Eng.* **25** 711–32
- [118] Arfken G 1970 *Mathematical Methods for Physicists* 2nd edn (New York: Academic)
- [119] Barton G 1989 *Elements of Green's Functions and Propagation: Potentials, Diffusion and Waves* (Oxford: Oxford University Press)
- [120] Arridge S R, Cope M and Delpy D T 1992 The theoretical basis for the determination of optical pathlengths in tissue: temporal and frequency analysis *Phys. Med. Biol.* **37** 1531–60
- [121] Carslaw H S and Jaeger J 1986 *Conduction of Heat in Solids* (New York: Oxford University Press)
- [122] Choe R *et al* 2009 Differentiation of benign and malignant breast tumors by *in-vivo* three-dimensional parallel-plate diffuse optical tomography *J. Biomed. Opt.* **14** 024020
- [123] Boas D A, O'Leary M A, Chance B and Yodh A G 1994 Scattering of diffuse photon density waves by spherical inhomogeneities within turbid media—analytic solution and applications *Proc. Natl Acad. Sci. USA* **91** 4887–91
- [124] Walker S A, Boas D A and Gratton E 1998 Photon density waves scattered from cylindrical inhomogeneities: theory and experiments *Appl. Opt.* **37** 1935–44

- [125] Ripoll J, Ntziachristos V, Culver J P, Pattanayak D N, Yodh A G and Nieto-Vesperinas M 2001 Recovery of optical parameters in multiple-layered diffusive media: theory and experiments *J. Opt. Soc. A* **18** 821–30
- [126] Farrell T J, Patterson M S and Essenpreis M 1998 Influence of layered tissue architecture on estimates of tissue optical properties obtained from spatially resolved diffuse reflectometry *Appl. Opt.* **37** 1958–72
- [127] Hielscher A H, Liu H L, Chance B, Tittel F K and Jacques S L 1996 Time-resolved photon emission from layered turbid media *Appl. Opt.* **35** 719–28
- [128] Alexandrakis G, Busch D R, Faris G W and Patterson M S 2001 Determination of the optical properties of two-layer turbid media by use of a frequency-domain hybrid monte carlo diffusion model *Appl. Opt.* **40** 3810–21
- [129] Alexandrakis G, Farrell T J and Patterson M S 1998 Accuracy of the diffusion approximation in determining the optical properties of a two-layer turbid medium *Appl. Opt.* **37** 7401–9
- [130] Schweiger M, Nissilä I, Boas D A and Arridge S R 2007 Image reconstruction in optical tomography in the presence of coupling errors *Appl. Opt.* **46** 2743–56
- [131] Hueber D M, Franceschini M A, Ma H Y, Zhang Q, Ballesteros J R, Fantini S, Wallace D, Ntziachristos V and Chance B 2001 Non-invasive and quantitative near-infrared haemoglobin spectrometry in the piglet brain during hypoxic stress, using a frequency-domain multidistance instrument *Phys. Med. Biol.* **46** 41–62
- [132] Nissilä I, Noponen T, Kotilahti K, Katila T, Lipiäinen L, Tarvainen T, Schweiger S and Arridge S 2005 Instrumentation and calibration methods for the multichannel measurement of phase and amplitude in optical tomography *Rev. Sci. Instrum.* **76** 044302
- [133] Yamashita Y, Maki A and Koizumi H 2001 Wavelength dependence of the precision of noninvasive optical measurement of oxy-, deoxy- and total-hemoglobin concentration *Med. Phys.* **28** 1108–14
- [134] Strangman G, Franceschini M A and Boas D A 2003 Factors affecting the accuracy of near-infrared spectroscopy concentration calculations for focal changes in oxygenation parameters *NeuroImage* **18** 865–79
- [135] Boas D A, Dale A M and Franceschini M A 2004 Diffuse optical imaging of brain activation: approaches to optimizing image sensitivity, resolution and accuracy *NeuroImage* **23** 275–88
- [136] Corlu A, Durduran T, Choe R, Schweiger M, Hillman E M C, Arridge S R and Yodh A G 2003 Uniqueness and wavelength optimization in continuous-wave multispectral diffuse optical tomography *Opt. Lett.* **28** 2339–41
- [137] Corlu A, Choe R, Durduran T, Lee K, Schweiger M, Hillman E M C, Arridge S R and Yodh A G 2005 Diffuse optical tomography with spectral constraints and wavelength optimization *Appl. Opt.* **44** 2082–93
- [138] Arridge S R and Lionheart W R B 1998 Nonuniqueness in diffusion-based optical tomography *Opt. Lett.* **23** 882–4
- [139] Srinivasan S, Pogue B W, Jiang S, Dehghani H and Paulsen K D 2005 Spectrally constrained chromophore and scattering near-infrared tomography provides quantitative and robust reconstruction *Appl. Opt.* **44** 1858–69
- [140] Brendel B and Nielsen T 2009 Selection of optimal wavelengths for spectral reconstruction in diffuse optical tomography *J. Biomed. Opt.* **14** 034041
- [141] Eames M E, Wange J, Pogue B W and Dehghani H 2008 Wavelength band optimization in spectral near-infrared optical tomography improves accuracy while reducing data acquisition and computational burden *J. Biomed. Opt.* **13** 054037
- [142] van der Zee P *et al* 1992 Experimentally measured optical pathlengths for the adult's head, calf and forearm and the head of the newborn infant as a function of interoptode spacing *Adv. Exp. Med. Biol.* **316** 143–53
- [143] Duncan A, Meek J H, Clemence M, Elwell C E, Tyszcuk L, Cope M and Delpy D T 1995 Optical pathlength measurements on adult head, calf and forearm and the head of the newborn infant using phase resolved optical spectroscopy *Phys. Med. Biol.* **40** 295–304
- [144] Cope M and Delpy D T 1988 System for long-term measurement of cerebral blood flow and tissue oxygenation on newborn infants by infra-red transillumination *Med. Biol. Eng. Comput.* **26** 289–94
- [145] Boas D A, Gaudette T, Strangman G, Cheng X, Marota J J A and Mandeville J B 2001 The accuracy of near infrared spectroscopy and imaging during focal changes in cerebral hemodynamics *NeuroImage* **13** 76–90
- [146] Kohl M, Lindauer U, Royl G, Kuhl M, Gold L, Villringer A and Dirnagl U 2000 Physical model for the spectroscopic analysis of cortical intrinsic optical signals *Phys. Med. Biol.* **45** 3749–64
- [147] Franceschini M A, Toronov V, Filiaci M E, Gratton E and Fantini S 2000 On-line optical imaging of the human brain with 160 ms temporal resolution *Opt. Express* **6** 49–57
- [148] Tamura M, Hoshi Y and Okada F 1997 Localized near-infrared spectroscopy and functional optical imaging of brain activity *Phil. Trans. R. Soc. Lond. B: Biol. Sci.* **352** 737–42
- [149] Nollert G, Jonas R A and Reichart B 2000 Optimizing cerebral oxygenation during cardiac surgery: a review of experimental and clinical investigations with near infrared spectrophotometry *Thorac. Cardiovasc. Surg.* **48** 247–53
- [150] Fantini S, Hueber D, Franceschini M A, Gratton E, Rosenfeld W, Stubblefield P G, Maulik D and Stankovic M R 1999 Non-invasive optical monitoring of the newborn piglet brain using continuous-wave and frequency-domain spectroscopy *Phys. Med. Biol.* **44** 1543–63
- [151] Chu B 1991 *Laser Light Scattering, Basic Principles and Practice* (New York: Academic)
- [152] Lemieux P A and Durian D J 1999 Investigating non-gaussian scattering processes by using nth-order intensity correlation functions *J. Opt. Soc. Am. A* **16** 1651–64
- [153] Bonner R and Nossal R 1981 Model for laser doppler measurements of blood flow in tissue *Appl. Opt.* **20** 2097–107
- [154] Ackerson B J, Dougherty R L, Reguigui N M and Nobbman U 1992 Correlation transfer: application of radiative transfer solution methods to photon correlation problems *J. Thermophys. Heat Transfer* **6** 577–88
- [155] Dougherty R L, Ackerson B J, Reguigui N M, Dorri-Nowkoorani F and Nobmann U 1994 Correlation transfer: development and application *J. Quant. Spectrosc. Radiat Transfer* **52** 713–27
- [156] Weitz D A and Pine D J 1993 Diffusing-wave spectroscopy *Dynamic Light Scattering: The Method and Some Applications* ed W Brown (Oxford: Oxford Science Publications)
- [157] Xue J Z, Pine D J, Milner S T, Wu X L and Chaikin P M 1992 Nonergodicity and light scattering from polymer gels *Phys. Rev. A* **46** 6550–63
- [158] Schatzel K 1993 Accuracy of photon correlation measurements on nonergodic samples *Appl. Opt.* **32** 3880–5
- [159] Pusey P N and Van Megen W 1989 Dynamic light scattering by non-ergodic media *Physica A* **157** 705–42
- [160] Einstein A 1905 On the motion of small particles suspended in liquids at rest required by the molecular-kinetic theory of heat *Ann. Phys., Lpz.* **17** 549–60
- [161] Bishop J J, Popel A S, Intaglietta M and Johnson P C 2002 Effect of aggregation and shear rate on the dispersion of

- red blood cells flowing in venules *Am. J. Physiol. Heart Circ. Physiol.* **283** 1985–96
- [162] Boryczko K, Dzwinek W and Yuen D A 2003 Dynamical clustering of red blood cells in capillary vessels *J. Mol. Model. (Online)* **9** 16–33
- [163] Binzoni T, Leung T S, Seghier M L and Delpy D T 2004 Translational and brownian motion in laser-doppler flowmetry of large tissue volumes *Phys. Med. Biol.* **49** 5445–58
- [164] Abbot N C and Beck J S 1993 Biological zero in laser doppler measurements in normal ischemic and inflamed human skin *Int. J. Microcirc.—Clin. Exp.* **12** 89–98
- [165] Kernick D P, Tooke J E and Shore A C 1999 The biological zero signal in laser doppler fluximetry—origins and practical implications *Pflugers Arch.* **437** 624–31
- [166] Caspary L, Creutzig A and Alexander K 1988 Biological zero in laser doppler fluxmetry *Int. J. Microcirc. Clin. Exp.* **7** 367–71
- [167] Liebert A, Leahy M and Maniewski R 1995 A calibration standard for laser-doppler perfusion measurements *Rev. Sci. Instrum.* **66** 5169–73
- [168] Katayama K, Nishimura G, Kinjo M and Tamura M 1995 Absorbance measurements in turbid media by the photon correlation method *Appl. Opt.* **34** 7419–27
- [169] Arridge S R and Schweiger M 1993 Inverse methods for optical tomography *Information Processing in Medical Imaging (IPMI'93 Proceedings) (Lecture Notes in Computer Science vol 687)* (Berlin: Springer) pp 259–77
- [170] Arridge S R and Schweiger M 1997 Image reconstruction in optical tomography *Phil. Trans. R. Soc. Lond. Ser. B: Biol. Sci.* **352** 717–26
- [171] Arridge S R 1999 Optical tomography in medical imaging *Inverse Problems* **15** R41–R93
- [172] Walker S A, Fantini S and Gratton E 1997 Image reconstruction by backprojection from frequency-domain optical measurements in highly scattering media *Appl. Opt.* **36** 170–79
- [173] Colak S B, Papaioannou D G, 't Hooft G W, van der Mark M B Schomberg H, Paasschens J C J, Melissen J B M and van Asten N A A J 1997 Tomographic image reconstruction from optical projections in light-diffusing media *Appl. Opt.* **36** 180–213
- [174] Schotland J C 1997 Continuous-wave diffusion imaging *J. Opt. Soc. Am. A* **14** 275–79
- [175] Li X D, Durduran T, Chance B, Yodh A G and Pattanayak D N 1997 Diffraction tomography for biochemical imaging with diffuse-photon density waves *Opt. Lett.* **22** 573–5
- Li X D, Durduran T, Chance B, Yodh A G and Pattanayak D N 1997 Diffraction tomography for biochemical imaging with diffuse-photon density waves *Opt. Lett.* **22** 1198 (erratum)
- [176] Cheng X and Boas D A 1998 Diffuse optical reflectance tomography with continuous-wave illumination *Opt. Express* **3** 118–23
- [177] Matson C L and Liu H L 1999 Analysis of the forward problem with diffuse photon density waves in turbid media by use of a diffraction tomography model *J. Opt. Soc. Am. A* **16** 455–66
- [178] Schotland J C, Haselgrave J C and Leigh J S 1993 Photon hitting density *Appl. Opt.* **32** 448–53
- [179] O'Leary M A, Boas D A, Chance B and Yodh A G 1995 Experimental images of heterogeneous turbid media by frequency-domain diffusing-photon tomography *Opt. Lett.* **20** 426–8
- [180] Arridge S R 1995 Photon-measurement density functions: part 1 Analytical forms *Appl. Opt.* **34** 7395–409
- [181] Arridge S R and Schweiger M 1995 Photon-measurement density functions: part 2 Finite-element-method calculations *Appl. Opt.* **34** 8026–36
- [182] Yao Y, Wang Y, Pei Y, Zhu W and Barbour R L 1997 Frequency-domain optical imaging of absorption and scattering distributions using a born iterative method *J. Opt. Soc. Am. A* **14** 325–42
- [183] Paulsen K D and Jiang H 1995 Spatially varying optical property reconstruction using a finite element diffusion equation approximation *Med. Phys.* **22** 691–701
- [184] Jiang H, Paulsen K D and Osterberg U L 1996 Optical image reconstruction using DC data: simulations and experiments *Phys. Med. Biol.* **41** 1483–98
- [185] Paulsen K D and Jiang H 1996 Enhanced frequency-domain optical image reconstruction in tissues through total variation minimization *Appl. Opt.* **35** 3447–58
- [186] Jiang H, Paulsen K D, Oesterberg U L and Patterson M S 1997 Frequency-domain optical image reconstruction in turbid media: an experimental study of single-target detectability *Appl. Opt.* **36** 52–63
- [187] Jiang H, Paulsen K D, Oesterberg U L and Patterson M S 1998 Improved continuous light diffusion imaging in single- and multi-target tissue-like phantoms *Phys. Med. Biol.* **43** 675–93
- [188] Pogue B W, McBride T O, Prewitt J, Osterberg U L and Paulsen K D 1999 Spatially variant regularization improves diffuse optical tomography *Appl. Opt.* **38** 2950–61
- [189] Arridge S R and Schweiger M 1998 A gradient-based optimisation scheme for optical tomography *Opt. Express* **2** 213–26
- [190] Hielscher A H, Klose A D and Hanson K M 1999 Gradient-based iterative image reconstruction scheme for time-resolved optical tomography *IEEE Trans. Med. Imaging* **18** 262–71
- [191] Klibanov M V, Lucas T R and Frank R M 1997 A fast and accurate imaging algorithm in optical/diffusion tomography *Inverse Problems* **13** 1341–61
- [192] Gryazin Y A, Klibanov M V and Lucas T R 1999 Imaging the diffusion coefficient in a parabolic inverse problem in optical tomography *Inverse Problems* **1** 373–97
- [193] Roy R and Sevick-Muraca E M 1999 Truncated newton's optimization scheme for absorption and fluorescence optical tomography: I. Theory and formulation *Opt. Express* **4** 353–71
- [194] Roy R and Sevick-Muraca E M 1999 Truncated newton's optimization scheme for absorption and fluorescence optical tomography: II. Reconstruction from synthetic measurements *Opt. Express* **4** 372–82
- [195] Roy R and Sevick-Muraca E M 2000 Active constrained truncated newton method for simple-bound optical tomography *J. Opt. Soc. Am. A* **17** 1627–41
- [196] Roy R and Sevick-Muraca E M 2001 Three-dimensional unconstrained and constrained image-reconstruction techniques applied to fluorescence, frequency-domain photon migration *Appl. Opt.* **40** 2206–15
- [197] Oh S, Milstein A B, Bouman C A and Webb K J 2005 A general framework for nonlinear multigrid inversion *IEEE Trans. Image Process.* **14** 125–40
- [198] Eppstein M J, Dougherty D E, Troy T L and Sevick-Muraca E M 1999 Biomedical optical tomography using dynamic parameterization and Bayesian conditioning on photon migration measurements *Appl. Opt.* **38** 2138–50
- [199] Eppstein M J, Dougherty D E, Hawrysz D J and Sevick-Muraca E M 2001 Three-dimensional Bayesian optical image reconstruction with domain decomposition *IEEE Trans. Med. Imaging* **20** 147–63

- [200] Eppstein M J, Hawrysz D J, Godavarty A and Sevick-Muraca E M 2002 Three-dimensional, Bayesian image reconstruction from sparse and noisy data sets: near-infrared fluorescence tomography *Proc. Natl Acad. Sci. USA* **99** 9619–24
- [201] Ye J C, Webb K J, Bouman C A and Millane R P 1999 Optical diffusion tomography using iterative coordinate descent optimization in a Bayesian framework *J. Opt. Soc. Am. A* **16** 2400–12
- [202] Ye J C, Bouman C A, Webb K J and Millane R P 2001 Nonlinear multigrid algorithms for Bayesian optical diffusion tomography *IEEE Trans. Image Process.* **10** 909–22
- [203] Milstein A B, Oh S, Reynolds J S, Webb K J, Bouman C A and Millane R P 2002 Three-dimensional Bayesian optical diffusion imaging using experimental data *Opt. Lett.* **27** 95–7
- [204] Milstein A B, Oh S, Webb K J, Bouman C A, Zhang Q, Boas D A and Millane R P 2003 Fluorescence optical diffusion tomography *Appl. Opt.* **42** 3081–94
- [205] Milstein A B, Stott J J, Oh S, Boas D A, Millane R P, Bourman C A and Webb K J 2004 Fluorescence optical diffusion tomography using multiple frequency data *J. Opt. Soc. Am. A* **21** 1035–49
- [206] Markel V A and Schotland J C 2001 Inverse problem in optical diffusion tomography: I. Fourier-Laplace inversion formulas *J. Opt. Soc. Am. A* **18** 1336–47
- [207] Markel V A and Schotland J C 2002 Inverse problem in optical diffusion tomography: II. Role of boundary conditions *J. Opt. Soc. Am. A* **19** 558–66
- [208] Markel V A, Mital V and Schotland J C 2003 Inverse problem in optical diffusion tomography: III. Inversion formulas and singular-value decomposition *J. Opt. Soc. Am. A* **20** 890–902
- [209] Markel V A, O’Sullivan J A and Schotland J C 2003 Inverse problem in optical diffusion tomography: IV. Nonlinear inversion formulas *J. Opt. Soc. Am. A* **20** 903–12
- [210] Pei Y, Gruber H L and Barbour R L 2001 Influence of systematic error in reference states on image quality and on stability of derived information for DC optical imaging *Appl. Opt.* **40** 5755–69
- [211] Ntziachristos V, Chance B and Yodh A G 1999 Differential diffuse optical tomography *Opt. Express* **5** 230–42
- [212] Kilmer M E, Miller E L, Barbaro A and Boas D 2003 Three-dimensional shape-based imaging of absorption perturbation for diffuse optical tomography *Appl. Opt.* **42** 3129–44
- [213] Li A *et al* 2003 Tomographic optical breast imaging guided by three-dimensional mammography *Appl. Opt.* **42** 5181–90
- [214] Cuccia D J, Bevilacqua F, Durkin A J and Tromberg B J 2005 Modulated imaging: quantitative analysis and tomography of turbid media in the spatial-frequency domain *Opt. Lett.* **30** 1354–6
- [215] Joshi A, Bangerth W, Hwang K, Rasmussen J C and Sevick-Muraca E M 2006 Fully adaptive fem based fluorescence optical tomography from time-dependent measurements with area illumination and detection *Med. Phys.* **33** 1299
- [216] Bassi A, D’Andrea C, Valentini G, Cubeddu R and Arridge S 2008 Temporal propagation of spatial information in turbid media *Opt. Lett.* **33** 2836–8
- [217] Knuttel A, Schmitt J M and Knutson J R 1993 Spatial localization of absorbing bodies by interfering diffusive photon density waves *Appl. Opt.* **32** 381–9
- [218] Chance B, Kang K, He L, Weng J and Sevick E M 1993 Highly sensitive object location in tissue models with linear in-phase and anti-phase multi-element optical arrays in one and two dimensions *Proc. Natl Acad. Sci. USA* **90** 3423–7
- [219] Gibson A and Dehghani H 2009 Diffuse optical imaging *Phil. Trans. R. Soc. A* **367** 3055–72
- [220] Gibson A B, Hebden J C and Arridge S R 2005 Recent advances in diffuse optical imaging *Phys. Med. Biol.* **50** R1–43
- [221] Dunsby C and French P M W 2003 Techniques for depth-resolved imaging through turbid media including coherence gated imaging *J. Phys. D: Appl. Phys.* **36** R207–R227
- [222] Schulz R B, Ripoll J and Ntziachristos V 2003 Noncontact optical tomography of turbid media *Opt. Lett.* **28** 1701–3
- [223] Ripoll J and Ntziachristos V 2003 Iterative boundary method for diffuse optical tomography *J. Opt. Soc. Am. A* **20** 1103–10
- [224] Ripoll J, Schulz R B and Ntziachristos V 2003 Free-space propagation of diffuse light: theory and experiments *Phys. Rev. Lett.* **91** 1039011–1039014
- [225] Klose A D and Hielscher A H 2008 Optical tomography with the equation of radiative transfer *Methods Heat Fluid Flow* **18** 443–64
- [226] Hielscher A H, Klose A D, Scheel A K, Moa-Anderson B, Backhaus M, Netz U and Beuthan J 2004 Sagittal laser optical tomography for imaging of rheumatoid finger joints *Phys. Med. Biol.* **49** 1147–63
- [227] Wright S, Schweiger M and Arridge S R 2007 Reconstruction in optical tomography using the p_n approximations *Meas. Sci. Technol.* **18** 79–86
- [228] Aydin E D, de Oliveira C R E and Goddard A J H 2002 A comparison between transport and diffusion calculations using a finite element-spherical harmonics radiation transport method *Med. Phys.* **29** 2013–23
- [229] Boas D A 1996 Diffuse photon probes of structural and dynamical properties of turbid media: theory and biomedical applications *PhD Dissertation* University of Pennsylvania
- [230] Hull E L and Foster T H 2001 Steady-state reflectance spectroscopy in the P_3 approximation *J. Opt. Soc. Am. A* **18** 584–99
- [231] Firbank M, Arridge S R, Schweiger M and Delpy D T 1996 An investigation of light transport through scattering bodies with non-scattering regions *Phys. Med. Biol.* **41** 767–83
- [232] Arridge S R, Dehghani H, Schweiger M and Okada E 2000 The finite element model for the propagation of light in scattering media: a direct method for domains with non-scattering regions *Med. Phys.* **27** 252–64
- [233] Riley J, Dehghani H, Schweiger M, Arridge S R, Ripoll J and Nieto-Vesperinas M 2000 3d optical tomography in the presence of void regions *Opt. Express* **7** 462–7
- [234] Hayashi T, Kashio Y and Okada E 2003 Hybrid monte carlo-diffusion method for light propagation in tissue with a low-scattering region *Appl. Opt.* **42** 2888–96
- [235] Dehghani H, Srinivasan S, Pogue B W and Gibson A 2009 Numerical modelling and image reconstruction in diffuse optical tomography *Phil. Trans. R. Soc. A* **367** 3073–93
- [236] Srinivasan S, Pogue B W, Carpenter C, Yalavarthy P K and Paulsen K 2007 A boundary element approach for image-guided near-infrared absorption and scatter estimation *Med. Phys.* **34** 4545–57
- [237] Wang L V and Jacques S L 1993 Hybrid model of Monte Carlo simulation diffusion theory for light reflectance by turbid media *J. Opt. Soc. Am. A* **10** 1746–52
- [238] Kak A C and Slaney M 1988 *Principles of Computerized Tomographic Imaging* (New York: IEEE Press)
- [239] O’Leary M A 1996 Imaging with diffuse photon density waves *PhD Dissertation* University of Pennsylvania

- [240] Lagendijk A and Biemond J 1991 *Iterative Identification and Restoration of Images* (Dordrecht: Kluwer)
- [241] Per Christian Hansen 1998 *Rank-Deficient and Discrete Ill-Posed Problems* (Philadelphia: SIAM)
- [242] Tikhonov A N 1963 Regularization of mathematically incorrectly posed problems *Sov. Math.* **4** 1624
- [243] Douiri A, Schweiger M, Riley J and Arridge S 2005 Local diffusion regularization method for optical tomography reconstruction by using robust statistics *Opt. Lett.* **30** 2439–41
- [244] Hansen P and O’Leary D 1993 The use of the L-curve in the regularization of discrete ill-posed problems *SIAM J. Sci. Comput.* **14** 1487–503
- [245] Hansen P 1992 Analysis of discrete ill-power problems by means of the L-curve *SIAM Rev.* **34** 561–80
- [246] Boas D A 1997 A fundamental limitation of linearized algorithms for diffuse optical tomography *Opt. Express* **1** 404–13
- [247] Li X D, Pattanayak D N, Durduran T, Culver J P, Chance B and Yodh A G 2000 Near-field diffraction tomography with diffuse photon density waves *Phys. Rev. E* **61** 4295–309
- [248] Schotland J C and Markel V A 2001 Inverse scattering with diffusing waves *J. Opt. Soc. Am. A* **18** 2767–77
- [249] Matson C L 1997 A diffraction tomographic model of the forward problem using diffuse photon density waves *Opt. Express* **1** 6–11
- [250] Konecky S D, Panasyuk G Y, Lee K, Markel V A, Yodh A G and Schotland J C 2008 Imaging complex structures with diffuse light *Opt. Express* **16** 5048–60
- [251] Moskow S and Schotland J C 2008 Convergence and stability of the inverse scattering series for diffuse waves *Inverse Problems* **24** 065005
- [252] O’Leary M A, Boas D A, Chance B and Yodh A G 1994 Reradiation and imaging of diffuse photon density waves using fluorescent inhomogeneities *J. Lumin.* **60** 1 281–6
- [253] O’Leary M A, Boas D A, Li X D, Chancey B and Yodh A G 1996 Fluorescence lifetime imaging in turbid media *Opt. Lett.* **21** 158–60
- [254] Li X D, O’Leary M A, Boas D A, Chance B and Yodh A G 1996 Fluorescent diffuse photon density waves in homogeneous and heterogeneous turbid media: analytic solutions and applications *Appl. Opt.* **35** 3746–58
- [255] Li X D, Chance B and Yodh A G 1998 Fluorescent heterogeneities in turbid media: limits for detection, characterization and comparison with absorption *Appl. Opt.* **37** 6833–44
- [256] Patterson M S and Pogue B W 1994 Mathematical-model for time-resolved and frequency-domain fluorescence spectroscopy in biological tissue *Appl. Opt.* **33** 1963–74
- [257] Sevick-Muraca E M and Burch C L 1994 The origin of phosphorescence signals re-emitted from tissues *Opt. Lett.* **19** 1928–30
- [258] Reynolds J S, Troy T L, Mayer R H, Thompson A B, Waters D J, Cornell K K, Snyder P W and Sevick-Muraca E M 1999 Imaging of spontaneous canine mammary tumors using fluorescent contrast agents *Photochem. Photobiol.* **70** 87–94
- [259] Sevick-Muraca E M, Lopez G, Reynolds J S, Troy T L and Hutchinson C L 1997 fluorescence and absorption contrast mechanisms for biomedical optical imaging using frequency-domain techniques *Photochem. Photobiol.* **66** 55–64
- [260] Wu J, Feld M S and Rava R P 1993 Analytical model for extracting intrinsic fluorescence in turbid media *Appl. Opt.* **32** 3585–95
- [261] Wu J, Wang Y, Perelman L, Itzkan I, Dasari R R and Feld M S 1997 Time-resolved multichannel imaging of fluorescent objects embedded in turbid media **20** 489–91 1995
- [262] Durkin A J, Jaikumar S, Ramanujam N and Richards-Kortum R 1994 Relation between fluorescence spectra of dilute and turbid samples *Appl. Opt.* **33** 414–4
- [263] Chang J W, Gruber H L and Barbour R L 1997 Luminescence optical tomography of dense scattering media *J. Opt. Soc. Am. A* **14** 288–99
- [264] Paithankar D Y, Chen A U, Pogue B W, Patterson M S and Sevick-Muraca E M 1997 Imaging of fluorescent yield and lifetime from multiply scattered light reemitted from random media *Appl. Opt.* **36** 2260–72
- [265] Jiang H 1998 Frequency-domain fluorescent diffusion tomography: a finite-element-based algorithm and simulations *Appl. Opt.* **37** 5337–43
- [266] Ntziachristos V and Weissleder R 2001 Experimental three-dimensional fluorescence reconstruction of diffuse media by use of a normalized born approximation *Opt. Lett.* **26** 893–5
- [267] Wilson B C, Patterson M S and Lilge L 1997 Implicit and explicit dosimetry in photodynamic therapy: a new paradigm *Las. Med. Sci.* **12** 182–92
- [268] Cottrell W J, Oseroff A R and Foster T H 2006 A portable instrument that integrates irradiation with fluorescence and reflectance spectroscopies during clinical photodynamic therapy of cutaneous disease *Rev. Sci. Instrum.* **77** 064302
- [269] Ntziachristos V, Bremer C, Graves E E, Ripoll J and Weissleder R 2002 *In vivo* tomographic imaging of near-infrared fluorescent probes *Mol. Imaging* **1** 82–8
- [270] Weissleder R and Ntziachristos V 2003 Shredding light onto live molecular targets *Nature Med.* **9** 123–8
- [271] Ntziachristos V, Ripoll J, Wang L V and Weissleder R 2005 Looking and listening to light: the evolution of whole-body photonic imaging *Nature Biotechnol.* **23** 313–20
- [272] Tanaka E, Choi H S, Fujii H, Bawendi M G and Frangioni J V 2006 Image-guided oncologic surgery using invisible light: completed pre-clinical development for sentinel lymph node mapping *Ann. Surg. Oncol.* **13** 1671–81
- [273] Sevick-Muraca E M *et al* 2008 Imaging of lymph flow in breast cancer patients after microdose administration of a near-infrared fluorophore: feasibility study *Radiology* **246** 734–4
- [274] Hagen A J, Grosenick D, Pöllinger A, Burock S, Warnick P, Macdonald R, Rinneberg H H and Schlag P M 2009 *In-vivo* fluorescence imaging of breast cancer *SPIE Photonics West (San Jose, CA)* pp 7174–38
- [275] Leproux A, van der Voort M, Harberts R, Verhaegh W, Bakker L, Nielsen T, Brendel B J and van der Mark M B 2009 Optical mammography: improved sensitivity by combined absorption and fluorescence analysis *SPIE Photonics West (San Jose, CA)* pp 7174–37
- [276] Kuebler W M 2008 How NIR is the future in blood flow monitoring? *J. Appl. Physiol.* **104** 905–6
- [277] Terborg C, Bramer S, Harscher S, Simon M and Witte O W 2004 Bedside assessment of cerebral perfusion reductions in patients with acute ischaemic stroke by near-infrared spectroscopy and indocyanine green *J. Neurol. Neurosurg. Psychiatry* **75** 38–42
- [278] Liebert A, Wabnitz H, Steinbrink J, Moller M, Macdonald R, Rinneberg H, Villringer A and Obrig H 2005 Bed-side assessment of cerebral perfusion in stroke patients based on optical monitoring of a dye bolus by time-resolved diffuse reflectance *NeuroImage* **24** 426–35
- [279] Keller E, Wietasch G, Ringleb P, Scholz M, Schwarz S, Stingle R, Schwab S, Hanley D and Hacke W 2000 Bedside monitoring of cerebral blood flow in patients with acute hemispheric stroke *Crit. Care Med.* **28** 511–16

- [280] Apreleva S V, Wilson D F and Vinogradov S A 2006 Tomographic imaging of oxygen by phosphorescence lifetime *Appl. Opt.* **45** 8547–59
- [281] Vinogradov S A, Lo L W, Jenkins W T, Evans S M, Koch C and Wilson D F 1996 Noninvasive imaging of the distribution of oxygen in tissue *in vivo* using infrared phosphors *Biophys. J.* **70** 1609
- [282] Sakadžić S, Yuan S, Dilekz̄ E, Ruvinskaya S, Vinogradov S A, Ayata C and Boas D A 2009 Simultaneous imaging of cerebral partial pressure of oxygen and blood flow during functional activation and cortical spreading depression *Appl. Opt.* **48** 169–77
- [283] Wang G, Cong W, Durairaj K, Qian X, Shen H, Sinn P, Hoffman E, McLennan G and Henry M 2002 *In vivo* mouse studies with bioluminescence tomography *Biomed. Eng.* **4** 235–60
- [284] Quistorff B, Haselgrave J C and Chance B 1985 High spatial resolution readout of 3-D metabolic organ structure: An automated, low-temperature redox ratio-scanning instrument *Anal. Biochem.* **148** 389–400
- [285] Ramanujam N 2000 Fluorescence spectroscopy *in vivo* *Encyclopedia of Analytical Chemistry* (New York: Wiley) pp 20–56
- [286] Bigio I J and Mourant J R 2003 Optical biopsy *Encyclopedia of Optical Engineering* (New York: Dekker)
- [287] Bigio I J and Bown S G 2004 Spectroscopic sensing of cancer and cancer chemotherapy, current status of translational research *Cancer Biol. Ther.* **3** 259–67
- [288] Ji S, Chance B, Stuart B H and Nathan R 1977 Two-dimensional analysis of the redox state of the rat cerebral cortex *in vivo* by NADH fluorescence photography *Brain Res.* **119** 357–73
- [289] Siesjo B K 1978 *Brain Energy Metabolism* (New York: Wiley) p 4
- [290] Buxton R B and Frank L R 1997 A model for the coupling between cerebral blood flow and oxygen metabolism during neural stimulation *J. Cereb. Blood Flow Metab.* **17** 64–72
- [291] Friston K J, Mechelli A, Turner R and Price C J 2000 Nonlinear responses in fMRI: the balloon model, volterra kernels, and other hemodynamics *NeuroImage* **12** 466–77
- [292] Gjedde A 1997 *Cerebrovascular disease* chapter on The relation between brain function and cerebral blood flow and metabolism, (Philadelphia: Lippincott-Raven) pp 23–40
- [293] Kety S S and Schmidt C F 1948 The nitrous oxide method for the quantitative determination of cerebral blood flow in man; theory, procedure and normal values *J. Clin. Invest.* **27** 476–83
- [294] Gesztesy G, Finnegan W, DeMaro J A, Wang J Y and Chen J L 1993 Parenchymal microvascular systems and cerebral atrophy in spontaneously hypertensive rats *Brain Res.* **611** 249–57
- [295] Boas D A, Strangman G, Culver J P, Hoge R D, Jaszczewski G, Poldrack R A, Rosen B R and Mandeville J B 2003 Can the cerebral metabolic rate of oxygen be estimated with near-infrared spectroscopy? *Phys. Med. Biol.* **48** 2405–18
- [296] American cancer society, statistics for 2007: Cancer facts & figures 2007 http://www.cancer.org/docroot/STT/stt_0.asp accessed July 8, 2007.
- [297] Kerlikowske K, Barclay J, Grady D, Sickles E A and Ernster V 1997 Comparison of risk factors for ductal carcinoma *in situ* and invasive breast cancer *J. Natl Cancer Inst.* **89** 76–82
- [298] Goergen S K, Evans J, Cohen G P B and MacMillan J H 1997 Characteristics of breast carcinomas missed by screening radiologists *Radiology* **204** 131–5
- [299] Birdwell R L, Ikeda D M, O'Shaughnessy K F and Sickles E A 2001 Mammographic characteristics of 115 missed cancers later detected with screening mammography and the potential utility of computer-aided detection *Radiology* **219** 192–202
- [300] Wang J, Shih T T, Hsu J C and Li Y W 2000 The evaluation of false negative mammography from malignant and benign breast lesions *J. Clin. Imaging* **24** 96–103
- [301] Fletcher S W 1997 Breast cancer screening among women in their forties: an overview of the issues *J. Natl Cancer Inst. Monogr.* **22** 5–9
- [302] Elmore J G, Barton M B, Moceri V M, Polk S, Arena P J and Fletcher S W 1998 Ten-year risk of false positive screening mammograms and clinical breast examinations *New Engl. J. Med.* **338** 1089–96
- [303] Bevilacqua F, Berger A J, Cerussi A E, Jakubowski D and Tromberg B J 2000 Broadband absorption spectroscopy in turbid media by combined frequency-domain and steady-state methods *Appl. Opt.* **39** 6498–507
- [304] Cheng X, Mao J, Bush R, Kopans D B, Moore R H and Chorlton M 2003 Breast cancer detection by mapping hemoglobin concentration and oxygen saturation *Appl. Opt.* **42** 6412–21
- [305] Chance B, Nioka S, Zhang J, Conant E F, Hwang E, Briest S, Orel S G, Schnall M D and Czerniecki B J 2005 Breast cancer detection based on incremental biochemical and physiological properties of breast cancers: a six-year, two-site study *Acad. Radiol.* **12** 925–33
- [306] Simick M K, Jong R, Wilson B and Lilge L 2004 Non-ionizing near-infrared radiation transillumination spectroscopy for breast tissue density and assessment of breast cancer risk *J. Biomed. Opt.* **9** 794–803
- [307] Xu R X, Quangy B, Mao J J and Povoski S P 2007 Development of a handheld near-infrared imager for dynamic characterization of *in vivo* biological tissue systems *Appl. Opt.* **46** 7442–51
- [308] Chen N G, Guo P Y, Yan S K, Piao D Q and Zhu Q 2001 Simultaneous near-infrared diffusive light and ultrasound imaging *Appl. Opt.* **40** 6367–80
- [309] Franceschini M A, Moesta K T, Fantini S, Gaida G, Gratton E, H Jess, Mantulin W W, Seeber M, Schlag P M and Kaschke M 1997 Frequency-domain techniques enhance optical mammography: initial clinical results *Proc. Natl Acad. Sci. USA* **94** 6468–73
- [310] Pera V E, Heffer E L, Siebold H, Schutz O, Heywang-Kobrunner S, Gotz L, Heinig A and Fantini S 2003 Spatial second-derivative image processing: an application to optical mammography to enhance the detection of breast tumors *J. Biomed. Opt.* **8** 517–24
- [311] Torricelli A, Spinelli L, Pifferi A, Taroni P, Cubeddu R and Danesini G M 2003 Use of a nonlinear perturbation approach for *in vivo* breast lesion characterization by multi-wavelength time-resolved optical mammography *Opt. Express* **11** 853–67
- [312] Bassi A, Spinelli L, D'Andrea C, Guistì A, Swartling J, Pifferi A, Torricelli A and Cubeddu R 2006 Feasibility of white-light time-resolved optical mammography *J. Biomed. Opt.* **11** 054035
- [313] Grosenick D, Moesta K T, Möller M, Mucke J, Wabnitz H, Gebauer B, Stroszczynski C, Wassermann B, Schlag P M and Rinneberg H 2005 Time-domain scanning optical mammography: I. Recording and assessment of mammograms of 154 patients *Phys. Med. Biol.* **50** 2429–50
- [314] Dierkes T, Grosenick D, Moesta K T, Möller M, Schlag P M, Rinneberg H and Arridge S 2005 Reconstruction of optical properties of phantom and breast lesion *in vivo* from paraxial scanning data *Phys. Med. Biol.* **50** 2519–42

- [315] Colak S B, van der Mark M B, Hooft G W, Hoogenraad J H, van der Linden E S and Kuijpers F A 1999 Clinical optical tomography and NIR spectroscopy for breast cancer detection *IEEE J. Quantum Electron.* **5** 1143–58
- [316] Iftimia N, Gu X J, Xu Y and Jiang H B 2003 A compact, parallel-detection diffuse optical mammography system *Rev. Sci. Instrum.* **74** 2836–42
- [317] Li C, Zhao H, Anderson B and Jiang H 2006 Multispectral breast imaging using a ten-wavelength, 64x64 source/detector channels silicon photodiode-based diffuse optical tomography system *Med. Phys.* **33** 627–36
- [318] Schmitz C H, Klemer D P, Hardin R, Katz M S, Pei Y, Gruber H L, Levin M B, Levina R D, Fraco N A, Solomon W B and Barbour R L 2005 Design and implementation of dynamic near-infrared optical tomographic imaging instrumentation for simultaneous dual-breast measurements *Appl. Opt.* **44** 2140–53
- [319] McBride T O, Pogue B W, Jiang S, Osterberg U L and Paulsen K D 2001 A parallel-detection frequency-domain near-infrared tomography system for hemoglobin imaging of the breast *in vivo* *Rev. Sci. Instrum.* **72** 1817–24
- [320] Intes X *et al* 2005 Time-domain optical mammography SoftScan: initial results *Acad. Radiol.* **12** 934–47
- [321] Durduran T, Choe R, Culver J P, Zubkov L, Holboke M J, Giannarco J, Chance B and Yodh A G 2002 Bulk optical properties of healthy female breast tissue *Phys. Med. Biol.* **47** 2847–61
- [322] Jiang S D, Pogue B W, Paulsen K D, Kogel C and Poplack S P 2003 *In vivo* near-infrared spectral detection of pressure-induced changes in breast tissue *Opt. Lett.* **28** 1212–4
- [323] Srinivasan S, Pogue B W, Jiang S D, Dehghani H, Kogel C, Soho S, Gibson J J, Tosteson T D, Poplack S P and Paulsen K D 2003 Interpreting hemoglobin and water concentration, oxygen saturation, and scattering measured *in vivo* by near-infrared breast tomography *Proc. Natl Acad. Sci. USA* **100** 12349–54
- [324] Jakubowski D B, Cerussi A E, Bevilacqua F, Shah N, Hsiang D, Butler J and Tromberg B J 2004 Monitoring neoadjuvant chemotherapy in breast cancer using quantitative diffuse optical spectroscopy: a case study *J. Biomed. Opt.* **9** 230–8
- [325] Tromberg B J, Shah N, Lanning R, Cerussi A, Espinoza J, Pham T, Svaasand L and Butler J 2000 Non-invasive *in vivo* characterization of breast tumors using photon migration spectroscopy *Neoplasia* **2** 26–40
- [326] Painchaud Y, Mailloux A, Harvey E, Verreault S, Frechette J, Gilbert C, Vernon M L and Beaudry P 1999 Multi-port time-domain laser mammography: results on solid phantom and volunteers *Int. Symp. on Biomedical Optics (San Jose, CA), Proc. SPIE* **3597** 484–55
- [327] Chance B 1998 Near-infrared images using continuous, phase-modulated and pulsed light with quantitation of blood and blood oxygenation *Ann. New York Acad. Sci.* **838** 19–45
- [328] Suzuki K, Yamashita Y, Ohta K, Kaneko M, Yoshida M and Chance B 1996 Quantitative measurement of optical parameters in normal breasts using time-resolved spectroscopy: *in vivo* results of 30 Japanese women *J. Biomed. Opt.* **1** 330–4
- [329] Thomsen S and Tatman D 1998 Physiological and pathological factors of human breast disease that can influence optical diagnosis *Ann. New York Acad. Sci.* **838** 171–93
- [330] Spinelli L, Torricelli A, Pifferi A, Taroni P, Danesini G M and Cubeddu R 2004 Bulk optical properties and tissue components in the female breast from multiwavelength time-resolved optical mammography *J. Biomed. Opt.* **9** 1137–42
- [331] Boyd N F, Lockwood G A, Byng J W, Tritchler D L and Yaffe M J 1998 Mammographic densities and breast cancer risk *Cancer Epidemiol. Biomarkers Prevent.* **7** 1133–44
- [332] Blyschak K, Simick M, Jong R and Lilge L 2004 Classification of breast tissue density by optical transillumination spectroscopy: optical and physiological effects governing predictive value *Med. Phys.* **31** 1398–414
- [333] Blackmore K M, Knight J A, Jong R and Lilge L 2007 Assessing breast tissue density by transillumination breast spectroscopy (tibs): an intermediate indicator of cancer risk *B. J. Radiology* **80** 545–56
- [334] Blackmore K M, Knight J A and Lilge L 2008 Association between transillumination breast spectroscopy and quantitative mammographic features of the breast *Cancer Epidemiology Biomarkers Prevent.* **17** 1043–50
- [335] Ntziachristos V, Yodh A G, Schnall M and Chance B 2000 Concurrent MRI and diffuse optical tomography of breast after indocyanine green enhancement *Proc. Natl Acad. Sci. USA* **97** 2767–72
- [336] Pogue B W, Poplack S P, McBride T O, Wells W A, Osterman K S, Osterberg U L, and Paulsen K D 2001 Quantitative hemoglobin tomography with diffuse near-infrared spectroscopy: pilot results in the breast *Radiology* **218** 261–6
- [337] Jiang H, Xu Y, Iftimia N, Eggert J, Klove K, Baron L and Fajardo L 2001 Three-dimensional optical tomographic imaging of breast in a human subject. *IEEE Trans. Med. Imaging* **20** 1334–40
- [338] Dehghani H, Pogue B W, Jiang S D, Brooksby B and Paulsen K D 2003 Three-dimensional optical tomography: resolution in small-object imaging *Appl. Opt.* **42** 3117–28
- [339] Zhu Q I, Huang M M, Chen N G, Zarfos K, Jagjivan B, Kane M, Hedge P and Kurtzman S H 2003 Ultrasound-guided optical tomographic imaging of malignant and benign breast lesions: initial clinical results of 19 cases *Neoplasia* **5** 379–88
- [340] Choe R *et al* 2005 Diffuse optical tomography of breast cancer during neoadjuvant chemotherapy: a case study with comparison to MRI *Med. Phys.* **32** 1128–39
- [341] Grosenick D, Wabnitz H, Moesta K T, Mucke J, Schlag P M and Rinneberg H 2005 Time-domain scanning optical mammography: II. Optical properties and tissue parameters of 87 carcinomas *Phys. Med. Biol.* **50** 2451–68
- [342] Spinelli L, Torricelli A, Pifferi A, Taroni P, Danesini G and Cubeddu R 2005 Characterization of female breast lesions from multi-wavelength time-resolved optical mammography *Phys. Med. Biol.* **50** 2489–502
- [343] Enfield L C, Gibson A P, Everdell N L, Delpy D T, Schweiger M, Arridge S R, Richardson C, Keshtgar M, Douek M and Hebden J C 2007 Three-dimensional time-resolved optical mammography of the uncompressed breast *Appl. Opt.* **46** 3628–38
- [344] Dehghani H, Pogue B W, Poplack S P and Paulsen K D 2003 Multiwavelength three-dimensional near-infrared tomography of the breast: initial simulation, phantom and clinical results *Appl. Opt.* **42** 135–45
- [345] Jiang H B, Iftimia N V, Xu Y, Eggert J A, Fajardo L L and Klove K L 2002 Near-infrared optical imaging of the breast with model-based reconstruction *Acad. Radiol.* **9** 186–94
- [346] Zhu Q, Chen N and Kurtzman S H 2003 Imaging tumor angiogenesis by use of combined near-infrared diffusive light and ultrasound *Opt. Lett.* **28** 337–9
- [347] Srinivasan S, Pogue B W, Brooksby B, Jiang S, Dehghani H, Kogel C, Wells W A, Poplack S P and Paulsen K D 2005 Near-infrared characterization of breast tumors *in vivo*

- using spectrally-constrained reconstruction *Tech. Cancer Res. Treat.* **4** 513–26
- [348] Hanahan D and Weinberg R A 2000 The hallmarks of cancer *Cell* **100** 57–70
- [349] Zhu Q, Kurtzma S H, Hegde P, Tannenbaum S, Kane M, Huang M, Chen N G, Jagjivan B and Zarfos K 2005 Utilizing optical tomography with ultrasound localization to image heterogeneous hemoglobin distribution in large breast cancers *Neoplasia* **7** 263–70
- [350] Li C, Grobmyer S R, Massol N, Liang X, Zhang Q, Chen L, Fajardo L L and Jiang H 2008 Noninvasive *in vivo* tomographic optical imaging of cellular morphology in the breast: possible convergence of microscopic pathology and macroscopic radiology *Med. Phys.* **35** 2493–501
- [351] Brown J M 2007 Tumor hypoxia in cancer therapy *Methods Enzymol.* **435** 297–321
- [352] Hockel M and Vaupel P 2001 Tumor hypoxia: definitions and current clinical, biologic and molecular aspects *J. Natl Cancer Inst.* **93** 266–76
- [353] Evans S M and Koch C J 2003 Prognostic significance of tumor oxygenation in humans *Cancer Lett.* **195** 1–16
- [354] Fantini S, Walker S A, Franceschini M A, Kaschke M, Schlag P M and Moesta K T 1998 Assessment of the size, position and optical properties of breast tumors *in vivo* by noninvasive optical methods *Appl. Opt.* **37** 1982–9
- [355] Chernomordik V, Hattery D W, Grosenick D, Wabnitz H, Rinneberg H, Moesta K T, Schlag P M and Gandjbakhche A 2002 Quantification of optical properties of a breast tumor using random walk theory *J. Biomed. Opt.* **7** 80–7
- [356] Heffer E, Pera V, Schutz O, Siebold H and Fantini S 2004 Near-infrared imaging of the human breast: complementing hemoglobin concentration maps with oxygenation images *J. Biomed. Opt.* **9** 1152–60
- [357] Srinivasan S, Pogue B W, Carpenter C, Jiang S, Wells W A, Poplack S P, Kaufman P A and Paulsen K D 2007 Developments in quantitative oxygen-saturation imaging of breast tissue *in vivo* using multispectral near-infrared tomography *Antioxidants Redox Signaling* **9** 1143–56
- [358] McBride T O, Pogue B W, Poplack S, Soho S, Wells W A, Jiang S D, Osterberg U L and Paulsen K D 2002 Multispectral near-infrared tomography: a case study in compensating for water and lipid content in hemoglobin imaging of the breast *J. Biomed. Opt.* **7** 72–9
- [359] Cerussi A, Shah N, Hsiang D, Durkin A, Butler J and Tromberg B J 2006 *In vivo* absorption, scattering and physiologic properties of 58 malignant breast tumors determined by broadband diffuse optical spectroscopy *J. Biomed. Opt.* **11** 044005
- [360] Gu X J, Zhang Q Z, Bartlett M, Schutz L, Fajardo L L and Jiang H B 2004 Differentiation of cysts from solid tumors in the breast with diffuse optical tomography *Acad. Radiol.* **11** 53–60
- [361] Taroni P, Torricelli A, Spinelli L, Pifferi A, Arpaia F, Danesini G and Cubeddu R 2005 Time-resolved optical mammography between 637 and 985 nm: clinical study on the detection and identification of breast lesions *Phys. Med. Biol.* **50** 2469–88
- [362] Yates T, Hebden J C, Gibson A, Everdell N, Arridge S R and Douek M 2005 Optical tomography of the breast using a multi-channel time-resolved imager *Phys. Med. Biol.* **50** 2503–18
- [363] Shah N, Gibbs J, Wolverton D, Cerussi A, Hylton N and Tromberg B J 2005 Combined diffuse optical spectroscopy and contrast-enhanced magnetic resonance imaging for monitoring breast cancer neoadjuvant chemotherapy: a case study *J. Biomed. Opt.* **10** 051503
- [364] Tromberg B J, Cerussi A E, Shah N, Hsiang D, Butler J A, Du T, Compton M and Fedyk A 2005 Predicting response to breast cancer neoadjuvant chemotherapy using diffuse optical spectroscopy *Optical Tomography and Spectroscopy of Tissue VI* vol 5693 ed B Chance *et al* (Bellingham, WA: SPIE)
- [365] Azar F S, Lee K, Khamene A, Choe R, Corlu A, Konecky S D, Sauer F and Yodh A G 2007 Standardized platform for coregistration of non-concurrent diffuse optical and magnetic resonance breast images obtained in different geometries *J. Biomed. Opt.* **12** 051902
- [366] Konecky S D *et al* 2008 Comparison of diffuse optical tomography of human breast with whole-body and breast-only positron emission tomography *Med. Phys.* **35** 446–55
- [367] Breslow N E, Day N E and Davis W 1980 *Statistical Methods in Cancer Research* (Lyon, France: International Agency for Research on Cancer)
- [368] Pepe M S 2003 *The Statistical Evaluation of Medical Tests for Classification and Prediction* (Oxford: Oxford University Press)
- [369] Poplack S P, Tosteson T D, Wells W A, Pogue B W, Meaney P M, Hartov A, Kogel C A, Soho S K, Gibson J J and Paulsen K D 2007 Electromagnetic breast imaging: Results of a pilot study in women with abnormal mammograms *Radiology* **243** 350–9
- [370] Ntziachristos V, Yodh A G, Schnall M D and Chance B 2002 MRI-guided diffuse optical spectroscopy of malignant and benign breast lesions *Neoplasia* **4** 347–54
- [371] Intes X, Ripoll J, Chen Y, Nioka S, Yodh A G and Chance B 2003 *In vivo* continuous-wave optical breast imaging enhanced with indocyanine green *Med. Phys.* **30** 1039–47
- [372] Bastiaens P I and Squire A 1999 Fluorescence lifetime imaging microscopy: spatial resolution of biochemical processes in the cell *Trends Cell Biol.* **9** 48–52
- [373] Kuwana E and Sevick-Muraca E M 2003 Fluorescence lifetime spectroscopy for pH sensing in scattering media *Anal. Chem.* **75** 4325–9
- [374] Godavarty A, Eppstein M J, Zhang C Y, Theru S, Thompson A B, Gurinkel M and Sevick-Muraca E M 2003 Fluorescence-enhanced optical imaging in large tissue volumes using a gain-modulated iccd camera *Phys. Med. Biol.* **48** 1701–20
- [375] Knopp M V, Brix G and Zeger S L 1994 MR mammography with pharmacokinetic mapping for monitoring of breast cancer treatment during neoadjuvant therapy *Magn. Reson. Imaging Clin. N. Am.* **2** 633–58
- [376] Tsuboi N, Ogawa Y, Inomata T, Yoshida D, Yoshida S, Moriki T and Kumon M 1999 Changes in the findings of dynamic MRI by preoperative CAF chemotherapy for patients with breast cancer of stage II and III: pathologic correlation *Oncol. Rep.* **6** 727–32
- [377] Drew P J, Kerin M J, Mahapatra T, Malone C, Monson J R T, Turnbull L W and Fox J N 2001 Evaluation of response to neoadjuvant chemoradiotherapy for locally advanced breast cancer with dynamic contrast-enhanced MRI of the breast *Eur. J. Surg. Oncol.* **27** 617–20
- [378] Wahl R L 1998 Overview of the current status of PET in breast cancer imaging *Q. J. Nucl. Med.* **42** 1–7
- [379] Tiling R, Linke R, Untch M, Richter A, Fieber S, Brinkbaumer K, Tatsch K and Hahn K 2001 F-18-FDG PET and Tc-99m-sestamibi scintimammography for monitoring breast cancer response to neoadjuvant chemotherapy: a comparative study *Eur. J. Nucl. Med.* **28** 711–20
- [380] Jiang S *et al* 2009 Evaluation of breast tumor response to neoadjuvant chemotherapy with tomographic diffuse optical spectroscopy: case studies of tumor region-of-interest changes *Radiology* **252** 551–60
- [381] Zhu Q, Tannenbaum S, Hegde P, Kane M, Xu C and Kurtzman S H 2008 Noninvasive monitoring of breast

- cancer during neoadjuvant chemotherapy using optical tomography with ultrasound localization *Neoplasia* **10** 1028–40
- [382] Cerussi A, Hsiang D, Shah N, Mehta R, Durkin A, Butler J and Tromberg B J 2007 Predicting response to breast cancer neoadjuvant chemotherapy using diffuse optical spectroscopy *Proc. Natl Acad. Sci. US A* **104** 4014–9
- [383] Chung S H, Cerussi A E, Klifa C, Baek H M, Birgul O, Gulsen G, Merritt S I, Hsiang D and Tromberg B J 2008 *In vivo* water state measurements in breast cancer using broadband diffuse optical spectroscopy *Phys. Med. Biol.* **53** 6713–27
- [384] Taroni P, Comelli D, Pifferi A, Torricelli A and Cubeddu R 2007 Absorption of collagen: effects on the estimate of breast composition and related diagnostic implications *J. Biomed. Opt.* **12** 014021
- [385] Liang X, Zhang Q, Li C, Grobmyer S R, Fajardo L L and Jiang H 2008 Phase-contrast diffuse optical tomography: pilot results in the breast *Acad. Radiol.* **15** 859–66
- [386] Brooksby B, Jiang S D, Dehghani H, Pogue B W, Paulsen K D, Kogel C, Doyley M, Weaver J B and Poplack S P 2004 Magnetic resonance-guided near-infrared tomography of the breast *Rev. Sci. Instrum.* **75** 5262–70
- [387] Brooksby B, Jiang S, Dehghani H, Pogue B W, Paulsen K D, Weaver J, Kogel C and Poplack S P 2005 Combining near-infrared tomography and magnetic resonance imaging to study *in vivo* breast tissue: implementation of a Laplacian-type regularization to incorporate magnetic resonance structure *J. Biomed. Opt.* **10** 051504
- [388] Boverman G, Miller E L, Li A, Zhang Q, Chaves T, Brooks D H and Boas D A 2005 Quantitative spectroscopic diffuse optical tomography of the breast guided by imperfect *a priori* structural information *Phys. Med. Biol.* **50** 3941–56
- [389] Carpenter C M, Pogue B W, Jiang S, Dehghani H, Wang X, Paulsen K D, Wells W A, Forero J, Kogel C, Weaver J B, Poplack S P and Kaufman P A 2007 Image-guided optical spectroscopy provides molecular-specific information *in vivo*: MRI-guided spectroscopy of breast cancer hemoglobin, water and scatterer size *Opt. Lett.* **32** 933–5
- [390] Carpenter C M, Srinivasan S, Pogue B W and Paulsen K D 2008 Methodology development for three-dimensional MR-guided near infrared spectroscopy of breast tumors *Opt. Express* **16** 17903–14
- [391] Zhang Q *et al* 2005 Coregistered tomographic x-ray and optical breast imaging: initial results *J. Biomed. Opt.* **10** 024033
- [392] Fang Q, Carp S A, Selb J, Boverman G, Zhang Q, Kopans D B, Moore R H, Miller E L, Brooks D H and Boas D A 2009 Combined optical imaging and mammography of the healthy breast: optical contrast derived from breast structure and compression *IEEE Trans. Med. Imaging* **28** 30–42
- [393] Zhu Q, Durduran T, Ntziachristos V, Holboke M and Yodh A G 1999 Imager that combines near-infrared diffusive light and ultrasound *Opt. Lett.* **24** 1050–2
- [394] Holboke M J, Tromberg B J, Li X, Shah N, Fishkin J, Kidney D, Butler J, Chance B and Yodh A G 2000 Three-dimensional diffuse optical mammography with ultrasound localization in a human subject *J. Biomed. Opt.* **5** 237–47
- [395] Zhu Q, Conant E and Chance B 2000 Optical imaging as an adjunct to sonograph in differentiating benign from malignant breast lesions *J. Biomed. Opt.* **5** 229–36
- [396] Ermilov S A, Khamapirad T, Conjusteau A, Leonard M H, Lacewell R, Megta K, Miller T and Oraevsky A A 2009 Laser optoacoustic imaging system for detection of breast cancer *J. Biomed. Opt.* **14** 024007
- [397] Roy C S and Sherrington C S 1890 On the regulation of the blood-supply of the brain *J. Physiol.* **11** 85
- [398] Mosso A 1881 *Ueber den Kreislauf des Blutes im menschlichen Gehirn* (Leipzig: Veit)
- [399] Lou H C, Edvinsson L and Mackenzie E T 1987 The concept of coupling blood-flow to brain-function—revision required *Ann. Neurol.* **22** 289–97
- [400] Villringer A and Dirnagl U 1995 Coupling of brain activity and cerebral blood flow: basis of functional neuroimaging *Cereb. Brain. Metab. Rev.* **7** 240–76
- [401] Paulson O B, Strandgaard S and Edvinsson L 1990 Cerebral autoregulation *Cerebrovasc. Brain Metab. Rev.* **2** 161–92
- [402] Smith M 2008 Monitoring intracranial pressure in traumatic brain injury *Anesth. Analg.* **106** 240–8
- [403] Wintermark M *et al* 2005 Comparative overview of brain perfusion imaging techniques *Stroke* **36** 83–99
- [404] Rosenblum B R, Bonner R F and Oldfield E H 1987 Intraoperative measurement of cortical blood flow adjacent to cerebral AVM using laser doppler velocimetry *J. Neurosurg.* **66** 396–9
- [405] Fasano V A, Urciuoli R, Bolognese P and Mostert M 1988 Intraoperative use of laser doppler in the study of cerebral microvascular circulation *Acta Neurochirurgica* **95** 40–8
- [406] Prakash N, Uhleman F, Sheth S A, Bookheimer S, Martin N and Toga A W 2008 Current trends in intraoperative optical imaging for functional brain mapping and delineation of lesions of language cortex *NeuroImage* **47** T116–26
- [407] Binzoni T, Leung T S, Boggett D and Delpy D T 2003 Non-invasive laser Doppler perfusion measurements of large tissue volumes and human skeletal muscle blood RMS velocity *Phys. Med. Biol.* **48** 2527–49
- [408] Dunn A K, Bolay T, Moskowitz M A and Boas D A 2001 Dynamic imaging of cerebral blood flow using laser speckle *J. Cereb. Blood Flow Metab.* **21** 195–201
- [409] Durduran T, Burnett M G, Yu G, Zhou C, Furuya D, Yodh A G, Detre J A and Greenberg J H 2004 Spatio-temporal quantification of cerebral blood flow during functional activation in rat somatosensory cortex using laser speckle flowmetry *J. Cereb. Blood Flow Metab.* **24** 518–25
- [410] Kirkham F J, Padayachee T S, Parsons S, Segeant L S, House F R and Gosling R G 1986 Transcranial measurement of blood velocities in the basal cerebral arteries using pulsed doppler ultrasound: velocity as an index of flow *Ultrasound Med. Biol.* **12** 15–21
- [411] Bishop C C, Powell S, Rutt D and Browne N L 1986 Transcranial doppler measurement of middle cerebral artery blood flow velocity: a validation study *Stroke* **17** 913–5
- [412] Pindzola R R, Balzer J R, Nemoto E M, Goldstein S and Yonas H 2001 Cerebrovascular reserve in patients with carotid occlusive disease assessed by stable xenon-enhanced ct cerebral blood flow and transcranial Doppler *Stroke* **32** 1811–7
- [413] Alexandrov A V, Demchuk A M, Wein T H and Grotta J C 1999 Yield of transcranial Doppler in acute cerebral ischemia *Stroke* **30** 1604–9
- [414] Detre J A and Alsop D C 1999 Perfusion magnetic resonance imaging with continuous arterial spin labeling: methods and clinical applications in the central nervous system *Eur. J. Radiol.* **30** 115–24
- [415] Barbier E L, Silva A C, Kim S G and Koretsky A P 2001 Perfusion imaging using dynamic arterial spin labeling (DASL) *Magn. Reson. Med.* **45** 1021–9
- [416] Detre J A, Zhang W, Roberts D A, Silva A C, Williams D S, Grandis D J, Koretsky A P and Leigh J S 1994 Tissue specific perfusion imaging using arterial spin labeling *NMR Biomed.* **7** 75–82

- [417] Kim S G 1995 Quantification of relative cerebral blood flow change by flow-sensitive alternating inversion recovery (FAIR) technique: application to functional mapping *Magn. Reson. Med.* **34** 293–301
- [418] Kwong K K *et al* 1992 Dynamic magnetic resonance imaging of human brain activity during primary sensory stimulation *Proc. Natl Acad. Sci. USA* **89** 5675–9
- [419] Pindzola R R and Yonas H 1998 The xenon-enhanced computed tomography cerebral blood flow method *Neurosurgery* **43** 1488–92
- [420] Yonas R P, and Pindzola H and Johnson D W 1996 Xenon/computed tomography cerebral blood flow and its use in clinical management *Neurosurg. Clin. N. Am.* **7** 605–16
- [421] Frackowiak R S, Lenzi G L, Jones T and Heather J D 1980 Quantitative measurement of regional cerebral blood flow and oxygen metabolism in man using 150 and positron emission tomography: theory, procedure and normal values *J. Comput. Assist. Tomogr.* **4** 727–36
- [422] Reivich M *et al* 1979 The [¹⁸F] fluorodeoxyglucose method for the measurement of local cerebral glucose utilization in man *Circ. Res.* **44** 127–37
- [423] Phelps M E, Mazziotta J C, Schelbert H R, Hawkins R A and Engel J 1985 Clinical PET - what are the issues *J. Nucl. Med.* **26** 1353–8
- [424] Brazzy J E, Lewis D V, Mitnick M H and Jobsis F F 1985 Noninvasive monitoring of cerebral oxygenation in preterm infants: preliminary observations *Pediatrics* **75** 217–25
- [425] Brazzy J E and Lewis D V 1986 Changes in cerebral blood volume and cytochrome AA3 during hypertensive peaks in preterm infants *J. Pediatrics* **108** 983–7
- [426] Bucher H U, Edwards A D, Lipp A E and Duc G 1993 Comparison between near infrared spectroscopy and ¹³³Xenon clearance for estimation of cerebral blood flow in critically ill preterm infants *Pediatric Res.* **33** 56–9
- [427] Cope M 1991 *The Development of a Near-Infrared Spectroscopy System and Its Application for Noninvasive Monitoring of Cerebral Blood and Tissue Oxygenation in the Newborn Infant* (London: University College London)
- [428] Delpy D T, Cope M C, Cady E B, Wyatt J S, Hamilton P A, Hope P L, Wray S and Reynolds E O 1987 Cerebral monitoring in newborn infants by magnetic resonance and near infrared spectroscopy *Scand. J. Clin. Lab. Invest. Suppl.* **188** 9–17
- [429] Hintz S R, Benaron D A, Siegel A M, Stevenson D K and Boas D A 1999 Bedside functional imaging of the premature infant brain during passive motor activation *J. Investigative Med.* **47** 60a–60a
- [430] Hebdon J C 2003 Advances in optical imaging of the newborn infant brain *Psychophysiol* **40** 501–10
- [431] Hillman E M C 2007 Optical brain imaging *in vivo*: techniques and applications from animal to man *J. Biomed. Opt.* **12**
- [432] Wolf M, Ferrari M and Quaresima V 2007 Progress of near-infrared spectroscopy and topography for brain and muscle clinical applications *J. Biomed. Opt.* **12** 062104
- [433] Dehghani H, White B R, Zeff B W, Tizzard A and Culver J P 2009 Depth sensitivity and image reconstruction analysis of dense imaging arrays for mapping brain function with diffuse optical tomography *Appl. Opt.* **48** 137–43
- [434] Gomersall C D, Joynt G M, Gin T, Freebairn R C and Stewart I E 1997 Failure of the INVOS3100 cerebral oximeter to detect complete absence of cerebral blood flow *Crit. Care Med.* **25** 1252–4
- [435] Schwarz G, Litscher G, Kleinert R and Jobstmann R 1996 Cerebral oximetry in dead subjects *J. Neurosurg. Anesthesiol.* **8** 189–93
- [436] Nicklin S E, Hassan I A A, Wickramasinghe Y A and Spencer S A 2003 The light still shines, but not that brightly? the current status of perinatal near infrared spectroscopy *Arch. Disease Childhood Fetal Neonatal Edn* **88** F263
- [437] Al-Rawi P G 2005 Near infrared spectroscopy in brain injury: today's perspective *Acta Neurochirurgica—Suppl.* **95** 453
- [438] Kirkpatrick P J, Smielewski P, Czosnyka M, Menon D K and Pickard J D 1995 Near-infrared spectroscopy use in patients with head injury *J. Neurosurg.* **83** 963–70
- [439] Gopinath S P, Robertson C S, Contant C F, Narayan R K, Grossman R G and Chance B 1995 Early detection of delayed traumatic intracranial hematomas using near-infrared spectroscopy *J. Neurosurg.* **83** 438–44
- [440] Gopinath S P, Robertson C S, Grossman R G and Chance B 1993 Near-infrared spectroscopic localization of intracranial hematomas *J. Neurosurg.* **79** 43–7
- [441] Lewis S B, Myburgh J A, Thornton E L and Reilly P L 1996 Cerebral oxygenation monitoring by near-infrared spectroscopy is not clinically useful in patients with severe closed-head injury: a comparison with jugular venous bulb oximetry *Crit. Care Med.* **24** 1334–8
- [442] Keller E, Nadler A, Imhof H G, Niederer P, Roth P and Yonekawa Y 2002 New methods for monitoring cerebral oxygenation and hemodynamics in patients with subarachnoid hemorrhage *Acta Neurochirurgica Suppl.* **82** 87
- [443] Carandang R and Krieger D W 2007 Near infrared spectroscopy: finding utility in malignant hemispheric stroke *Neurocrit. Care* **6** 161–4
- [444] Bönöczk P, Panczel G and Nagy Z 2002 Vinpocetine increases cerebral blood flow and oxygenation in stroke patients: a near infrared spectroscopy and transcranial doppler study *Eur. J. Ultrasound* **15** 85–91
- [445] Sakatani K, Xie Y, Lichty W, Li S and Zuo H 1998 Language-activated cerebral blood oxygenation and hemodynamic changes of the left prefrontal cortex in poststroke aphasic patients: a near-infrared spectroscopy study *Stroke* **29** 1299–304
- [446] Kato H, Izumiya M, Koizumi H, Takahashi A and Itoyama Y 2002 Near-infrared spectroscopic topography as a tool to monitor motor reorganization after hemiparetic stroke: A comparison with functional MRI *Stroke* **33** 2032–6
- [447] Miyai I, Yagura H, Hatakenaka M, Oda I, Konishi I and Kubota K 2003 Longitudinal optical imaging study for locomotor recovery after stroke *Stroke* **34** 2866–70
- [448] Damiani M S and Schlosser R 2007 Bilateral near infrared spectroscopy in space-occupying middle cerebral artery stroke *Neurocrit. Care* **6** 165–73
- [449] Vernieri F, Rosato N, Pauri F, Tibuzzi F, Passarelli F and Rossini P M 1999 Near infrared spectroscopy and transcranial doppler in monohemispheric stroke *Eur. Neurol.* **41** 159–62
- [450] Hargroves D, Tallis R, Pomeroy V and Bhalla A 2008 The influence of positioning upon cerebral oxygenation after acute stroke: a pilot study *Age Ageing* **37** 581–5
- [451] Hayakawa T, Terashima M, Kayukawa Y, Ohta T and Okada T 1996 Changes in cerebral oxygenation and hemodynamics during obstructive sleep apneas *Chest* **109** 916–21
- [452] McGown A D, Makker H, Elwell C, Al Rawi P G, Valipour A and Spiro S G 2003 Measurement of changes in cytochrome oxidase redox state during obstructive sleep apnea using near-infrared spectroscopy *Sleep* **26** 710–6
- [453] Spielman A J, Zhang G, Yang C M, D'Ambrosio P, Serizawa S, Nagata M, von Gizycki H and Alfano R R 2000 Intracerebral hemodynamics probed by near infrared

- spectroscopy in the transition between wakefulness and sleep *Brain Res.* **866** 313–25
- [454] Michalos A, Safanova L P, Wolf U, Wolf M, Choi J H, Gupta R, Mantulin W W, Hueber D M, Barbieri B and Gratton E 2002 Obstructive sleep apnea: Evaluation of brain oxygenation and hemodynamics by near-infrared spectroscopy *Sleep* **25** 547
- [455] Taillefer M C and Denault A Y 2005 Cerebral near-infrared spectroscopy in adult heart surgery: systematic review of its clinical efficacy *Can. J. Anesthesia* **52** 79–87
- [456] Al-Rawi P G and Kirkpatrick P J 2006 Tissue oxygen index: Thresholds for cerebral ischemia using near-infrared spectroscopy *Stroke* **37** 2720
- [457] Benaron D A *et al* 2000 Noninvasive functional imaging of human brain using light *J. Cereb. Blood Flow Metab.* **20** 469–77
- [458] Wolfberg A J and du Plessis A J 2006 Near-infrared spectroscopy in the fetus and neonate *Clin. Perinatol.* **33** 707–28
- [459] Minagawa-Kawai Y, Mori K, Hebden J and Dupoux E 2008 Optical imaging of infants' neurocognitive development: recent advances and perspectives *Dev. Neurobiol.* **68** 712–28
- [460] Yang Y, Liu H L, Li X D and Chance B 1997 Low cost frequency-domain photon migration instrument for tissue spectroscopy, oximetry and imaging *Opt. Eng.* **36** 950 1562–69
- [461] Sokoloff L 1960 The effects of carbon dioxide on the cerebral circulation *Anesthesiology* **21** 664–73
- [462] Jasper H 1958 Report of the committee on methods of clinical examination in electroencephalography *Clin. Neurophysiol.* **10** 370–5
- [463] Kastrup A, Kruger G, Neumann-Haefelin T, Glover G H and Moseley M E 2002 Changes of cerebral blood flow, oxygenation and oxidative metabolism during graded motor activation *NeuroImage* pages 74–82
- [464] Ye F Q, Smith A M, Yang Y, Duyn J, Mattay V S, Ruttmann U E, Frank J A, Weinberger D R and McLaughlin A C 1999 Quantitation of regional cerebral blood flow increases during motor activation: a steady-state arterial spin tagging study *Magn. Reson. Med.* **42** 404–7
- [465] Colebatch J G, Deiber M P, Passingham R E, Friston K J and Frackowiak R S 1991 Regional cerebral blood flow during voluntary arm and hand movements in human subjects *J. Neurophysiol.* **65** 1392–401
- [466] Roland P E, Larsen B, Lassen N A and Skinhøj E 1980 Supplementary molaughlinfinger motor area and other cortical areas in organization of voluntary movements in man *J. Neurophysiol.* **43** 118–36
- [467] Seitz R J and Roland P E 1992 Learning of sequential finger movements in man: a combined kinematic and positron emission tomography (pet) study *Eur. J. Neurosci.* **4** 154–65
- [468] Mehagnoul-Schipper D J, van der Kallen B F W, Colier W N J M, van der Sluijs M C, van Erning L J T O, Thijssen H O M, Oeseburg B, Hoefnagels W H L and Jansen R W M M 2002 Simultaneous measurements of cerebral oxygenation changes during brain activation by near-infrared spectroscopy and functional magnetic resonance imaging in healthy young and elderly subjects *Human Brain Mapping* **16** 14–23
- [469] Hoge R D, Atkinson J, Gill B, Crelier G R, Marrett S and Pike G B 1999 Linear coupling between cerebral blood flow and oxygen consumption in activated human cortex *Proc. Natl Acad. Sci. USA* **96** 9403–8
- [470] Hoge R D, Franceschini M A, Covolan R J M, Huppert T, Mandeville J B and Boas D A 2005 Simultaneous recording of task-induced changes in blood oxygenation, volume and flow using diffuse optical imaging and arterial spin-labeling MRI *NeuroImage* **25** 701–7
- [471] Huppert T J, Hoge R D, Diamond S G, Franceschini M A and Boas D A 2006 A temporal comparison of BOLD, ASL and NIRS hemodynamic responses to motor stimuli in adult humans *NeuroImage* **29** 368–82
- [472] Diamond S G, Huppert T J, Kolehmainen V, Franceschini M A, Kaipio J P, Arridge S R and Boas D A 2006 Dynamic physiological modeling for functional diffuse optical tomography *NeuroImage* **30** 88–101
- [473] Joseph D K, Huppert T J, Franceschini M A and Boas D A 2006 Diffuse optical tomography system to image brain activation with improved spatial resolution and validation with functional magnetic resonance imaging *Appl. Opt.* **45** 8142–51
- [474] Huppert T J, Hoge R D, Dale A M, Franceschini M A and Boas D A 2006 Quantitative spatial comparison of diffuse optical imaging with blood oxygen level-dependent and arterial spin labeling-based functional magnetic resonance imaging *J. Biomed. Opt.* **11** 064018
- [475] Huppert T J, Allen M S, Diamond S G and Boas D A 2009 Estimating cerebral oxygen metabolism from fmri with a dynamic multi-compartment windkessel model *Human Brain Mapping* **30** 1548
- [476] Kim M N *et al* 2009 Diffuse optical measurements of cerebral blood flow and oxygenation in patients after traumatic brain injury or subarachnoid hemorrhage *SPIE Photonics West (San Jose, CA)*
- [477] Hebden J C and Austin T 2007 Optical tomography of the neonatal brain *Eur. Radiol.* **17** 2926–33
- [478] Hintz S R, Benaron D A, Houten J P, Duckworth J L, Liu F W H, Spilman S D, Stevenson D K and Cheong W F 1998 Stationary headband for clinical time-of-flight optical imaging at the bedside *Photochem. Photobiol.* **68** 361–9
- [479] Hintz S R, Cheong W F, van Houten J P, Stevenson D K and Benaron D A 1999 Bedside imaging of intracranial hemorrhage in the neonate using light: comparison with ultrasound, computed tomography and magnetic resonance imaging *Pediatric Res.* **45** 54
- [480] Hebden J C, Gibson A, Yusof R M, Everdell N, Hillman E M C, Delpy D T, Arridge S R, Austin T, Meek J H and Wyatt J S 2002 Three-dimensional optical tomography of the premature infant brain *Phys. Med. Biol.* **47** 4155–66
- [481] Hebden J C, Gibson A, Austin T, Yusof R M, Everdell N, Delpy D T, Arridge S R, Meek J H and Wyatt J S 2004 Imaging changes in blood volume and oxygenation in the newborn infant brain using three-dimensional optical tomography *Phys. Med. Biol.* **49** 1117–30
- [482] Kondepudi V R, Heise H M and Backhaus J 2008 Recent applications of near-infrared spectroscopy in cancer diagnosis and therapy *Anal. Bioanal. Chem.* **390** 125–39
- [483] Vardi M and Nini A 2008 Near-infrared spectroscopy for evaluation of peripheral vascular disease. a systematic review of literature *Eur. J. Vasc. Endovasc. Surg.* **35** 68–74
- [484] Luksiene Z 2003 Photodynamic therapy: mechanism of action and ways to improve the efficiency of treatment *Medicina (Kaunas)* **39** 1137–50
- [485] Dougherty T J, Gomer C J, Henderson B W, Jori G, Kessel D, Korbelik M, Moan J and Peng Q 1998 Photodynamic therapy *J. Natl Cancer Inst.* **90** 889–905
- [486] De Grand A M and Frangioni J V 2003 An operational near-infrared fluorescence imaging system prototype for large animal surgery *Tech. Cancer Res. Treat.* **2** 553–62
- [487] Marghoob A A, Swindle L D, Moricz C Z M, Negron F A S, Slue B, Halpern A C H, and Kopf A W 2003 Instruments and new technologies for the *in vivo* diagnosis of melanoma *J. Am. Acad. Dermatol.* **49** 777–97

- [488] Xu Y, Iftimia N, Jiang H B, Key L L and Bolster M B 2001 Imaging of *in vitro* and *in vivo* bones and joints with continuous-wave diffuse optical tomography *Opt. Express* **8** 447–51
- [489] Lasker J M, Fong C J, Ginat D T, Dwyer E and Hielscher A H 2007 Dynamic optical imaging of vascular and metabolic reactivity in rheumatoid joints *J. Biomed. Opt.* **12** 052001
- [490] Wang L V and Wu H I 2007 *Biomedical Optics: Principles and Imaging* 1 edn (New York: Wiley-Interscience) p 5
- [491] Vo-Dinh T (ed) 2003 *Biomedical Photonics Handbook* (Boca Raton, FL: CRC Press)
- [492] Bouma B E and Tearney G J 2001 *Handbook of Optical Coherence Tomography* 1st edn (Colchester, UK: Informa Healthcare) p 11
- [493] Sharpe J 2004 Optical projection tomography *Ann. Rev. Biomed. Eng.* **6** 209–28
- [494] Johansson A, Katharina K, Ronald S and Herbert S 2008 Clinical optical diagnostics—status and perspectives *Med. Laser Appl.* **23** 155–74
- [495] Patterson M S, Andersson-Engels S, Wilson B C and Osei E K 1995 Absorption spectroscopy in tissue-simulating materials: a theoretical and experimental study of photon paths *Appl. Opt.* **34** 22–30
- [496] Zhou C 2007 *In-vivo* optical imaging and spectroscopy of cerebral hemodynamics *PhD Dissertation* University of Pennsylvania